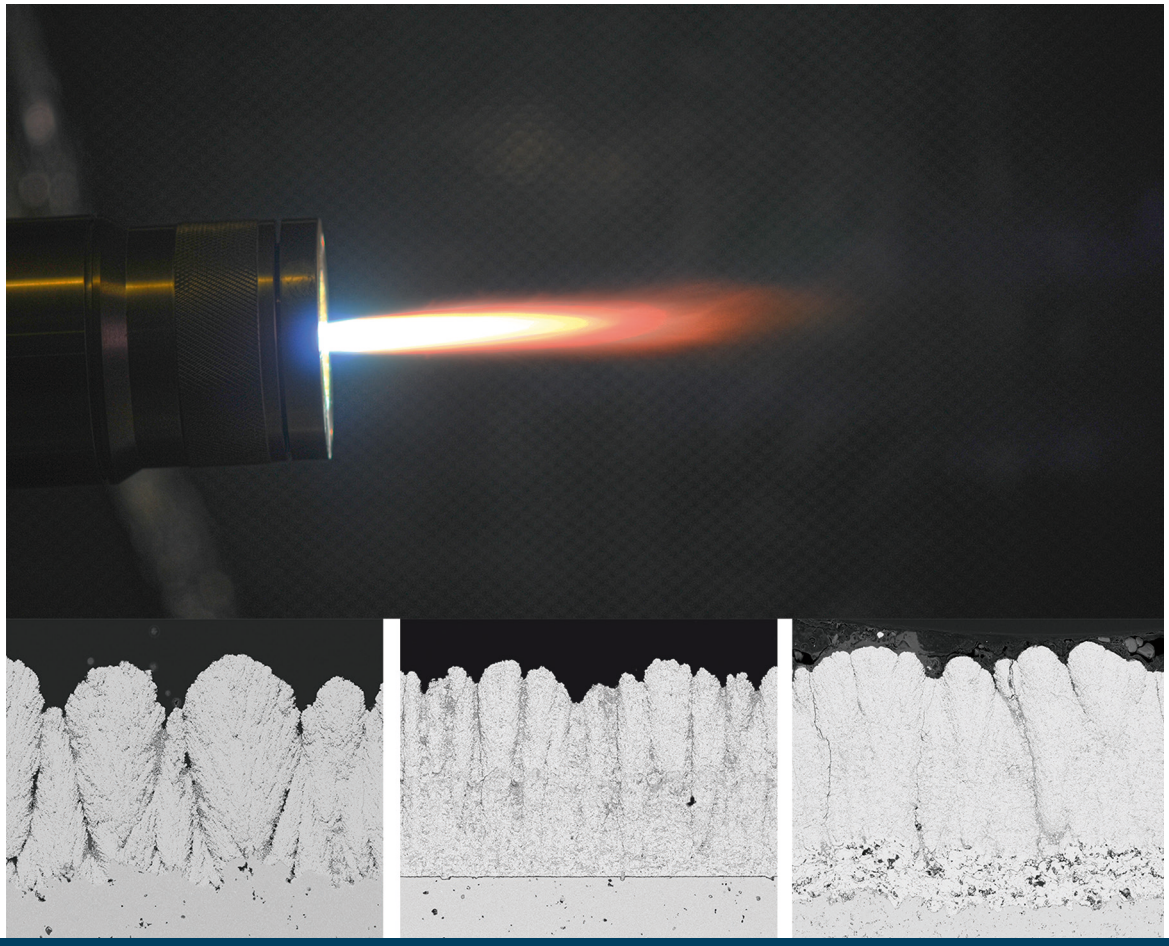

Columnar Structured Thermal Barrier Coatings Deposited by Axial Suspension Plasma Spraying

Dapeng Zhou

Energie & Umwelt / Energy & Environment
Band / Volume 456
ISBN 978-3-95806-391-4

Mitglied der Helmholtz-Gemeinschaft

JÜLICH
Forschungszentrum

Schriften des Forschungszentrums Jülich
Reihe Energie & Umwelt / Energy & Environment Band / Volume 456

Forschungszentrum Jülich GmbH
Institut für Energie- und Klimaforschung
Werkstoffsynthese und Herstellungsverfahren (IEK-1)

Columnar Structured Thermal Barrier Coatings Deposited by Axial Suspension Plasma Spraying

Dapeng Zhou

Schriften des Forschungszentrums Jülich
Reihe Energie & Umwelt / Energy & Environment Band / Volume 456

ISSN 1866-1793 ISBN 978-3-95806-391-4

Bibliografische Information der Deutschen Nationalbibliothek.
Die Deutsche Nationalbibliothek verzeichnet diese Publikation in der
Deutschen Nationalbibliografie; detaillierte Bibliografische Daten
sind im Internet über http://dnb.d-nb.de abrufbar.

Herausgeber und Vertrieb:	Forschungszentrum Jülich GmbH Zentralbibliothek, Verlag 52425 Jülich Tel.: +49 2461 61-5368 Fax: +49 2461 61-6103 zb-publikation@fz-juelich.de www.fz-juelich.de/zb
Umschlaggestaltung:	Grafische Medien, Forschungszentrum Jülich GmbH
Druck:	Grafische Medien, Forschungszentrum Jülich GmbH
Copyright:	Forschungszentrum Jülich 2019

Schriften des Forschungszentrums Jülich
Reihe Energie & Umwelt / Energy & Environment, Band / Volume 456

D 294 (Diss., Bochum, Univ., 2018)

ISSN 1866-1793
ISBN 978-3-95806-391-4

Vollständig frei verfügbar über das Publikationsportal des Forschungszentrums Jülich (JuSER)
unter www.fz-juelich.de/zb/openaccess.

Abstract

Thermal Barrier Coatings (TBCs) providing thermal insulation for underlying metallic components are widely used in turbine engines. Suspension Plasma Spraying (SPS) is a promising technology to produce TBCs. With it, a variety of microstructures can be achieved. Especially columnar structured coatings with high strain tolerance have great potentials as TBCs. Thus the potentials of SPS coatings as TBCs were explored in this work.

In this work, potentials of SPS coatings were discussed with four parts, respectively. In the first part, relationships between spraying parameters, microstructures, mechanical properties and thermal cycling lifetime were preliminarily explored. It was found that spraying parameters especially spraying distance and bond coat roughness greatly affected the microstructures of coatings. A simplified model was built to correlate the mechanical properties to the thermal cycling lifetime.

Even though mechanical properties of coatings were optimized in the first part, the lifetime of SPS coatings was still short compared with APS coatings. Therefore, in the second part, a failure mechanism for columnar SPS coatings was promoted. According to this failure mechanism, two architecture designs were promoted. With the new architectures, the lifetime of SPS coatings was greatly improved.

Sintering behavior of columnar TBCs produced with SPS was discussed in the third part. Annealing resulted in obvious modifications on the microstructure of the coatings. These modifications also led to changes in mechanical properties. It was found that by short time pre-annealing, thermal cycling lifetime of coating could be significantly improved.

In the last part, thermal cycling performances of multilayered GZO/YSZ coatings were discussed. These multilayered coatings exhibited excellent thermal cycling performances which could be attributed to their higher strain tolerance and better sintering resistance.

In summary, SPS is a very promising technology for applying the top coat of TBCs; however, further researches are needed to get a full understanding of this type of coatings.

Kurzfassung

Wärmeschutzbeschichtungen (Thermal Barrier Coatings, TBCs), die eine Wärmeisolierung für darunterliegende metallische Komponenten bereitstellen, werden in Turbinentriebwerken häufig verwendet. Suspensions-Plasma-Spritzen (SPS) ist eine vielversprechende Technologie zur Herstellung von TBCs. Mit ihm können eine Vielzahl von Beschichtungen Mikrostrukturen erreicht werden. Insbesondere säulenförmige strukturierte Beschichtungen mit hoher Dehnungstoleranz haben große Potentiale als TBCs. Daher wurde das Potenzial von SPS-Beschichtungen als TBCs in dieser Arbeit untersucht.

In dieser Arbeit wurden die Potenziale von SPS-Beschichtungen mit jeweils vier Themenbereichen diskutiert. Im ersten Teil wurden die Beziehungen zwischen den Sprühparametern, den Mikrostrukturen, den mechanischen Eigenschaften und der thermischen Zykluslebensdauer vorläufig untersucht. Es wurde festgestellt, dass die Sprühparameter, insbesondere die Sprühdistanz und die Rauheit der Bindungsschicht, die Mikrostruktur der Beschichtungen stark beeinflussten. Ein vereinfachtes Modell wurde erstellt, um die mechanischen Eigenschaften mit der thermischen Zykluslebensdauer zu korrelieren.

Obwohl die mechanischen Eigenschaften von Beschichtungen im ersten Teil optimiert wurden, war die Lebensdauer von SPS-Beschichtungen im Vergleich zu APS-Beschichtungen immer noch kurz. Daher wurde im zweiten Teil ein Versagensmechanismus für SPS-Säulenbeschichtungen befürwortet. Gemäß diesem Fehlermechanismus wurden zwei Architekturentwürfe gefördert. Mit neuen Architekturen wurde die Lebensdauer von SPS-Beschichtungen stark verbessert.

Das Sinterverhalten von säulenförmigen TBCs, die mit SPS hergestellt wurden, wurde im dritten Teil diskutiert. Das Glühen führte zu offensichtlichen Modifikationen der Mikrostruktur der Beschichtungen. Diese Modifikationen führten auch zu Veränderungen der mechanischen Eigenschaften. Zusätzlich wurde gefunden, dass durch kurzzeitiges Vorglühen die Lebensdauer der Beschichtung durch Wärmezyklen signifikant verbessert werden konnte.

Im letzten Teil wurden die thermischen Zyklen von mehrschichtigen Beschichtungen diskutiert. Diese mehrschichtigen Beschichtungen zeigten ausgezeichnete thermische Zyklusleistungen, die auf ihre höhere Verspannungstoleranz und bessere Sinterbeständigkeit zurückgeführt werden konnten.Zusammenfassend ist SPS eine sehr vielversprechende Technologie zum Aufbringen von Deckschichten von TBCs; Es sind jedoch weitere Untersuchungen erforderlich, um diese Art von Beschichtungen vollständig zu verstehen.

Abbreviations

TBCs	Thermal Barrier Coatings
APS	Atmosphere Plasma Spraying
EB-PVD	Electron Beam-Physical Vapor Deposition
SPS	Suspension Plasma Spraying
YSZ	Yttria Stabilized Zirconia
GZO	Gadolinium Zirconate
CMAS	Calcium-Magnesium-Alumino-Silicates
OPR	Overall Pressure Ratio
TIT	Turbine Inlet Temperature
TGO	Thermally Grown Oxide
SEM	Scanning Electron Micrograph
LPPS	Low Pressure Plasma Spraying
HVOF	High Velocity OxyFuel
HVAF	High Velocity Air Fuel
VPS	Vacuum Plasma Spraying
CTE	Coefficient of Thermal Expansion
SPPS	Solution Precursor Plasma Spraying
EDS	Energy-Dispersive X-ray Spectroscopy
IA	Image Analysis
XRD	X-ray Diffraction
ECD	Equivalent Circle Diameter

Contents

1 Introduction and Objective

In the aerospace industry, achieving higher efficiency for gas turbine engines has always been an important research issue. Thermal Barrier Coatings (TBCs) applied to the surface of metallic parts in the hottest part of gas turbine engines are used to improve durability and efficiency [1]. By using TBCs along with internal cooling, a temperature drop of up to 300 K across the TBCs of super-alloy components can be achieved. Hence, the engines can work at a gas temperature higher than the melting point of the metallic components leading to higher energy efficiency and better performances [2]. This benefit continuously promotes the research on TBCs for almost half a century [3].

TBCs are complex multilayered systems composed of an oxidation resistant metallic bond coat and a thermally insulating ceramic top coat. Generally, the two mostly used technologies to apply ceramic top coat are Atmosphere Plasma Spraying (APS) and Electron Beam-Physical Vapor Deposition (EB-PVD) [4, 5]. With APS, a lamellar structured coating can be obtained. Due to the special microstructure with splat boundaries and cracks parallel to the metallic and ceramic coat interface, generally, APS coatings have very low thermal conductivity (0.8 – 1.7 W/mK) [6]. Furthermore, the versatility and low deposition costs make APS coatings very attractive in commercial applications[7]. However, their relatively short cycling lifetime make APS coatings only suitable for low loaded components in aircraft engines, such as combustors, fuel vaporizers and stator vanes [3, 6]. In contrast to APS, columnar structured TBCs with high strain tolerance can be achieved by EB-PVD. Due to the columnar structures, the thermal mismatch can be accommodated and then lead to higher thermal cycling lifetime, even though with a compromise on thermal conductivity (1.5 – 2 W/mK) [8-10]. EB-PVD TBCs are more durable, but their high cost limits their applications in the industry [2].

Suspension Plasma Spraying (SPS), as a relatively novel technique, has the potential of combining the advantages of EB-PVD and APS [11]. By using the SPS technique, TBCs with different microstructures, such as porous, vertical cracked and columnar microstructure, can be obtained with a low cost [12-15]. Especially, columnar TBCs with high strain tolerance have great potential applications in aircraft engines and stationary power plant turbines [3, 4]. Thus in this work, columnar structured SPS TBCs were fabricated and investigated based on processing, performance and properties. The effects of processing parameters on microstructures and properties of TBCs were investigated. Even though many results have been reported on SPS TBCs, the relatively poor and unstable thermal cycling performance of SPS TBCs is still a hot research topic [16-19]. Thus in this work, the effective ways to improve thermal cycling performances of SPS TBCs were also explored.

The most generally used material for the ceramic top coat is 6-8 wt.% Yttria Stabilized Zirconia (YSZ). Even though YSZ has many advantages, such as high fracture toughness, high melting point, low thermal conductivity; there is an upper application temperature limit of about 1473 K for YSZ TBCs

[8, 20, 21]. This is because YSZ undergoes volume changing phase transformation, accompanied with an accelerated sintering, at a temperature above this limit [22]. For these reasons, a number of new materials have been studied to search for better TBC materials than YSZ [20, 23, 24]. Gadolinium Zirconate ($Gd_2Zr_2O_7$, GZO) as a very promising new material has attracted a lot of interest since last decade. It has a high melting point, good phase stability, as well as lower thermal conductivity, better sintering and Calcium-Magnesium-Alumino-Silicates (CMAS) resistance with respect to YSZ [23, 25-28]. However, single layered GZO TBCs are not successful. This is due to its low fracture toughness and the formation of porous interphase $GdAlO_3$ with Thermally Grown Oxide (TGO) [29]. Thus, a YSZ diffusion barrier layer is necessary to prevent this reaction. It has been proved that the double-layered design is very well suitable to APS [30, 31] and EB-PVD [32, 33] TBCs . In this work, a double-layered design was also realized with SPS. The performance of the double-layered APS YSZ/SPS GZO TBCs, such as thermal cycling performances, CMAS and erosion resistance were investigated.

This thesis is organized as follow: In chapter 2, the background on TBCs and spraying techniques are introduced, and also a literature review is given to introduce the state of the art researches on SPS TBCs. In chapter 3, the used characterization methods, spraying facilities and raw materials are briefly introduced. The results are presented and discussed in chapter 4 to 7. In chapter 4, the effects of spraying parameters on microstructure, mechanical properties and thermal cycling lifetime are investigated. In addition, a simplified model was built to correlate the mechanical properties to the thermal cycling lifetime. In chapter 5, in connection with the premature failure of coatings presented in chapter 4, an explanation on failure mechanism is given. Based on this finding, different ways aiming to improve thermal cycling lifetime are promoted and realized. In chapter 6, sintering effects on microstructure, properties and thermal cycling lifetime are discussed. In chapter 7, results on APS YSZ/SPS GZO multi-layered TBCs are presented. Finally, a brief summary of this work is given in chapter 8.

2 Background

2.1 Gas Turbine Engines

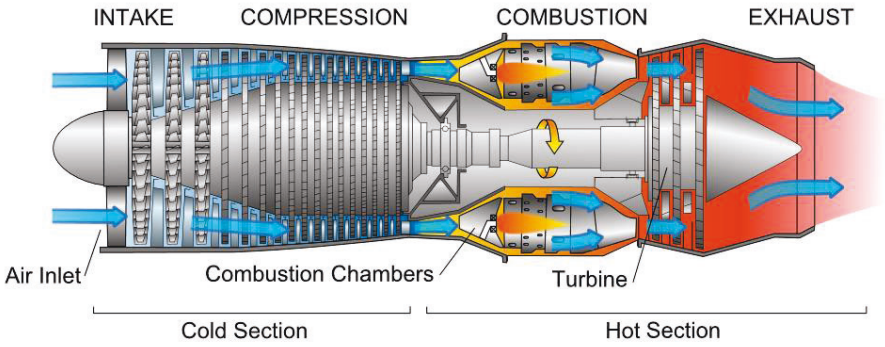

Fig. 2.1 Example of gas turbine (turbojet) configurations [34].

Gas turbine engines which are generally used to propel the aircrafts and generate electricity play important roles in the industry. It has been estimated that gas turbine engines have a $42 billion market all over the world (2010) [35]. Among this huge market, about 65 % is contributed by jet engines used for propelling aircrafts and the rest is contributed by land-based engines for electricity generation. With the growth of electricity demand and airline traffic, the number of gas turbine engines in service will inevitably grow in the next 20 years [36]. A gas turbine mainly consists of three main sections: the compressor, the combustion chamber and the turbine, as shown in Fig. 2.1.

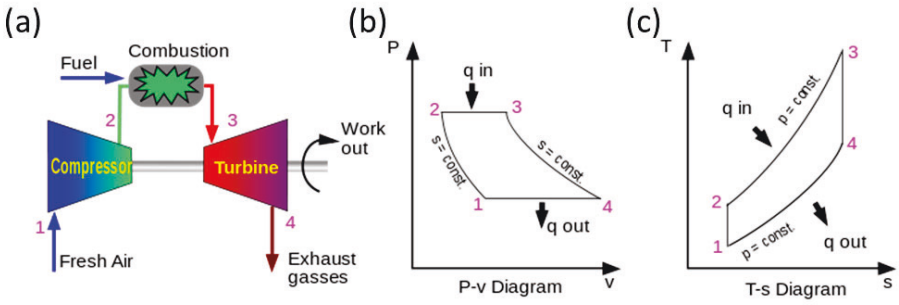

Fig. 2.2 Working mechanism for the ideal Brayton cycle (a); classical Pressure-Volume (P-V) diagram for the Brayton cycle (b); Temperature-Entropy (T-S) diagram [37].

The compressor mechanically increases the pressure of air which is extracted through an intake and drawn into the system. Then the high pressure, high temperature compressed air is delivered to a combustion chamber in where the compressed air is fully mixed with fuel and burned. During the combustion, the temperature of the compressed air is further increased. Finally, in the turbine section, the energy of hot gas is converted into work. Part of the energy that the turbine extracted from hot gas is used to drive the compressor and the remaining energy is used to propel engines or generate electricity. The basic operation of the gas turbine is a Brayton cycle with air as the working fluid.

As described in Fig. 2.2, the Brayton cycle consists of the following four processes: (1) Adiabatic process (from 1 to 2): ambient air is drawn into the compressor and compressed; (2) isobaric heating process (from 2 to 3): the compressed air is directed to the combustion chamber, mixed with fuel, combusted and heated to high temperature at a constant pressure. (3) isentropic process (from 3 to 4): high temperature, compressed air expands through a turbine, cools down and performs work. (4) isobaric cooling process (from 4 to 1): the hot air is cooled by the atmosphere. For ideal Brayton cycle, the efficiency only depends on the Overall Pressure Ratio (OPR) which is the ratio of pressure inside the combustion chamber to the pressure outside; but in reality, as shown in Fig. 2.3, it also depends on the Turbine Inlet Temperature (TIT). As a result of high OPR, the TIT has to be increased as well to realize an optimum Brayton cycle [38]. With continuously increase on TIT for decades, this leads to a great challenge for the serviced materials. Based on the studying historical trend in TIT and the maximum allowable metal operating temperature, the average increase in TIT has been around 19 K/year, which is substantially higher than the increase of operating metal temperature (5 K/year) [38]. As a result of this, metal materials are not able to meet the requirements of high efficient turbine engines on TIT.

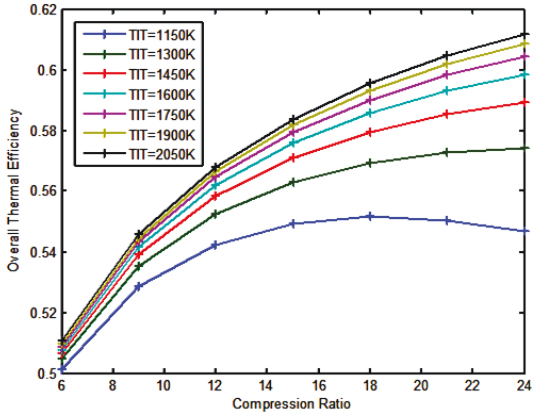

Fig. 2.3 Variation of compression ratio and turbine inlet temperature on overall thermal efficiency [39].

As described in Fig. 2.4, this disparity is compensated by using TBCs in conjunction with innovative air-cooling techniques [40]. By using these two techniques, a reduction of 100 K to 300 K can be achieved on the surface of superalloy components. This enables advanced gas turbine engines to operate at a temperature even above the melting temperature of the superalloy, achieving a remarkable increase in efficiency and performance of engines. Alternatively, by reducing metal temperature, TBCs can make engine components more durable. TBCs have been regarded as one of the most important and effective developments to improve the efficiency of advanced turbines [41].

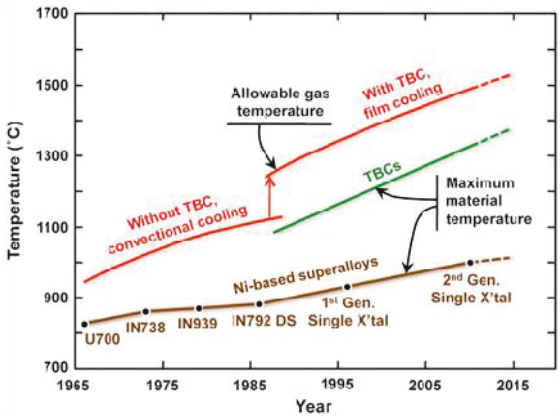

Fig. 2.4 Progression of the operating temperature of Ni-based superalloy and thermal barrier coatings [2].

2.2 Thermal Barrier Coatings (TBCs)

TBCs were first introduced to extend the durability of stationary part of engines such as the combustion chambers [42]. Most of these TBCs were flame sprayed ceramic coatings, such as alumina and zirconia calcia coatings. With the development of plasma torch, plasma sprayed TBCs were successfully used on hot section components of commercial gas turbine engines in the 1970s. In the middle of 1970s, NASA developed a two-layered TBCs with a plasma sprayed NiCrAlY bond coat and a plasma sprayed zirconia yttria ceramic top coat. In the late of 1980s, they were first used on rotating blades [43]. The initial zirconia yttria TBCs are fully stabilized cubic phase. Later, the composition of zirconia yttria was optimized by Stecura [44]. A Yttria Stabilized Zirconia (YSZ) with Yttria level between 6 wt.% to 8 wt.% shows better performances. The first Electron Beam–Physical Vapor Deposited zirconia yttria coatings were deposited by Pratt and Whiney in the late 1970s [45]. The early PVD coatings were reported to have much better burner rig lives than early plasma-sprayed ones. This is because the columnar characteristic of PVD coatings imparts higher stain tolerance to coatings. Until today, Atmospheric Plasma Spray (APS) and Electron Beam-Physical Vapor Deposition (EB-PVD) as two main technical processes for depositing ceramic layers are still

widely used all over the world; YSZ is still the most widely used ceramic layer material. Today, TBCs are critical components in gas turbine engines. And they may be expected to play a more important role in the development of more efficient turbine engines.

TBCs are multi-functional: they must provide thermal insulation to protect the underlying metallic parts; they need to have high strain tolerance to minimize thermal stress which arises from thermal expansion mismatch with superalloy parts under cooling and heating; they must reflect much of the radiant heat to prevent it from reaching the metallic part. Furthermore, TBCs are required to survive from long-term high-temperature service and thermal cycling. Typically, for jet engines, the service time can last for thousands of hours with numerous cycling between maximum temperature 1300 ˚C and low ambient temperature. TBCs also need to withstand extreme thermal gradients (~1˚C/μm) and energy fluxes (~1 MWm^{-2}). These demands and needs to reliably operate TBCs at high temperature for thousands of hours are driving the developments of TBCs [10].

Nowadays, TBCs are a complex multi-layered system consisting of not only ceramic top layer but also the underlying superalloy metallic part. To compromise the thermal mismatch between the ceramic layer and the superalloy, a layer of metallic bond coat is also introduced. This bond coat not only increases bonding; but also protects the underlying superalloy from oxidation. Due to the high-temperature service condition, a thin layer of Thermally Grown Oxide (TGO) is inevitably formed on the bond coat. Thus for an intact TBC system, it consists of at least four layers, as shown in Fig. 2.5 : (a) ceramic top coat, (b) metallic bond coat, (c) Thermally Grown Oxide (TGO), (d) substrate. The characteristics and functions of each layer will be illustrated in the following section.

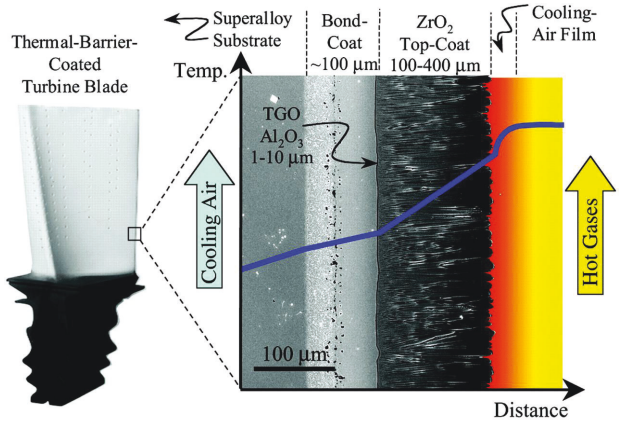

Fig. 2.5 Cross-sectional Scanning Electron Micrograph (SEM) of and EB-PVD TBCs, superimposed onto a schematic diagram showing the temperature reduction provided by the TBC [7].

2.2.1 Ni-Based Superalloys Used for Turbine Engines

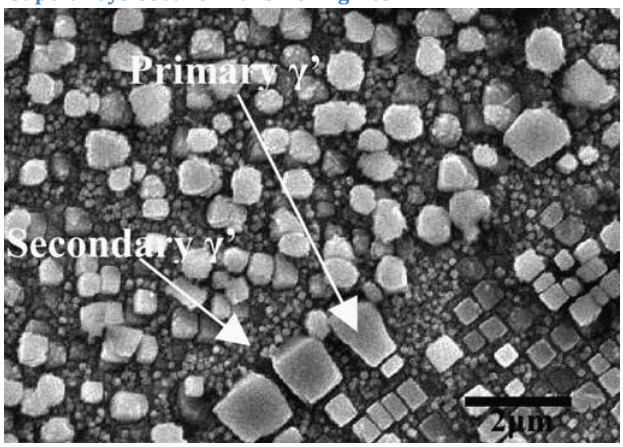

Fig. 2.6 Distribution of γ' phase in solution treated IN 738 superalloy [46].

The term "superalloy" was first used after World War II to describe a group of alloys developed for turbine engines which require high performance at elevated temperature. Nowadays, the applications of superalloys are extended to aircraft and land-based turbine engines, rocket engines, solar thermal power plants and heat exchangers for nuclear reactor systems. Superalloys exhibit several key characteristics, such as excellent mechanical strength, resistance to thermal creep, corrosion and oxidation [47]. With intensive developments on metallurgy and processing since last several decades, as shown in Fig. 2.4, the average maximum service temperature has reached about 1050 ˚C. For some extreme cases, the tolerated temperature can reach to 1200 ˚C, which is about 90% of the melting point [48].

The essential solute in nickel-based superalloys is aluminum. This lead to a two-phase microstructure, consisting of γ and γ' phases, as presented in Fig. 2.6. The γ phase is a matrix in which the γ' (Ni_3Al) phase precipitates. The γ' phase is responsible for the high-temperature strength and its resistance to creep deformation. The amount of the γ' phase depends on chemical composition and temperature. For a given chemical composition, the fraction of the γ' phase increases with a drop of temperature. This phenomenon can be used to adjust the distribution and size of the γ' strengthening precipitates [48, 49]. Heat treated high fraction γ' alloys have a microstructure as shown in Fig. 2.6. Cuboid γ' precipitations separated by channels of the γ matrix. The γ phase has a primitive cubic lattice with a random distribution of different species of atoms. In contrast, the γ' phase has a face-centered cubic lattice with Ni atoms at the face centers and Al atoms at the cube corners. Since both of them have a cubic lattice with similar lattice parameters, the γ' is coherent with the γ phase when the precipitate size is small. The dislocations at the

interface and ordered γ' phase which is difficult for dislocations to penetrate can strengthen the alloys.

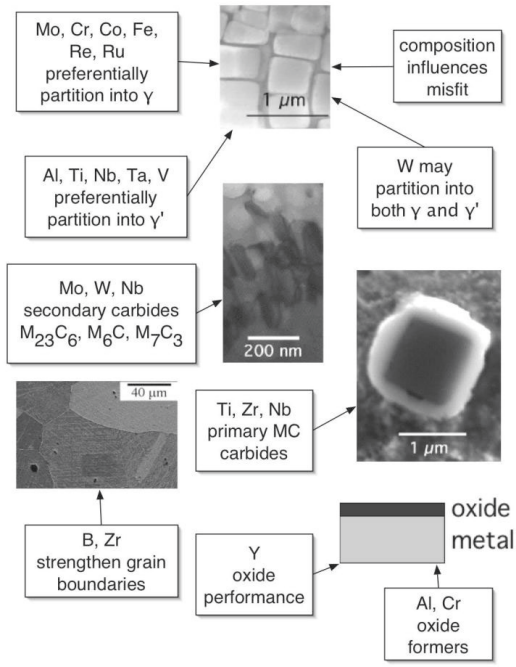

Fig. 2.7 Alloying element effects in nickel-based superalloys [50].

Except for Al, the properties of Ni-based superalloys can be tailored to a certain extent with an addition of other elements such as Cr, Fe, Co, Mo, W, Ta, Ti, Zr, Nb, Re Y, V, C, B and so on. Some alloys can contain up to 40 wt. % of a combination of non-Ni elements. The elemental addition can be grouped in to (a) γ phase former, elements that tend to precipitate to the γ matrix, such as Co Cr, Mo, W; (b) γ' former, elements that precipitate to γ' precipitates; (c) carbide former such as C, Cr, Mo, W, Ta, Hf and Ti, they tend to precipitate at the grain boundaries and reduce grain boundary sliding; (d) elements segregate to grain boundary such as Hf, Zr, W, Mo. The effect of alloys elements on Ni-based superalloys is illustrated in Fig. 2.7.

In this work, a superalloy named as IN738 was used as the substrate. IN738 is a vacuum melted, vacuum cast, precipitation hardenable Ni-based alloy. It has excellent high-temperature creep-rupture strength and corrosion resistance. The nominal composition (in weight percent) is listed in the Table 2.1.

Table 2.1 Nominal composition of IN738 in wt.%[51].

Substrate	C	Co	Cr	Mo	W	Ta	Nb	Al	Ti	B	Zr	Ni
	0.17	8.50	16.00	1.75	2.60	1.75	0.90	3.40	3.40	0.010	0.10	Balance

Normally, the alloy need to be heat treated in vacuum to achieve the best combination of mechanical properties. Firstly, they are isothermally kept at 1120 ˚C for 2 hours and then cooled down to room temperature; finally, they are heated to 845 ˚C and kept for 24 hours followed by air cooling to room temperature. Physical properties of IN738 are listed in Table 2.

Table 2 Physical properties of IN738 [51].

Density (g/cm^3)	Melting point (˚C)	Specific heat at 982 ˚C (J/g·˚C)	Thermal conductivity at 982 ˚C (W/m·K)	Mean thermal expansion from RT to 982 ˚C (/˚C)	Elastic modulus at 982 ˚C (GPa)	Poisson's ratio	Yield stress at 982 ˚C (MPa)
8.11	1230	0.711	26.0	1.59×10^{-5}	140	0.30	345

2.2.2 Bond coat and Thermally Grown Oxide (TGO)

The bond coat is an oxidation resistant metallic layer with a thickness of 100 to 200 μm, between the ceramic top layer and the superalloy substrate. The thickness varies typically as a function of processing techniques and service time [2]. The composition of the bond coat is quite complex as it needs to optimize a broad of thermal mechanical and thermal chemical properties. It is often made of MCrAlY alloys. M often refers to Ni, Co or a combination of both. Other types of bond coat, such as NiAl and PtAl bond coat can be deposited with diffusion aluminizing or chemical-vapor deposition in conjunction with electroplating. A Ni-Al-Cr ternary diagram at 1100 ˚C is presented in Fig. 2.8.

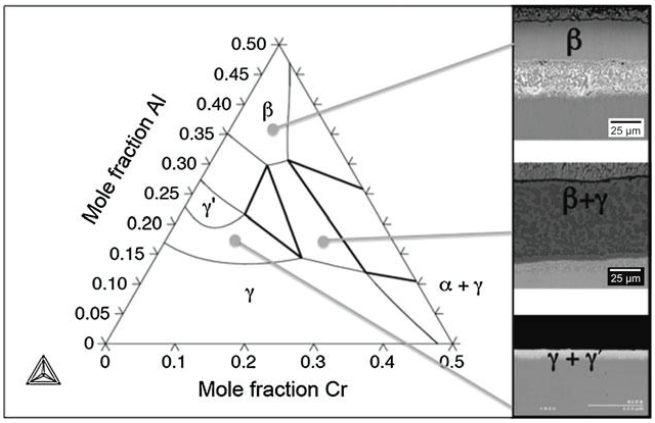

Fig. 2.8 The ternary Ni-Al-Cr phase diagram at 1100 ˚C and corresponding predominant phases at given chemical composition [52].

In the ternary compositional space, phases include β phase with an approximately equal level of Ni and Al, fcc γ-Ni phases, γ'-Ni_3Al phase and α-Cr phase. These phases are often present in the as-

sprayed bond coat. Based on the major phase constituents, bond coats can be roughly grouped into different classes. Coatings primarily comprised of β phase are referred to as nickel aluminide coatings. If they additionally contain platinum, they are calcified as platinum aluminides. For MCrAlY bond coats, they often consist of β phase and γ phase. And even, several emerging bond coats contain a mixture of γ' phase and γ Ni phase.

There are multiplicities of coating processes that are capable of covering complex geometries of turbine components with uniform bond coats. Generally, these bond coats can be classified into two groups: diffusion coatings and overlays coatings. The most used processes to apply diffusion coatings are pack cementation [53] and chemical vapor deposition [54]. The MCrAlY family bond coats, can be deposited with a number of processes. The most used processes are EB-PVD, which can deposit a high-quality bond coat with element additions. Low Pressure Plasma Spraying (LPPS) as a lower-cost alternative is also broadly used. In regard of cost, the cheaper processes include inert gas shrouded plasma spraying and High Velocity OxyFuel (HVOF) [55]. With further reducing particle temperature and increasing particle velocity, new processes such as activated combustion High Velocity Air Fuel (HVAF) and cold spray emerges recently [56]. Another example is Vacuum Plasma Spraying (VPS), with which dense, adherent, chemically homogeneous bond coat can be obtained [57]. The typical microstructure of MCrAlY bond coats sprayed with VPS and HVOF is presented in Fig. 2.9. The MCrAlY bond coat mainly contains two phases; Al-rich β-NiAl phase and γ-Ni phase. The presence of continuous matrix fcc γ phase can increase ductility and the thermal fatigue strength. The β phase serves as an Al reservoir in bond coat providing Al for the formation of TGO. With an increase of TGO thickness, the Al-rich phase at the outer region of the bond coat depletes and the γ becomes the predominant phase [58].

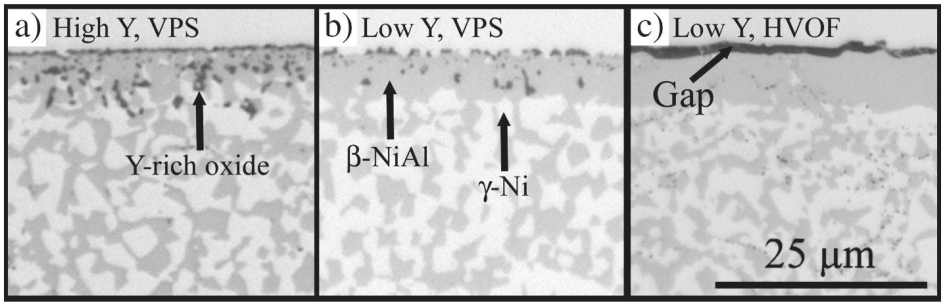

Fig. 2.9 Cross-section microstructure of MCrAlY bond coat after vacuum annealing; a) high Y, VPS coating; b) low Y, VPS coating; c) low Y, HVOF coating [59].

The bond coat must protect the metallic substrates from oxidation, as the outer ceramic top coat is permeable to oxygen. This requires bond coats which have the ability to form a layer of dense, protective oxide during service. The primary protective oxide is Al_2O_3. Although other elements can also form oxides; they are not as protective as Al_2O_3. Most bond coats presently contain a sufficiently high level of aluminum (8-12 wt.% for MCrAlY) to promote the formation of a dense α-

Al_2O_3 layer at the interface between ceramic top coat and bond coat. This Al_2O_3 layer has many characteristics: (a) slow growth rate; (b) resistant to corrosive species penetrated through ceramic top coat; (c) good cohesion with the top coat without reacting with it; (d) low oxygen diffusivity. This thin oxide layer is referred to as the Thermally Grown Oxide (TGO). Even though TGO can slow down oxidation of the underlying bond coat, it also introduces large thermal and growth stresses which can challenge the durability of TBCs [60, 61].

The growth of TGO during engine service is the most important phenomenon which is responsible for the spallation failure of TBCs. During the lifetime of TBCs, TGO undergoes thickening and elongation. The elongation is caused by new TGO formed on internal grain boundary; while the thickening is caused by a new TGO formed at the TGO/bond coat interface. The growth of TGO can lead to a constrained volume expansion. A compressive growth stress with a level of about 1 GPa can be formed. Due to the thermal expansion mismatch between the TGO and bond coat, upon cooling, a very high compressive thermal stress (1-3 GPa) can be formed at ambient temperature. The strain energy in TGO increases linearly with TGO thickness. And often, as TGO thickness exceeds critical thickness, failure of TBCs occurs [62].

The formation and growth of α-Al_2O_3 results in the depletion of Al in the bond coat. If severe, it can result in fast growth oxides, such as Ni and Co containing spinels, $Y_3Al_5O_{12}$ and Y_2O_3. These fast-growing oxides could compromise the integrity of TGO and accelerates oxidation. During cycling, for EB-PVD TBCs, the roughening of bond coat/TGO/ceramic top coat occurs due to cyclic creep of bond coats, leading to out of plane stress normal to the interface of bond coat/top coat interface. This stress along with interfacial imperfection is primarily responsible for the failure of EB-PVD TBCs [10]. Images of TGO in TBCs are presented in Fig. 2.10.

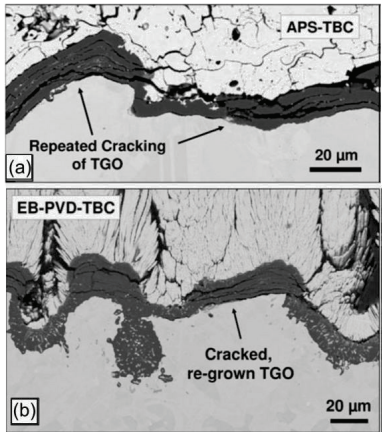

Fig. 2.10 SEM images of TGOs: (a) cyclically oxidized (at 1050 ˚C) APS TBCs with NiCoCrAlY bond coat; (b) cyclically oxidized (at 1000 ˚C) EB-PVD TBC with NiCoCrAlY bond coat [60].

The adhesion of TGO with bond coats is also important to the durability of TBCs. Some deleterious elements such as S can weaken the bonding, while other elements such as Pt, Y, Hf, can increase the adhesion [2].

2.2.3 Ceramic Top Coat

The main function of the ceramic top coat in TBCs system is providing thermal insulation for the metallic substrate and bond coat. This layer has an intermediate thickness (100 μm to 1 mm) with a high porosity (typically 15 %), which is essential for high strain tolerance and reducing the thermal conductivity of top coats. Furthermore, top coats need to be mechanically resistant to fracture, erosion, and foreign object damage. The top coats also need to be deposited on a complex shaped surface. Although, there are many methods to deposit ceramic top coat on a metallic substrate; currently, top coats are mainly deposited by Air Plasma Spraying (APS) and Electron Beam-Physical Vapor Deposition (EB-PVD). The microstructures of APS TBCs and EB-PVD TBCs are very different. The details of these deposition processes and microstructure of deposited coatings will be introduced in section 2.3.

Considering the extremely harsh operating environment of TBCs, the requirements for materials are: (a) high melting point, (b) low thermal conductivity, (c) good thermal phase stability (d) chemical inertness, (e) high sintering resistance, (f) similar Coefficient of Thermal Expansion (CTE) with metallic substrate. The state of art top coat material is Y_2O_3 partially Stabilized ZrO_2 (YSZ) [63]. As mentioned before, the first TBCs consisting YSZ top coat was developed by NASA in the middle of 1970s. Subsequently, the composition of YSZ was optimized by Stecura [64]. It was found that YSZ with Yttria content of 6–8 wt.% has the best performances. YSZ has a suite of desirable properties that make it the most widely used top coat material. YSZ has a relatively low thermal conductivity at elevated temperature (2.3 $Wm^{-1}K^{-1}$ at 1000 ˚C for fully dense material) [27]. This could be attributed to its high concentration of point defects (oxygen vacancies and substitutional solute atoms), which scatter heat conducting phonons [65]. The YSZ also has a high melting point (2700 ˚C) [23]. The density of YSZ is about 6.0 g/cm^3[27], which is important for parasitic-weight consideration in turbine engines. It has a high hardness (~14 GPa) and high fracture toughness (~3 $MPam^{-0.5}$) [20, 27]. The high fracture toughness of YSZ does not arise from the martensitic transformation (an irreversible diffusionless collective atom movement) from tetragonal to monoclinic phase but from reversible ferroelastic domain switching from one tetragonal variant to another when stressed [66]. Unlike transformation toughening, ferroelastic toughening can operate at high temperature. This makes it resistant to erosion and foreign object impact at high service temperature. YSZ also has a high CTE (11×10^{-6} K^{-1}), which is close to that of the underlying substrate (14×10^{-6} K^{-1}). This will help to mitigate stress arising from the thermal expansion mismatch; however, a difference still remains. This will lead to thermal stress and crack propagation within the top coat. By introducing porosity, cracks into the top coats or depositing columnar structures, the thermal stress level is reduced and the strain tolerance is increased. Thus a better performing TBC can be achieved. This will be discussed in the following part. Even though, YSZ has so many advantages, as listed before, some

weak points such as insufficient phase stability and accelerated sintering at temperatures above 1200 ˚C, limit the application of YSZ in TBCs[27].

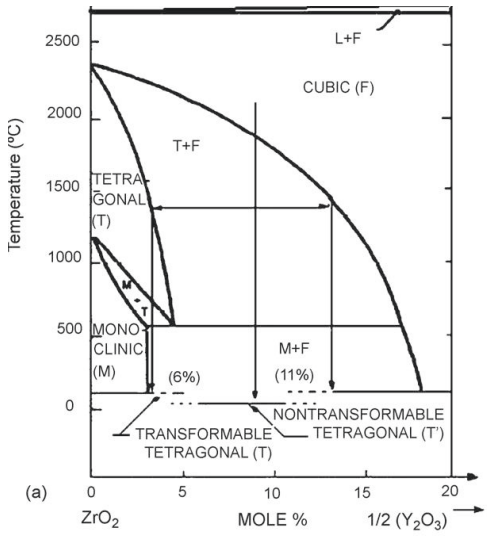

Fig. 2.11 ZrO_2-Y_2O_3 phase diagram [67].

As described in Fig. 2.11. YSZ exits as three different polymorphs: monoclinic (m), tetragonal (t) and cubic (c) which depend on composition and temperature. For 6-8 wt% YSZ, a non-equilibrium phase (t', non-transformable tetragonal phase) can be observed in as-sprayed coatings at room temperature. This is due to the fast cooling process which prevents necessary atoms rearrangement for the formation of transformable tetragonal phase and cubic phase. This phase is the preferred phase for TBCs, as it tends to have the best combination of thermal-mechanical properties and phase stability [68]. However, the t' phase undergoes phase transformation into equilibrium phase (tetragonal and cubic phase) at a temperature higher than 1200 ˚C. Upon cooling, the tetragonal phase turns into monoclinic phase accompanying a large volume change (~4 vol%). This volume change is detrimental to the cycling lifetime of TBCs [66]. The cubic phase is also a non-desired phase, as it has a lower fracture toughness (~ 1 $MPa{\cdot}m^{-0.5}$) compared with t' phase. It can lead to inferior cycling lifetime of TBCs. Furthermore, the enhanced sintering of YSZ at high temperature leads to a decrease in the porosity and an increase on the elastic modulus. With an increase of elastic modulus, a thermal stress is also increased, which can lead to crack propagation in the top coat leading to TBC failure [69].

Except for intrinsic issues which lead to degradation of top coats, there are also extrinsic degradation mechanisms such as erosion, foreign object damage, hot corrosion and CMAS attack. They will be specifically illustrated in the following part.

Erosion and foreign object damage

Solid particle erosion including foreign object damage is another failure mode for top coats. This especially is the case for gas turbines operated in a sandy or ashy environment. Even for land-based turbine engines, where the air is filtered before entering the compressor, solid particle erosion can also take place [70]. Owing to their relatively large inertia, solid particles do not follow the streamline and impact on the fast rotating components. Finally, it leads to the erosion of protective coating from the underlying substrate. Erosion mechanisms in APS and EB-PVD coatings are significantly different. This can be attributed to their different microstructures. The typical erosion failure modes for APS and EB-PVD coatings are presented in Fig. 2.12.

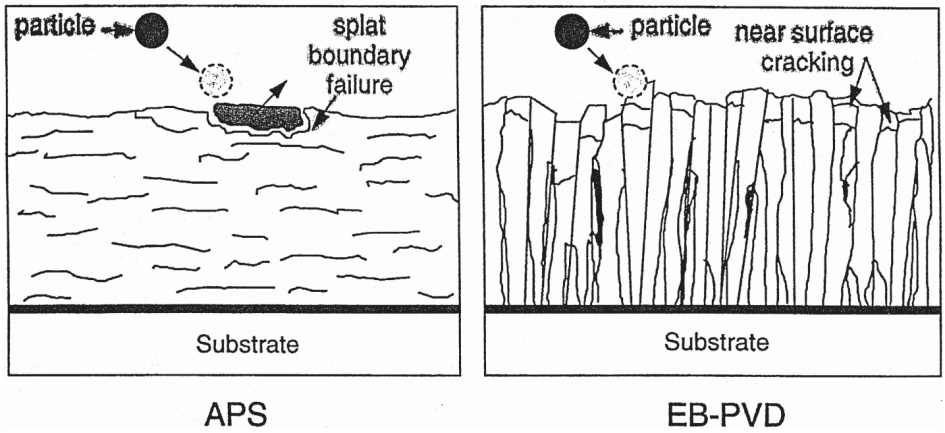

Fig. 2.12 A schematic diagram of the failure modes for APS and EB-PVD TBCs [71].

For APS TBCs, three different types of solid erosion can be distinguished [72]:

(a) Primary scars as the main observable feature on erosion surface.

(b) Occurrence of fractures around the impact area on coating surface.

(c) Tunnel formation on the surface.

In the case of (a), the impacting particles can make indentations on the surface. The erosion is mainly caused by successive impacts on the deformed surface. In the case of (b), impactions lead to cracks which propagate along the splat boundaries. In the case of (c), the kinetic energy of impacting

particle transferred to coatings is high enough to cause connection of pre-existing pores inside TBCs. This can lead to spallation of splat clusters [70].

As founded by Eaton et al. and Novak et al., the higher the strength of TBCs is, the lower the erosion rate can be obtained. When the overall porosity of the coatings is fixed, the erosion rate increases as a function of the specific surface area of the porosity [72]. Nichols et al. and Li et al. reported that erosion of APS TBCs is due to the spallation of surface lamellas. The erosion rate is determined by the propagation of cracks along the interface between two neighbor lamellae [73]. This indicates that the stronger the bonding between splats is, the lower the erosion rate can be. Li built a model to describe the erosion rate as:

$$W_e \propto \frac{\rho_c E_{eff}}{K_{IC}} \tag{2.1}$$

where ρ_c is the density of the coating; E_{eff} is the fraction of kinetic energy per unit mass of impacting particles; K_{IC} is the fracture toughness of the coating along lamella direction [74].

For EB-PVD columnar TBCs, the erosion mode is different from that of APS TBCs. Three possible modes were reported:

(a) Near-surface cracking/lateral cracking. When small particles impact on EB-PVD TBCs with sufficient low speed, the top 20 μm of individual columns are cracked due to the impaction. In this mode, only elastic strain can be found and the cracks propagate along the direction parallel to the top coat/bond coat interface. These cracks are caused by tensile stress which is promoted by the elastic waves moving forward and backward along each single column.

(b) Compaction damage. Due to a higher impulse of partials compared with mode (a), a densification of top coat (1 – 20 μm in thickness) which is caused by a plastic deformation can be observed. The cracks can propagate at the interface between the densified layer and underlying columns. This can be attributed to the stress concentration caused by particle impaction.

(c) Foreign object damage. When particles with high impulse impact on EB-PVD TBCs, most of the kinetic energy is absorbed by the plastic deformation of coatings. This deformation accompanys kink bands around the perimeter of the plastic zone. These crack bands propagate conically through the top coat and turn parallel to top coat/bond coat interface when they approach to the interface.

Hot corrosion

Low-quality fuels usually contain impurities such as Vanadium (V) and Sodium (Na). These impurities can form Na_2SO_4 and V_2O_5 salts on the surface of TBCs. These strong acidic or alkaline oxides can attack both the ceramic and metallic components of TBCs. This phenomenon is called hot corrosion. Hot corrosion of TBCs can be grouped into four different modes: chemical reaction, “mineralization”, corrosion of bond coat, physical damage by molten phase penetrating into the TBCs [75].

For chemical reaction mode, the Yttria in YSZ readily reacts with V_2O_3 and forms YVO_4. This can deplete Yttria from YSZ, promote the phase transformation of YSZ and finally leads to spallation of TBCs. Mineralization is a type of phase reaction involving a non-reactive liquid which tends to move stressed or non-equilibrium phase toward equilibrium [75]. The typical example is that molten $NaVO_3$ can mineralize CeO_2 stabilized ZrO_2. In some cases, the molten impurities can penetrate through the ceramic layer to react with bond coat. It was found that the vaporous NaCl can cause the formation of fast-growing, thick, un-protective Al_2O_3 on the surface of bond coats. This can also promote spallation of TBCs. For physical damages, the molten oxides penetrate into the porous ceramic layer and fill into voids and column gaps. This will reduce strain tolerance of TBCs and promote failure of coatings.

In regards of hot corrosion, many approaches have been introduced to increase the hot corrosion resistance of TBCs, such as increasing yttria content in YSZ [76], sealing TBC surface [77] and seeking new corrosion resistant stabilizer for ZrO_2 [78]. Furthermore, fuels have become cleaner; the hot corrosion problem for TBCs has been greatly relieved.

CMAS attack

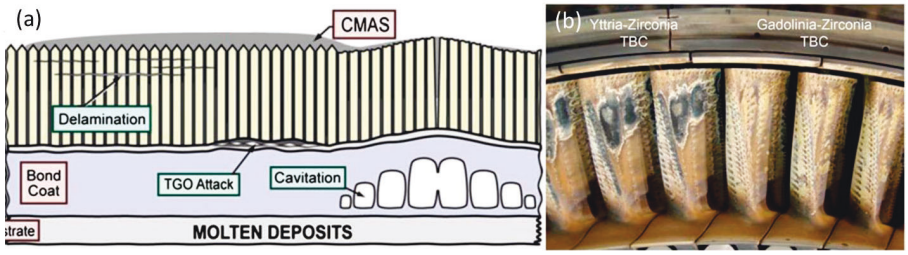

Fig. 2.13 (a) Identified TBCs failure mechanism attacked by CMAS and (b) example of CMAS attack on current airfoils (left part is coated with YSZ TBCs and the right part is coated with $Gd_2Zr_2O_7$ TBCs) [79, 80].

As a result of high service temperature of TBCs in advance turbine engines ($\geqslant$ 1200 ˚C), low melting point salts become a problem for some TBC applications. The ingestion of siliceous debris (airborne dust, sand, volcano ash) can lead to glassy melts based on Calcium-Magnesium Alumino-Silicates (CMAS). These glassy melts can wet all ceramic coating materials of interest. This leads to a series of problems, such as penetration of void space of the TBCs and reduced strain tolerance of coatings; chemically dissolving of materials followed by a precipitation of modified oxides. Furthermore, CMAS seems to affect more and more engines in the future, as high performances of engines induce increasing operating temperature. Finding a solution to CMAS problems has attracted intensive focus since last decade [81, 82]. Although researches on CMAS attack on TBCs are relatively new; important insight on CMAS attack and the transport mechanisms of CMAS have emerged [82-84]. It has been noticed that TBCs with high CMAS resistance need to be non-wetting with CMAS or easy to

react with CMAS forming a crystalline dense layer which can prevent further penetration of CMAS [85, 86]. In contrary, TBCs made of ceramics which are inert or stable in contact with molten CMAS might have poor CMAS resistance in reality.

The main failure mode for CMAS attack is summarized in Fig 2.13. If the CMAS reaches the TGO, it can chemically react with TGO leading to delaminations along the TGO. In some cases, the CMAS can also promote creep cavitation in the bond coat, which can lead to the propagation of cracks within the bond coat instead of the ceramic top coat [85]. Furthermore, the penetration of CMAS can lead to the degradation of thermal conductivity [87]. This can aggravate other failure modes which are nominally unrelated to the CMAS attack. Delamination of APS and EB-PVD TBCs under CMAS attack was investigated by Mercer [83] and Krämer et al. [88]. It seems that the failure features for both kinds of coatings are quite similar. Two types of degradation mechanism on the ceramic top coat are identified: the thermo-mechanical failure and the thermo-chemical failure [87].

When the temperature is high enough, glass deposits on coating surface melts and infiltrates the porous or columnar TBCs microstructure. Upon cooling, the melt freezes and the infiltrated TBC becomes rigid, losing part of its strain tolerance. Cracks can develop in ceramic top coat and lead to progressive TBCs failure during service. The thermo-mechanical failure is considered as the most detrimental one to TBCs [82, 87]. The driving forces behind this failure are briefly summarized by Carlos G. Levi et al. [80]. The driving force for the delamination of TBCs can be attributed to the releasing of strain energy stored in the coating during cycling. The major source of this strain energy is thermal expansion mismatch between the ceramic top coat and the metallic substrate. To get a better insight of CMAS failure mechanism, a model based on rapid cooling scenario was built by Carlos G. Levi et al.. In order to make the model be realistic to thermal gradient test, a TBCs system with a superalloy substrate (3.5 mm in thickness) and a homogeneous YSZ ceramic layer (1 mm in thickness) is assumed. The transient temperature history which is computed by considering heat transfer of cooling air and radiation cooling of the rear side is presented in Fig 2.14. ΔT_{sub} is the temperature drop on the substrate; while $\Delta T_{sur/sub}$ is the temperature drop on the surface relative to the coating/substrate interface [80]. As shown in Fig. 2.14 (a), the surface of the coating is fast cooled down within the first several seconds and the $\Delta T_{sur/sub}$ peaks at about 650 ˚C, while the temperature drop on the substrate is still limited. With the progress of cooling, the substrate is cooled to room temperature, while $\Delta T_{sur/sub}$ approaches to a value of about 350 ˚C which is contributed by the initial temperature gradient across the coating.

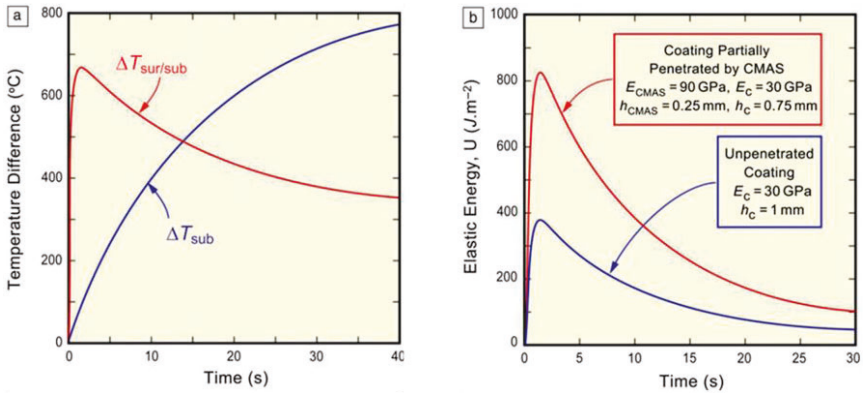

Fig. 2.14 Transient temperature of the substrate (ΔT_{sub}) and coating surface relative to the substrate surface ($\Delta T_{sur/sub}$) (a); evolution of elastic energy in un-penetrated coating and CMAS penetrated coating during cooling process (b) [80].

Transient elastic energy history based on transient temperature is presented in Fig. 2.14 (b). And also the elastic energy of a 1 mm coating with a 0.25 mm CMAS penetrated dense layer is presented in Fig. 2.14. It reveals that the coating experiences a peak in elastic energy within 2 seconds. More importantly, coating penetrated by CMAS experiences a double of peak energy. Therefore, coatings penetrated by CMAS are more susceptible to a delamination under rapid cooling. This can explain why CMAS penetration can decrease the lifetime of TBCs from the thermo-mechanical aspect.

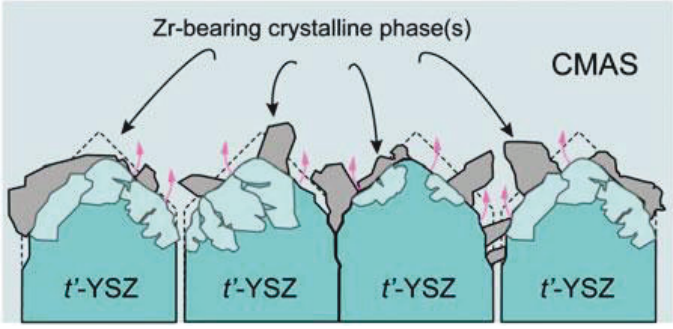

Fig. 2.15 Schematic illustration of the dissolution-reprecipitation mechanism in YSZ [80].

Thermo-chemical aspects are also very important to understand CMAS related TBCs failure. One key challenge in understanding thermo-chemical interaction between CMAS and TBCs is the uncertainty in the amount and chemical composition of glass deposit on the coating surface. It not only contains oxides which originate from the natural mineral source but also contains oxides originating from the

engine components such as NiO, TiO_2 and ZrO_2 [79]. Concentrations of predominant oxide in CMAS from the mineral source, engines deposits and also model CMAS are given in ref [80]. The infiltrated CMAS were reported to have dissimilar compositions for a wide variety of deposits, loadings and severity of exposure [89]. For laboratory approaches aiming to replicate the interaction in service, a simplified CMAS deposit mainly containing SiO_2, CaO, MgO and Al_2O_3 (in some cases FeO_x is additionally included) is used.

The primary interactions between CMAS and ceramic top layer are the dissolution and the precipitation. The precipitates mainly contain one or more compositionally modified crystalline phases [82, 87]. Reported by Krämer, J. el al., t' YSZ can dissolve isothermally in CMAS melt and reprecipitate either Y-lean ZrO_2 which transforms to monoclinic phase upon cooling, or fully stabilized Y-rich cubic ZrO_2 which has a lower fracture toughness [82]. The product depends on the alumina content of the CMAS melts [90]. Furthermore, in other experiments, products such as $Ga_2ZrSi_4O_{12}$ [80], $ZrSiO_4$ [91] and tetragonal YSZ [91] were also observed. After cooling, the residual CMAS generally is in an amorphous phase.

To slow down the penetration of CMAS in YSZ, two strategies based on reactivity are developed. One is using Alumina as the key reactant. Alumina can combine with CaO and SiO_2 to form anorthite $GaAl_2Si_2O_8$ [92, 93]. In this approach, Al_2O_3 and TiO_2 in form of solid solution have been incorporated into YSZ TBCs. The top coat can serve as a reservoir of Al and Ti solutes. When the CMAS penetrates TBCs, an accumulation of Al in CMAS can turn CMAS from the amorphous phase to crystallize anorthite phase [90]. Ti in the glass can promote crystallization of CMAS by working as a nucleating agent.

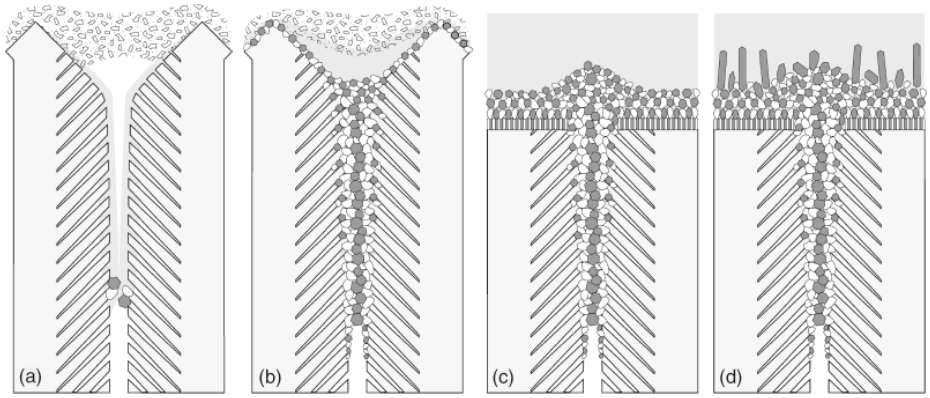

Fig. 2.16 Illustration of the sequence of events that leads to the sealing of column gaps owing to the chemical interaction of CMAS with GZO [84].

The other strategy is based on Rare-Earth (RE) zirconates, represented by $Gd_2Zr_2O_7$ (GZO) [84, 94]. The GZO dissolves into the CMAS melts and precipitates a $Zr(RE,Ca)O_x$ fluorite phase combined with

a highly stable apatite silicate with nominal composition $Ca_2RE_8(SiO_4)_6O_2$. An infiltration inhibiting mechanism was found by Stephen Krämer et al. in EB-PVD TBCs. [84]. The inhibiting mechanism is presented in Fig. 2.16. (a) The CMAS melt rapidly wets the inner surfaces of columns and lead to the formation of a limited amount of fluorite phase which is a result of re-precipitation of GZO, and apatite phase which is the reaction product. (b) The precipitates fluorite and apatite phase firstly fill the narrow gaps in where the supersaturation is achieved earlier. The columnar gap is sealed and covered with a dense reaction product layer. This layer can work as a diffusion barrier layer and hinder further penetration of CMAS melt. (c) Column tips are gradually infiltrated by CMAS forming a graded microstructure. This process progresses at a much lower rate. (d) Additional growth of crystalline phase takes place upon cooling.

As shown in previous Fig. 2.13 (b), GZO TBCs exhibit much better performances than YSZ TBCs under the CMAS attack. It seems GZO is a high potential candidate material against CMAS. Isothermal furnace cycle tests can lead to misleading results and also 1300 ˚C and above testing temperature cause serious degradation of the superalloy. Therefore, thermal gradient tests are essential for the thermo-mechanical assessment of CMAS infiltrated TBCs. A burner rig has been modified by D. E. Mack et al. to inject CMAS precursor solutions through the flame and was used successfully for testing plasma sprayed coatings [95]. The detailed set up of this burner rig facility will be introduced in section 3.

The essence of CMAS failure in TBCs is a thermo-mechanical failure, with a thermo-chemical issue relating to mitigation strategy. As the driving force for delamination scales is square of the temperature drop according to the model built in ref. [2], the CMAS problem is expected to be more serious in the future with the increase of surface temperature. The largest challenge for CMAS research is searching for a new ceramic oxide with better CMAS resistance and high fracture toughness.

2.2.4 New Ceramic Top-coat Materials

To against the drawbacks of YSZ, such as relatively high thermal conductivity, phase transformation, fast sintering at high temperature, poor CMAS resistance, various approaches were found. Over the last 20 years, primarily four different ceramic material groups have been suggested as promising new ceramic materials for TBCs: (a) zirconia doped with different rare earth oxides, (b) perovskites, (c) hexaaluminates, (d) pyrochlores.

Zirconia stabilized with rare earth oxides

To slow down the phase transformation and get a lower thermal conductivity, stabilizer other than Yttria has been investigated. Zirconia stabilized with rare earth oxides, such as Gd_2O_3, Yb_2O_3 and Nd_2O_3, has better thermal conductivity than YSZ [27, 96, 97]. Other approaches, such as co-doping zirconia with two or more oxides, adding paired dopants (Gd_2O_3, Nd_2O_3) into YSZ system were also reported [98-100]. Due to the significant difference between the ionic sizes of the zirconia and RE, a highly defective lattice is produced while thermodynamic stability can be preserved[20]. For

example, zirconia doped with Nb_2O_5, Nb_3O_5 and Y_2O_3 can get a 40 % reduction on thermal conductivity [101]. Additionally, the thermal stability of zirconia is also improved by doping. Increased or similar cycling performance compared to conventional YSZ was observed at similar dopant level. However, reduced thermal cycling performance was also observed at higher dopant levels. This mainly can be attributed to the reduced fracture toughness by doping [100, 102].

Perovskites

The ABO_3 type perovskites are a class of materials with a lot of advantages as TBC materials such as low thermal conductivity, high melting point. Pure ABO_3 perovskite $SrZrO_3$ has a thermal conductivity of 2.1 W/mK at 1000 ˚C. Additionally, a further 20 % reduction on thermal conductivity can get on $SrZrO_3$ by doping Yb_2O_3 on B site [103]. At 730 ˚C, $SrZrO_3$ undergoes an undesired phase transformation from orthorhombic to tetragonal. But this transformation can be suppressed by doping with Gd or Yb. Moreover, increasing doping level can lead to new complex perovskite structures. For example, $Ba(Mg_{1/3}Ta_{2/3})O_3$ has a melting point about 3000 ˚C and is considered as the most refractory oxide. Its thermal conductivity can reach to 2.5 W/mK at 1100 ˚C. Similarly, $La(Al_{1/4}Mg_{1/2}Ta_{1/4})O_3$ shows a low thermal conductivity (~ 2W/mK) and a high coefficiency of thermal expansion (~11.9×10^{-6} K^{-1}). Although the bulk properties of perovskites show promising values, their toughness is till inferior compared to YSZ. This leads to poor thermal cycling performances of perovskite materials. The difference in vapor pressure of component oxides also leads to preferential volatilization of non-zirconia constituents during the spraying process [104].

Hexaaluminates

Among hexaaluminates, Lanthanum hexaaluminates with a magnetoplumbite structure is the most investigated material and is a promising competitor to YSZ as TBC materials [105]. They have a high melting point, high thermal expansion, low thermal conductivity, excellent sintering resistance and thermal stability up to 1800 ˚C. $LaMgAl_{11}O_{19}$ as the most promising one has attracted extensive investigations with APS. Due to the fast quenching from molten phase, some amorphous phase can be found in as-sprayed APS coatings. Upon heating up to a temperature range from 800 to 1200 ˚C, a large volume shrinkage which can be attributed to recrystallization of amorphous phase can be introduced. Recrystallization has been considered as the main drawback of plasma sprayed hexaaluminate coatings. The volatilization of Mg also introduces difficulties in the deposition of the coating by EB-PVD [8]. Recently, another hexaaluminate $LaTi_2Al_9O_{19}$ was reported as a novel TBC material [106]. It has low thermal conductivity (1.0-1.3 W/mK) and phase stability up to 1600 ˚C. The coefficiency of thermal expansion can reach to a range of 8-10 × 10^{-6} K^{-1}. However, its low fracture toughness (0.8-1 $MPam^{1/2}$) limits its application.

Pyrochlores

Pyrochlores are a relatively new group of ceramic materials for TBCs. They show a lot of advantages for applications at service temperature above 1300 ˚C. Among numbers of pyrochlores with $A_2B_2O_7$ structure, lanthanides zirconates attracted a lot of interest. The lanthanides can be one or

combination of La, Gd, Sm, Nd, Eu and Yb. And also hafnia and ceria-based materials were also found to be interesting [100]. Lanthanides zirconates have low thermal conductivity and excellent phase stability. Their low thermal conductivity can be attributed to a high concentration of intrinsic oxygen vacancies, high-level cation substitution and a large atomic mass difference between zirconia and large lanthanides. This difference can increase the phonon scattering strength of point defects [107]. The thermal conductivity of $Ln_2Zr_2O_7$ (Ln: La, Nd, Sm, Eu, Gd) were reported to be 1.2 to 2.2 W/mK. A further reduction in thermal conductivity can be obtained by cation doping. Lehmann et al. showed that doping $La_2Zr_2O_7$ with heavier Lanthanides (Nd, Eu, Gd) could further decrease the thermal conductivity of pyrochlores. Furthermore, as reported by L. Guo et al., Yb_2O_3 doped $Gd_2Zr_2O_7$ exhibited lower thermal conductivity than $Gd_2Zr_2O_7$ [97]. $(Gd_{0.9}Yb_{0.1})_2Zr_2O_7$ exhibited the lowest thermal conductivity with a value of 0.9 W/mK at 1200 ˚C. High-temperature phase stability is another advantage of $Ln_2Zr_2O_7$. All of them have a stability temperature higher than 1500 ˚C which is beyond the requirements of advanced turbine engine on TBCs. For $La_2Zr_2O_7$, it can keep stable until to the melting point (2283 ˚C). $Gd_2Zr_2O_7$ has the lowest stability temperature at about 1550 ˚C. Even with high phase stability, phase transformation in pyrochlore coatings ($Ln_2Zr_2O_7$, Ln: La, Sm, Gd) can also be found during service. Defect fluorite phase which is equilibrium phase at high temperature can be found in as deposited coatings deposited by plasma spraying or EB-PVD. Upon heating to a temperature above 1000 ˚C, the un-equilibrium fluorite phase undergoes a phase transformation to equilibrium pyrochlore phase. The formation of fluorite phase in the as deposited state is typically attributed to fast cooling rate during spraying with which the ordering process is kinetically suppressed. Fortunately, no detrimental effect of this phase transformation on thermal cycling performance of coatings can be found [108].

High coefficient of thermal expansion is another advantage of $Ln_2Zr_2O_7$ (Ln: La, Nb, Sm, Eu, Gd). They have CTEs ranging from 9.1 to 12.2 × 10^{-6} K^{-1} at 1000 ˚C. The CTEs of pyrochlores are close to that of YSZ (11 × 10^{-6} K^{-1}). Furthermore, CTEs of pyrochlores can be further increased by doping. It was found by Guo et al., doping Yb into $Gd_2Zr_2O_7$ can increase CTE [97]. CTE value scales to the amount of doping Yb. At 1200 ˚C, the CETs of Yb_2O_3 doped $Gd_2Zr_2O_7$ ceramics were in a range of 11.8 × 10^{-6} K^{-1} to 13 × 10^{-6} K^{-1}, which are comparable to or even larger than those of YSZ. Increased CTE was also found on TiO_2 doped $Gd_2Zr_2O_7$. $Gd_2(Zr_{1-x}Ti_x)_2O_7$ (X =0.2) shows an increased CTE (11.8 × 10^{-6} K^{-1}) at 1000 ˚C [109].

$Gd_2Zr_2O_7$ as the most promising TBC material has attracted intensive interest since the last two decades. It has been reported that $Gd_2Zr_2O_7$ has been in operation in engines for several years [80]. In the following part, the properties of $Gd_2Zr_2O_7$ will be highlighted. Except for the low thermal conductivity (1.2 W/mK), high melting point (2283 ˚C) and very good phase stability as mentioned before, $Gd_2Zr_2O_7$ also shows excellent CMAS resistance. As mentioned in section 2.2.3, $Gd_2Zr_2O_7$ reacts with CMAS resulting into highly stable apatite $Ca_2Gd_8(SiO_4)_6O_2$ phase. This crystalline phase seals off the top of the EB-PVD coating and prevents further CMAS penetration. Also, the competition of CMAS penetration with reaction and crystallization hinders the penetration of CMAS. Similar results were also found from APS $Gd_2Zr_2O_7$ coatings.

Drexler et al. have compared penetration of CMAS on different pyrochlores ($Ln_2Zr_2O_7$, Ln: Yb, Gd, Y). It was found all pyrochlores have more excellent CMAS penetration resistance than YSZ. The penetration depths of pyrochlores are only about one-tenth of that of YSZ. $Gd_2Zr_2O_7$ exhibits the deepest penetration. The author's hypothesis was that, as more RE^{+3} cation incorporation is required to form Gd apatite than the Y or Yb apatite. The CMAS melt needs to penetrate deeper to accumulate a sufficient amount of RE^{+3} [110]. Hot corrosion resistance of $Gd_2Zr_2O_7$ was also investigated by Habibi et al. [111]. For conventional YSZ, the reactions between yttria and $V_2O_5/NaVO_3$ produces YVO_4, leaching Y_2O_3 from YSZ and causing phase transformation. Thus conventional YSZ is very vulnerable under hot corrosion attack. But $Gd_2Zr_2O_7$ showed much better hot corrosion resistance than YSZ.

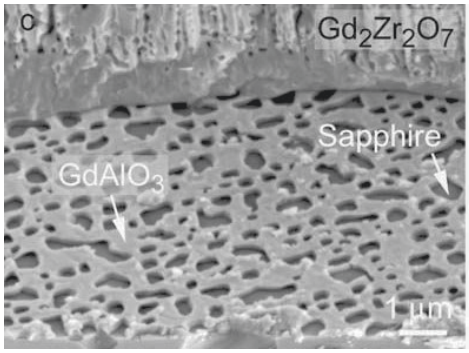

Fig. 2.17 SEM image on a porous reaction layer attached to sapphire (Al_2O_3) after partial spallation of the coating [29].

Apart from the advantages of $Gd_2Zr_2O_7$, some difficulties have been reported for $Gd_2Zr_2O_7$ TBCs. Reported by Leckie et al. [29], ZrO_2 compositions with $GdO_{1.5}$ >32%, when used as TBCs, tends to react with underlying TGO to form a porous $GdAlO_3$ interphase (as shown in Fig. 2.17), compromising the integrity of the system and eventually damaging the protective function of the TGO. It is suggested that a suitable diffusion barrier layer (e.g., YSZ) preclude the reaction with TGO. The chemical reaction formula is listed as following:

$$Gd_2Zr_2O_7 + Al_2O_3 \rightarrow 2GdAlO_3 + 2ZrO_2$$

The porosity of $GdAlO_3$ found at the interface is about 30 %. The volume change for the above reaction is about 9 vol%. This volume change account only for about 1/3 of the pore volume. However, the reason for high porosity is still not clear.

Relatively Lower fracture toughness of pyrochlores is another reason that limits their applications. Fracture toughness of $Gd_2Zr_2O_7$ reported by Guo et al. is only about 0.8 $MPam^{1/2}$, which is much lower than that of YSZ (2.6 $MPam^{1/2}$) [112]. Lower fracture toughness could lead to early failure of

pyrochlore TBCs as reported by Vassen et al. [8]. One way to overcome this drawback is to utilize multilayer concept. By spraying a high fracture toughness YSZ intermediate layer between pyrochlore and substrate, thermal cycling performance of pyrochlore can be greatly increased, as shown in Bakan's work [113]. Other trials such as doping, adding high fracture toughness ceramic, reducing RE_2O_3 content were also used to toughen $Gd_2Zr_2O_7$. As reported by Guo et al., $Gd_2Zr_2O_7$ with an addition of 60 mol% Dy stabilized zirconia has a fracture toughness value of 1.82 $MPam^{1/2}$, which is twice of that of $Gd_2Zr_2O_7$ [114]. Fracture toughness of $Gd_2Zr_2O_7$ can also be increased to 1.5 $MPam^{1/2}$ by doping Sc [112]. Schmitt et al. tried to reducing $GdO_{1.5}$ content from 50 mol% to 15.66 mol% and an increased fracture toughness with a value of 1.25 $MPam^{1/2}$ was obtained [115].

In summary of new ceramic top coat materials, a number of efforts have been taken for decades to search for even better ceramics than YSZ. Generally, they can be grouped into zirconia stabilized with rare earth oxides, perovskites, hexaaluminates, and pyrochlores. Among them, pyrochlores, especially $Gd_2Zr_2O_7$, with a combination of a lot of merits attracted the most intensive attention. In addition, a lot of methods such as doping, optimizing chemical composition were used to further promoting their performances.

2.3 Ceramic Top-coat Deposition Technology

The widespread utilization of TBCs has been realized by the development of advanced deposition technologies. The refractory nature of TBC materials with melting points approaching or in excess of 3000 K, requires ultra-high temperature materials processing capabilities. The two mainly used heating sources are thermal plasmas and electron beams. Based on different heating sources, different spaying technologies were developed. The two most widely used spraying technologies are Atmosphere Plasma Spraying (APS) and Electron Beam-Physical Vapor Deposition (EB-PVD). APS TBCs can be applied to aero engine components including combustors, vanes and turbine shrouds. They are also sprayed on both rotating and stationary parts of large land-based power generation engines. EB-PVD TBCs are mainly applied to rotating turbine blades of aircraft engines.

In addition to materials, the coating defected architectures facilitated by processing are another critical aspect of TBCs. Both APS and EB-PVD coatings contain 10–30 % of porosity contributed by defects. These porosities can further reduce the thermal conductivity of YSZ. Especially, as-sprayed APS coatings can show as low as 20 % of bulk value [5]. Defects also impart compliance of the TBCs which is critical to thermal cycling performance of TBCs. Taking EB-PVD TBCs as an example, they possess a feathery microstructure with vertical separations which offers excellent compliance during thermal cycling. Due to the excellent compliance, EB-PVD TBCs exhibit enhanced durability during service [2]. Similarly, typical APS TBCs have a lamellar microstructure built by discrete splats. This lamellar microstructure with pores, interfaces and cracks can also offer compliance, but to a lesser extent than the vertical separations. Controlling microstructures of TBCs by processing is very important to impart advanced properties to TBCs. There has been significant progress both in industry and academia to combine the advantages of APS and EB-PVD.

Plasma spray process has been modified to produce physical vapor deposited TBCs. This novel technology is called Plasma Spray-Physical Vapor Deposition (PS-PVD). The plasma torch is put into a high vacuum chamber instead of atmosphere. By reducing pressure in the chamber, plasma plume length can be extended from a few 100 mm to 1.5 m. This makes it possible to evaporate powder feedstock and achieve advanced microstructures (thin and dense, columnar structured) with non-line of sight deposition and high deposition rate[3]. Due to the high requirements on vacuum and equipment, the cost for PS-PVD TBCs remains high.

Suspension Plasma Spraying (SPS) is another relatively new spraying process based on plasma spraying. By introducing suspension instead of powder into the thermal plasma, new flexibilities and microstructures of coatings can be obtained [11]. It is very promising to make nanostructured coatings. Furthermore, advanced columnar structured coatings can also be obtained by SPS. This makes SPS a very promising process to combine the low thermal conductivity of APS TBCs and the excellent durability of EB-PVD TBCs. SPS attracted much more attention in recent years. In this section, mechanisms of these spraying processes and characteristics of that obtained coatings will be given.

2.3.1 Atmospheric Plasma Spraying (APS)

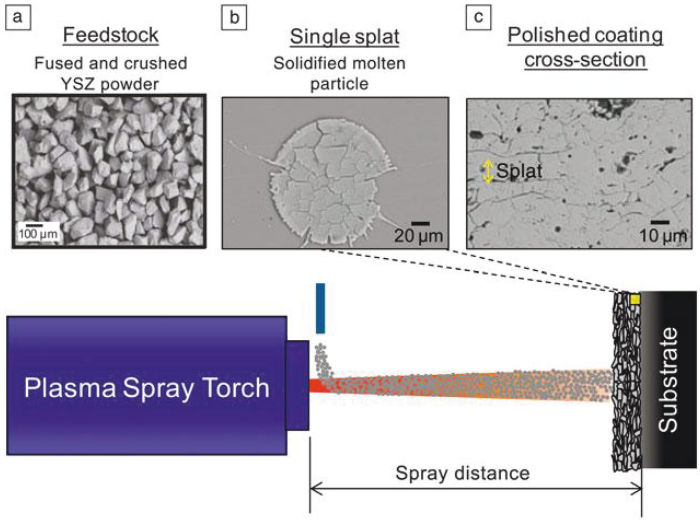

Fig. 2.18 Illustration on APS deposition process and obtained TBCs. SEM images on typical ceramic feedstock powder (a); single splat (b); a polished cross-section of as-sprayed coating (c) [2].

In Fig. 2.18, APS process mechanism is described. Firstly, high speed, high-temperature plasma is generated by a plasma torch. Powdered feedstock (typically ceramics and metals) with particle size ranging from 10 to 100 micrometers is injected into the plasma by gas. The injected particles in

plasma acquire thermal energy and impulse from the thermal plasma. The melted or half melted, high-velocity particles impact on a substrate followed by rapid solidification [116]. The resultant splats have a thickness of a few micrometers and a diameter of 100-150 micrometers. For typical APS conditions, most particles solidify independently. By piling up, a chaotic assemblage of a lamellar structure consisting of splat interfaces, cracks and unfilled regions (pores) can be formed, as shown in Fig 2.18 C.

The thermal plasma can be achieved by four different types of torches: (a) direct current plasma torch, (b) radio frequency inductively coupled plasma torch, (c) wire arc spraying torch, (d) direct current transferred arc plasma torch [117]. Limited by space of this work, only direct current plasma torch which represents more than 99 % plasma torch will be introduced here.

Direct current (DC) plasma torch: a plasma jet can be generated from a continuously flowing gas heated by an electric arc inside a nozzle. The arc is ignited between a cathode and a cylindrical anode nozzle. DC plasma torch can work with Ar, Ar-H_2, Ar-He, Ar-He-H_2, N_2 and N_2-H_2 mixtures resulting in a plasma with a temperature above 8000 K and supersonic velocity ranging from 500 to 2800 m/s. Generally, the plasma forming gases contain a primary heavy gas (Ar or N_2) for the flow and carrying feedstock, a secondary gas to improve the heat transfer (H_2, He).

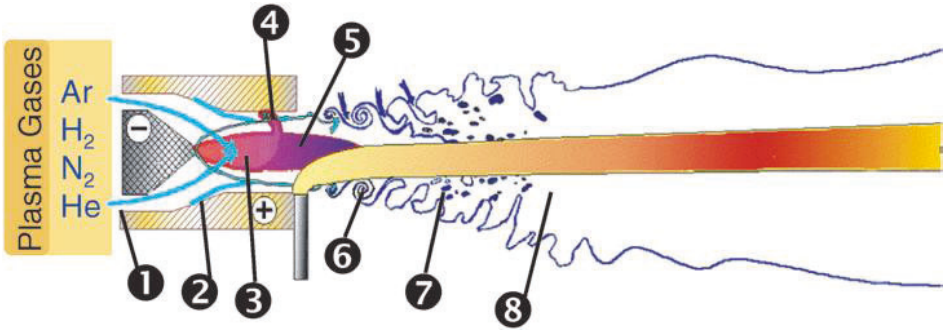

Fig. 2.19 Schematic of a conventional DC plasma torch with: ⊖ stick type thoriated tungsten cathode, ⊕ copper anode, ❶ plasma forming gas, ❷ cold boundary layer at the anode wall, ❸ arc column, ❹ connecting arc column, ❺ plasma jet, ❻ large-scale eddies, ❼ atmosphere bubbles, ❽ plasma plume [118].

A conventional plasma torch with stick type cathode is shown schematically in Fig. 2.19. The cathode is made of thoriated tungsten and the anode is made of high purity oxygen-free copper. An electric arc is ignited between the cathode and the anode. The plasma gas is injected at the base of the cathode, heated by the arc, and exits the nozzle as a high temperature, high-velocity jet. The arc continuously fluctuates in length and position. This is due to the movements introduced by drag force of gas flowing in the cold boundary layer and the magneto-hydrodynamic force. The arc

fluctuations are not favorable for uniformly heating particles, as they can affect the length of plasma core [119].

The particles are injected into the plasma jet either inside of the nozzle or right outside of the nozzle exit. And also the injection direction can be perpendicular to the jet axis or at a positive or negative angle. And then the injected particles are accelerated and melted in the plasma. The coating deposition mechanism of this process is summarized in Fig. 2.20. Within one second about 10^7-10^9 particles are injected into the plasma. Generally, particles in a plasma can be melted or half melted and accelerated to a velocity range of 30–500 m/s. Considering high velocity of particles, their resident time in plasma core and plasma plume are between 0.1 and a few milliseconds. After impaction, splats with thickness several micrometers and diameter ranging from 60 to 200 μm can be formed.

When impact onto the substrate, the molten or semi-molten particles flatten, solidify and form lamellar structured coatings. The flattening is completed within first 5 microseconds upon impaction. Solidification is started during flattening. The complex solidification generally takes place before the next particle impacts at the same position. The splat formation is controlled by many parameters linked to particles and the substrate surface, such as velocity, substrate temperature, particle flight direction and so on. By piling splats, a layer of coating with thickness from several hundred micrometers to several millimeters can be formed. This process can last from several seconds to hours. To ensure a good bonding strength between the coating and the substrate, proper surface treatment of the substrate for getting a certain roughness is necessary. Generally, the surface of substrates needs to be cleaned, grit blasted or roughed with a pressured water jet. The bonding between APS coating and substrate is essentially mechanical due to the shrinkage of the splat upon cooling around a peak of the roughed substrate.

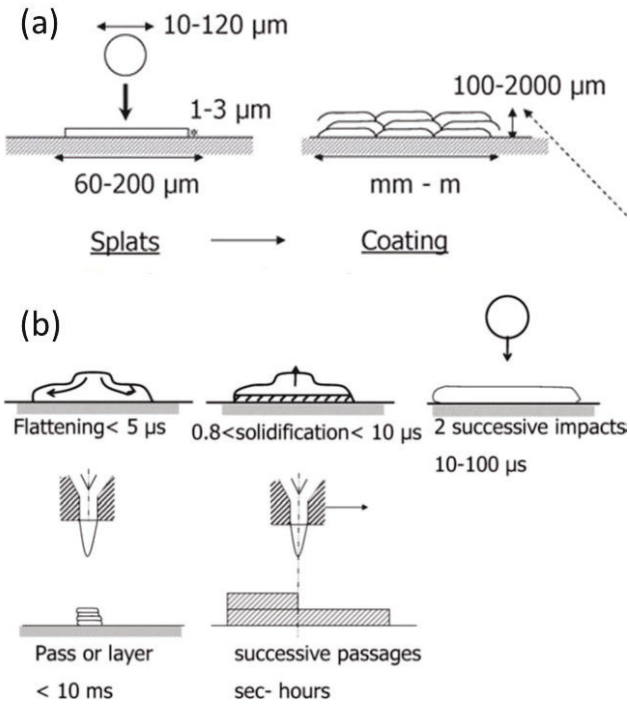

Fig. 2.20 Principle of APS coating formation; (a) showing typical particle and splat size, (b) corresponding time ranges for coating formation [118].

The properties and characteristics of deposited coating strongly depend on the processing. Important parameters include the characteristics of the spray stream (particle trajectory thermal and kinetic state, degrees of melting); location and state of the substrate, including roughness, temperature, position, part geometry, and relative movement. The characteristics of the feedstock powder as well as the state of the spraying device can also play a significant role. For YSZ TBCs, the critical microstructural elements include splats and inter-pass interfaces which are related to the movement of a torch, incompletely filled gaps which can result in varied porosity, intra-splat cracks which can be attributed to releasing of a high level of quenching stresses upon impaction [6].

The compliance and low thermal conductivity of conventional APS TBCs are due to their lamellar and porous structure. Typically, APS coatings show lower thermal conductivity and inferior thermal cycling performance than EB-PVD TBCs. Thus there is a significant interest to incorporate the benefits of EB-PVD into APS TBCs. Vertical cracked ceramic top coats sprayed with plasma spraying

have attracted a lot of interest and been applied in gas turbines [120]. SEM on the microstructure of a typical vertical cracked top coat is presented in Fig. 2.21.

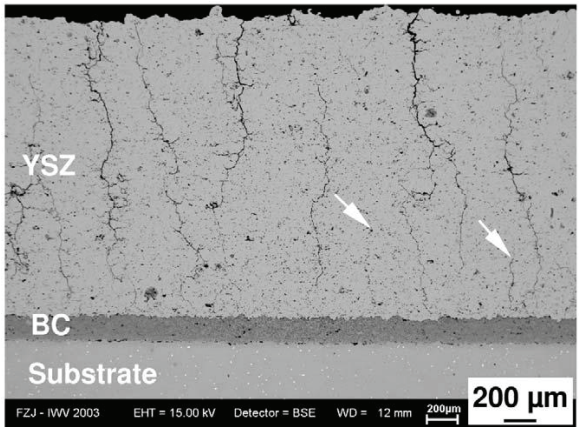

Fig. 2.21 SEM of an as-sprayed cross-section of a vertical cracked TBC [120].

These TBCs have cracks vertically penetrating through the thickness of the top coat. These vertical cracks can provide high strain tolerance to the coating. As reported by Guo et al., a significant improvement in thermal cycling performance has been found on such vertical cracked coatings [120].

Plasma sprayed splats undergo extremely rapid quenching when they impact on the substrate or previously deposited layers. As shown in Fig. 2.18 b, intricate cracks can be formed within a single splat. This is attributed to large lateral tensile stress, as the shrinkage of splat is constrained by the massive substrate. When deposition temperature is raised significantly, a vertical cracked structured coating can be formed. At high deposition temperature, wetting among several splats is improved. They start to behave more or less like a single body. When the tensile stress within the coating exceeds the strength of the coating, macro-scale cracking, as shown in Fig. 2.21, is formed [121].

2.3.2 Electron Beam-Physical Vapor Deposition (EB-PVD)

In Electron Beam-Physical Vapor Deposition (EB-PVD) process, a focused high energy electron beam is directed to evaporate ingot materials in a vacuum chamber, as shown in Fig. 2.22 (a). The evaporated material condenses on the surface of substrates and forms coating [122]. EB-PVD device mainly contains four parts, as shown in Fig. 2.22 (a): 1: electron beam torch which can be directly focused or electro-magnetic deflected as shown in Fig. 2.22 (b) and (c), 2: water-cooled copper crucible, 3: substrates and 4: vacuum chamber.

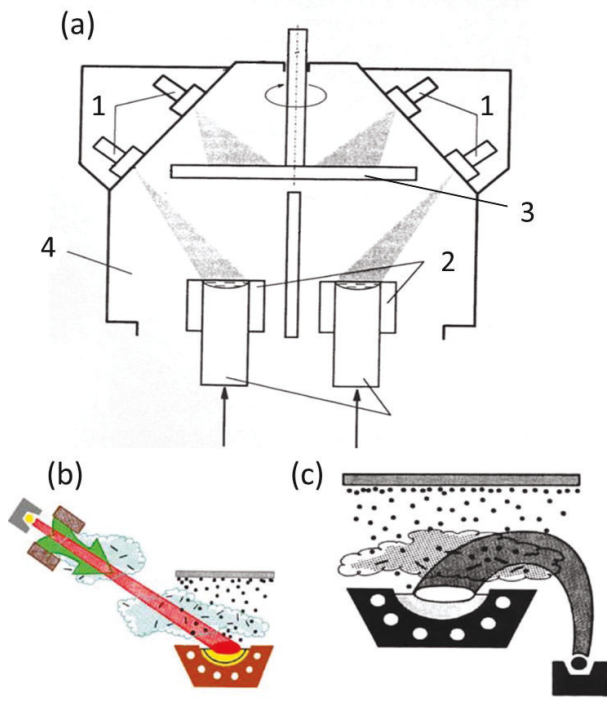

Fig. 2.22 Schematic diagram: (a) EB-PVD facility, (b) straight electron beam gun, (c) electro-magnetic deflected electron beam gun [122].

The EB-PVD process offers extensive flexibility on the composition and microstructure of coatings. Coatings can be graded from metallic to metallic, ceramic to metallic, metallic to ceramic and ceramic to ceramic. Furthermore, alternating layers of different compositions can also be obtained. Before deposition, substrates need to be ion beam sputter cleaned to promote strong adhesion between the coating and substrates.

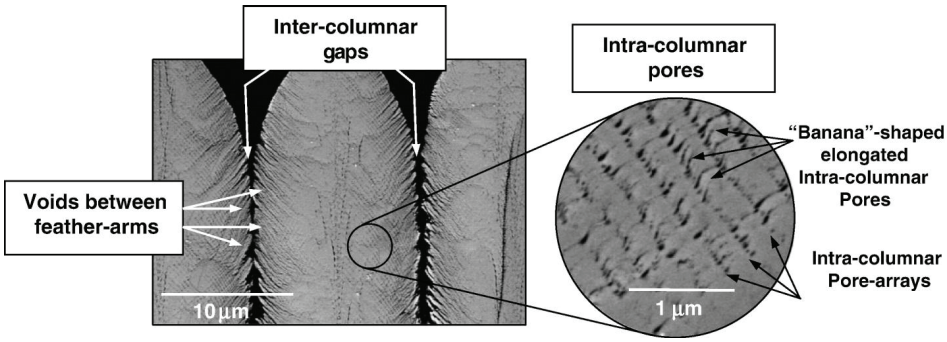

Fig. 2.23 SEM image on the microstructure of EB-PVD TBCs [123].

As the coating is formed from vapor combined with surface diffusion, shadowing and crystallographic growth selection, a columnar structured coating, as shown in Fig. 2.23, can be achieved. Columns with a very small diameter (several micrometers) start to grow on the substrate surface. The diameter can increase up to 10-20 µm at the tip. Columns are separated by inter-column gaps. These gaps are a few nanometers close to the substrate and can be as large as 1 µm at the tip. They can impart high strain tolerance to the coating which is critical for their thermal cycling performance. Open pores in so-called feather-arms can also be found at the column edges. They are formed by secondary shadowing. Furthermore, closed pores due to interruption of deposition can also be formed inside a column [123]. These different types of pores play an important role in determining the thermal conductivity of coatings.

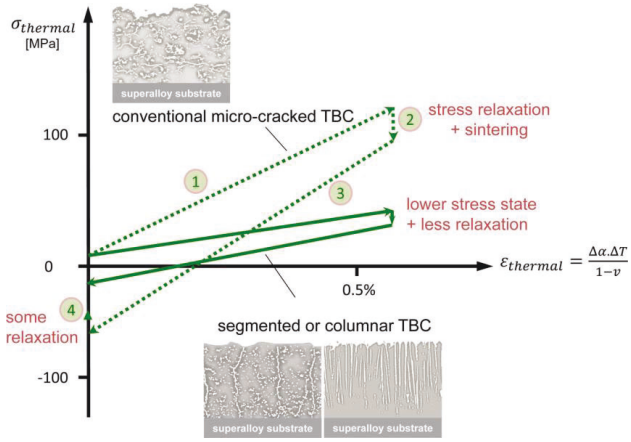

Fig. 2.24 Qualitative stress development within different TBCs deposited on a nickel based superalloy during heating (1) dwell time at temperature (2), cooling (3) and at room temperature (4) [20].

The stress development of conventional APS coatings, vertical cracked coatings (segmented) as well as columnar structured TBCs is illustrated by Bakan et al. [20]. As shown in Fig. 2.24, when the TBCs are heated to high temperature, a tensile stress is developed in ceramic top coat, due to the larger coefficient of thermal expansion of superalloy substrate ①. At high temperature, stress relaxation and sintering of coating take place simultaneously. The former leads to a reduction of thermal stress ②; the latter one leads to a steeper slope during cooling ③. Both of them increase compressive stress at room temperature which might be slightly reduced by room temperature relaxation ④.

In thick TBCs (with a thickness in millimeter range), this thermal stress in coatings becomes more critical. Because driving force for crack propagation is the elastic energy stored in the coating which can be described by the energy release rate (*G*).

$$G = \frac{(1-\nu^2)}{2(1-\nu)^2}\Delta\varepsilon^2 E_{coat} d_{coat} \tag{2.2}$$

where in $\Delta\varepsilon$ is the strain at room temperature which relates to the thermal expansion mismatch between top coat and substrate; E_{coat} is the elastic modulus of coating; d_{coat} is the thickness of the coating; factor ν is the Poisson's ratio. Thus for APS coatings, a further increase of porosity is required to lower E_{coat} and then reduce driving force for crack propagation. For vertical cracked and columnar structured coatings, vertical cracks and column gaps present in top coat significantly reduce the mean stress level in the coating by opening during a heating period as shown in Fig. 2.24. The relaxation in high temperature also becomes limited. Moreover, sintering has less effect on elastic modulus. Thus a smaller thermal stress can be resulted at room temperature leading to better cycling performances.

In summary, the major advantage of EB-PVD TBCs is the columnar structure that provides strain tolerance of coating leading to an excellent performance on thermal cycling. Except for this, EB-PVD coatings also process higher erosion resistance, a smooth surface finish which is benefit to aerodynamic performance. However, the high cost which is contributed by the request on a vacuum, higher thermal conductivity, low utilization of raw materials are the drawbacks [2].

2.3.3 Plasma Spray-Physical Vapor Deposition (PS-PVD)

Plasma Spray-Physical Vapor Deposition (PS-PVD) is a low-pressure plasma spray technology. It allows vaporizing feedstock within the thermal plasma and forming physical vapor deposited coatings on preheated substrates. It is modified on the base of Vacuum Plasma Spraying (VPS) which has been well applied in industry for many years [124]. In comparison to VPS, PS-PVD uses a higher energy plasma torch operated at a reduced vacuum pressure of 0.1 kPa. Due to lower working pressure, the plasma plume is extended to more than 500 mm in length and 40 mm in diameter. The images of plasma jets under different pressure are presented in Fig. 2.25. Combined with a high powerful torch, this makes vaporization of feedstock possible.

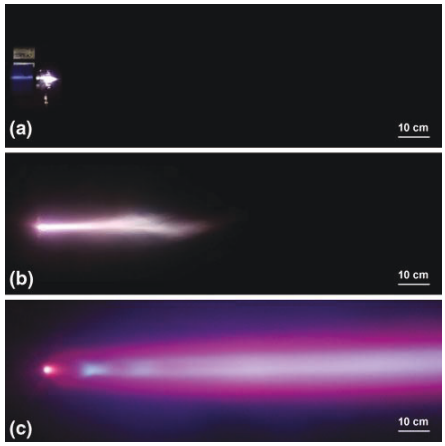

Fig. 2.25 Images of plasma jets expanded at different pressure (a) 95 kPa (APS), (b) 5 kPa (VPS), (c) 0.1 kPa (PS-PVD) [124].

The vaporization degree of powder can be controlled by setting plasma gas composition and powder feeding rate. This enables to develop coatings with different microstructures, as presented in Fig. 2.26 [125]. With a very low vaporization degree, a gas-tight homogeneous coating can be obtained. The coating is formed by pilling splats similar to APS coatings. With a high vaporization degree, a columnar structured coating can be obtained. For this case, PS-PVD exhibits a lot of advantages, such as high deposition rate (100 µm/min) and non-line of sight deposition. With further increasing vaporization degree, a pure vapor deposited coating as shown in Fig. 2.26 can be obtained. However, for this case, the deposition rate is limited.

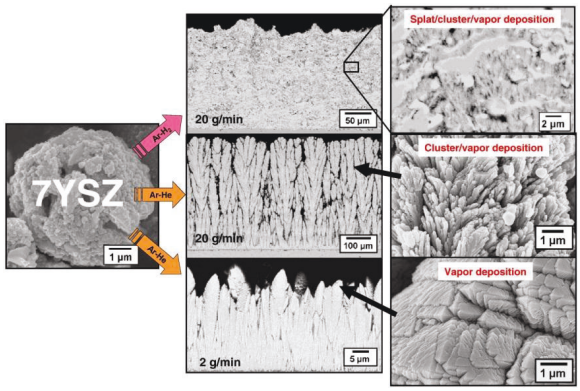

Fig. 2.26 Overview on the microstructures of PS-PVD coatings [125].

Thermal cycling performance of PS-PVD coatings has been investigated by Rezanka et al. [126]. PS-PVD TBCs show excellent thermal cycling performances. High deposition, columnar structured coating together with out of sight deposition make PS-PVD a very promising process for depositing TBCs.

2.3.4 Suspension Plasma Spraying (SPS)

For APS process, the injected powder feedstock has a particle size in the range of 10-100 µm in order to be flowable [2]. This limit on particle size restricts capabilities of APS for processing nano-sized particles. One of the major drawbacks of processing nano-sized particles by APS is the problem of injecting them into the core of plasma plume. Injecting nano-sized particles needs a high cold carrier gas flow rate with which the plasma plume is highly disrupted. To overcome this problem, two technical routes are made: spraying micrometer-sized particles made of nano-sized agglomerated particles or spraying nano-sized particles using a liquid carrier instead of gas [117]. With the liquid, two routes can be implemented. One is using precursor solutions of materials. This process is called Solution Precursor Plasma Spraying (SPPS). The other route is using suspension which is made by dispersing solid particles into a carrier liquid. This process is called Suspension Plasma Spraying (SPS).

The easiest way to produce a suspension is to make a slurry with particles and liquid. The most widely used liquids are ethanol or water or a mixture of both. Nano-sized oxide particles have a tendency to agglomerate. The stability problem can be overcome by using a suitable dispersant agent, which adsorbs on the particle surface and allows an effective dispersion of particles by electrostatic, steric or electro-steric repulsion [127]. Generally, there are two ways to inject the suspension into a plasma, radial injection [127] and axial injection [128]. After injection, suspension undergoes complex interaction with the plasma. The process is described in the following image.

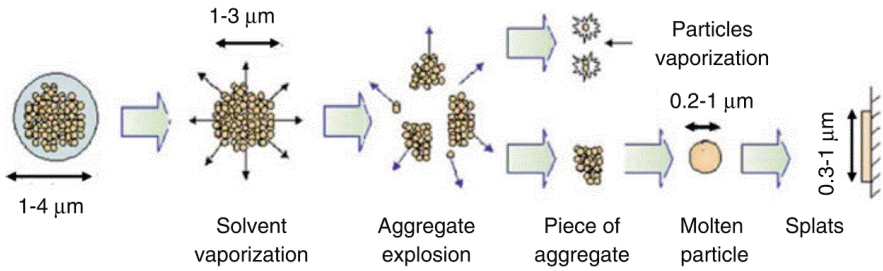

Fig. 2.27 Mechanism proposed for heat treatment of big agglomerates from liquid fragmentation to the splat formation [129].

Atomization, acceleration and vaporization of the liquids simultaneously happen when they are injected into the plasma jet. The injected suspension is atomized into small droplets with size

ranging from 1-4 µm. The liquid is firstly vaporized. The left aggregate particles explode to several parts. Some extremely fine particles are vaporized in plasma. The left large pieces of aggregate are melted into small droplets with a size of 0.2-1 µm. Accelerated by plasma jet, the molten droplets impact on the surface of treated substrates. Splats with size of 0.3-1 µm can be obtained. Similar to APS, by piling up numerous splats, a layer of coating can be formed.

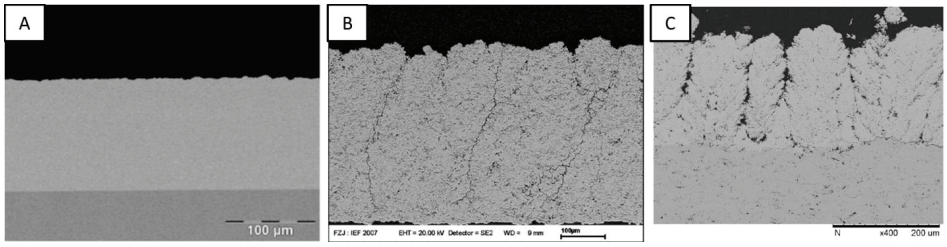

Fig. 2.28 Typical microstructures obtained with SPS; A: homogeneous dense microstructure [130]; B: vertical cracked microstructure [131]; C: columnar microstructure [128].

As the droplet size is much smaller than that of APS, some special microstructures can be obtained by SPS. Typical microstructures of SPS coatings, such as homogenous, vertical cracked and columnar structures are summarized in Fig. 2.28. It seems SPS has a very good flexibility on microstructures. Especially, columnar structure, as introduced previously, seems to be beneficial to the lifetime of TBCs.

The formation mechanism of columnar structures was initially proposed by VanEvery et al. [132]. The formation of columns can be connected to the interaction of atomized droplets with the plasma jet. If the size of the droplets in plasma is smaller than 5 µm, the impact trajectory of the in-flight particles will be severely affected by the plasma gas stream [132].

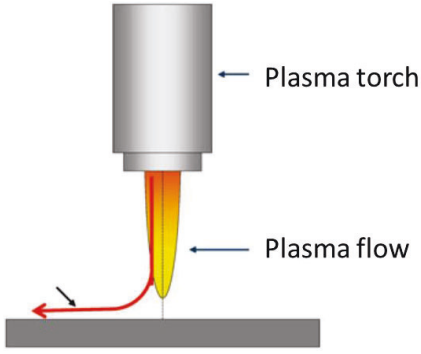

Fig. 2.29 Illustration on the plasma flow trajectory approaching to the substrate [117].

When the high-speed plasma flow approaches the substrate, the flow direction of plasma will be guided parallel to the substrate surface. Due to the different inertia, large particles do not follow the plasma flow, while small particles are easy to follow the plasma flow. The degree of particles following plasma flow can be quantified by Stokes number S_t:

$$S_t = \frac{\rho_p d_p^2 v_p}{\mu_g l_{bl}} \tag{2.3}$$

in which ρ_p is the particle specific mass (kg/m^3); d_p is the particle diameter (m); v_p is the particle velocity (m/s); μ_g is the plasma gas molecular viscosity (Pa • s); l_{bl} is the thickness of the flow boundary layer (m), which varies as the inverse of the square root of the plasma gas velocity. For particles with Stokes number < 1, they cannot penetrate the boundary layer near to the substrate and never impact on the substrate. If the sizes of droplets in the plasma are in the range of 1 to 5 μm or even smaller in diameter, the impact trajectory of in-flight particles will be severely affected by the plasma gas stream[17]. As described by VanEvery et al. [132], if particle size in plasma is small enough, most of the particles are redirected by plasma flow. These small particles impact preferentially on asperities of the substrate. Combined with a shadow effect, a columnar structured coating is formed.

As described in the former part, the columnar structures have an advantage on thermal cycling performance. Researches on columnar structured TBCs deposited with SPS have attracted intensive interest all over the world. The microstructure of SPS coatings is influenced by a variety of parameters. Reported by Curry et al. [133], substrates roughness has a great effect on the microstructure of coating. SPS coating microstructure could be designed by controlling the surface topography on which it is deposited. Investigated by A. Ganvir et al. [134], size of pores, the density of columnar grains and inter-column spacing are greatly affected by spraying conditions. Although coatings with columnar microstructures can be generated over a wide processing window, the inherent microstructure features such as porosity and column density can be vastly different depending on the spraying parameters. Effects of bond coat on microstructures of coating and performances were also reported by Zou et al. [135]. Rough APS bond coat leads to a fan-like structure; while the smooth HVOF bond coat leads to a columnar structure. Effect of parametric variation such as solid loadings, substrate preparation methods and particle size can also play an important role in the formation of columnar microstructures in SPS coatings [136]. It has been reported by Sokolowski et al. [137] that low solid concentration of suspension and long spraying distance promote the formation of columnar structure.

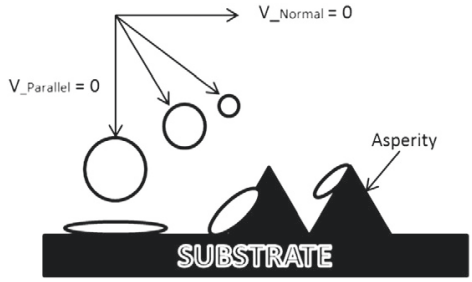

Fig. 2.30 Illustration on the trajectory of particles with different inertia [138].

The thermal conductivity of SPS coating was also reported by many researchers. The thermal conductivity of YSZ coating largely depends on the microstructures. It was reported that thermal conductivity of SPS coatings is in the range of 0.3-1.6 W/mK, while that of APS is in the range of 0.8-1.7 W/mK and EB-PVD coatings are in the range of 1.5-2.0 W/mK [2, 7, 139]. It seems low thermal conductivity coatings can be obtained with SPS. The low thermal conductivity of SPS coatings can be attributed to the existence of numerous micro-pores and micro-cracks in SPS coatings. It is well known that below 1450 K, heat transport is dominated by phonons. Micro-pores which can enhance photons scattering effectively reduce the thermal conductivity of the coating.

Thermal cycling performance is another critical property for TBCs. It has been reported by Curry et al. [128], thermal cycling lifetime of SPS YSZ coating is up to 9903 cycles which is five times longer than that of conventional APS coating. In addition, superior thermal cycling performance was also reported by Bernard et al. [140]. The thermo-cyclic fatigue lifetime of SPS coatings can last for more than 2000 cycles which is much better than that of EB-PVD coatings, as well. However, the factors affecting microstructure and thermal cycling lifetime of SPS TBCs are not fully understood. Getting reliable and longevity SPS TBCs is still challenging. Therefore, this work is aimed to investigate factors influencing microstructure and thermal cycling lifetime of SPS TBCs.

3 Experimental Methods and Materials

3.1 Spraying Facility

In this work, a commercial Axial III torch (Northwest Mettech Corporation, Vancouver, Canada) was used. This torch is composed of three independent cathodes and three anodes powered by three independent power supplies. Essentially, it contains three independent torches. These torches are arranged in a way that their axes are parallel and surround the central suspension injector, as shown in Fig. 3.1. Three plasma jets produced by torches are directed into a common nozzle, the axis of which is aligned with the central injector. These plasma jets converge in a nozzle and form a larger plasma plume. The suspension injected through the central injector is injected at where the plasma jets converge. They are entrained by the high velocity converging plasma jets which can provide a sucking action [141]. Thus, suspension can be injected into the plasma plume more easily. As longer plasma plume is obtained with such three torch design, longer spraying distance can be used. The input power of this torch can be up to 105 kW with a current of 750 A.

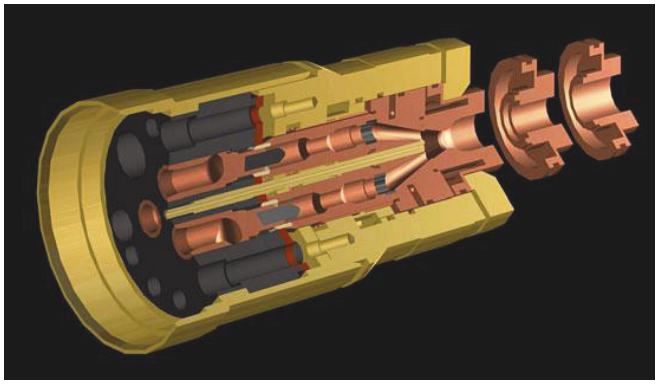

Fig. 3.1 Schematic of Northwest Mettech Axial III central injection torch [117].

The main characteristics of Axial III torch is listed as following [142]:

Plasma gas: Ar, N_2, H_2 (He)

Plasma flow: 100-300 slpm

Input power range: 30-105 kW

Arc current: 300-750 A

Spray distance: 50-250 mm

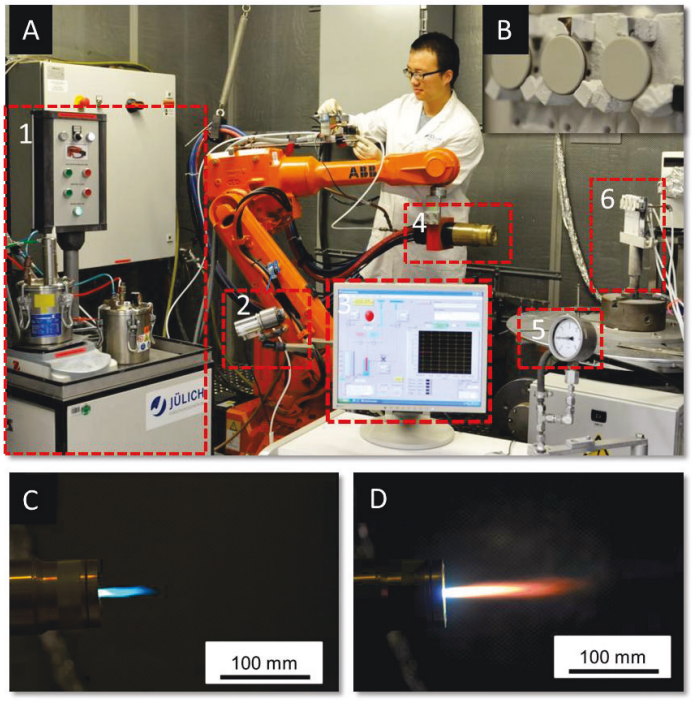

Fig. 3.2 Photographs of the Axial III suspension plasma spraying system; A: set up of spraying facility; B: the image of samples after spraying; C: the image of plasma plume fed with pure ethanol; D: the image of plasma plume fed with an ethanol based YSZ suspension.

Setup of Axial III suspension plasma spraying system is presented in Fig. 3.2 A. It mainly contains 1: feeding system, 2: infrared thermo meter; 3: feeding system controlling unit; 4: Axial III torch; 5: cooling gas pressure meter; 6: sample holder. The feeding system is developed by Forschungszentrum Jülich GmbH (FZJ). The feeding mechanism will be introduced later. With an infrared thermo meter, deposition temperature during spraying can be monitored. The feeding rate of suspension and deposition temperature, the weight of suspension left in the tank can be obtained from the controlling system. The Axial III torch is mounted on a six-axis robot. With pressure meter (5), the pressure of cooling air can be measured. By adjusting cooling gas pressure, different deposition temperature can be maintained on samples. During spraying, samples are mechanically mounted on sample holder (6). The rear side of the sample holders is connected cooling air supply to maintain a certain deposition temperature during spraying. Image of samples which are fixed on the sample holder is presented in Fig. 3.1 B. As shown in Fig. 3.2 C, plasma plume fed with pure

ethanol has a visible length of 50 mm with blue color. When fed with ethanol based YSZ suspension, the color turns to orange and the visible length is expanded to more than 100 mm.

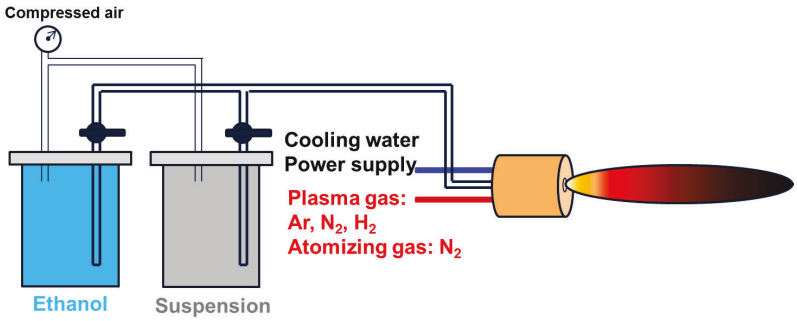

Fig. 3.3 Schematic of feeding system presented in Fig. 3.2.

The schematic of the feeding system is presented in Fig. 3.3. It contains two tanks which are stainless steel pressure vessels with a volume of 1.5 L. One tank is filled with ethanol and the other one is filled with suspension. The ethanol is used for cleaning torch after spraying. Both of them are connected with compressed air supply. Once the valve connected to the tank is open, ethanol or suspension will be pressed into the torch. By changing the pressure of compressed air, the feeding rate of suspension can be controlled. The maximum pressure applied in the tank is 2.5 bars with which, a maximum feeding rate about 32 g/min for YSZ suspension can be obtained. In this work, a mixture of Ar (75 vol%), N_2 (10 vol%) and H_2 (15 vol%) with a flow rate of 245 standard liters per minute (slpm) is used as plasma gas; in addition, N_2 with a flow rate of 15 slpm is used as atomizing gas. Different with pump feeding, the suspension is fed by compressed air; a stable feeding rate can be obtained with this feeding system. However, limited by tank volume, only 1.5 liters of suspension can be sprayed for one time. This makes spraying thick coatings be challenging.

3.2 Raw Powder and Suspension

Table 3.1 General information on raw powders.

Powder name	Material	Internal code	Manufacturer	Particle size (μm)			Chemical composition
				D_{10}	D_{50}	D_{90}	
TZ-3Y	YSZ	YSZ 478T	Tosoh Corporation	35	60	90	ZrO_2 (94.6 wt.%), Y_2O_3 (5.4 wt.%)
TZ-5Y	YSZ	YSZ 435T	Tosoh Corporation	35	60	90	ZrO_2 (90.3 wt.%), Y_2O_3 (9.7 wt.%)
NAMI	YSZ	YSZ 424X	Nanostructured & Amorphous Materials, Inc.	1.4	4.0	7.7	ZrO_2 (91.2 wt.%), Y_2O_3 (8.8 wt.%)
GZO	GZO	GZO 438I	Homemade	0.9	1.1	1.4	Gd_2O_3 (74.6 wt.%), ZrO_2 (25.4 wt.%)

Commercially available YSZ powder from Tosoh Corporation, Tokyo, Japan (TZ-5Y and TZ-3Y) and Nanostructured & Amorphous Materials, Inc., USA (NAMI) were used for preparing the suspensions. In addition, a homemade gadolinium zirconate (GZO) powder was also used for producing suspensions. General information on the raw powders is listed in Table 3.1. Morphologies of raw powders are presented in Fig. 3.4, as well.

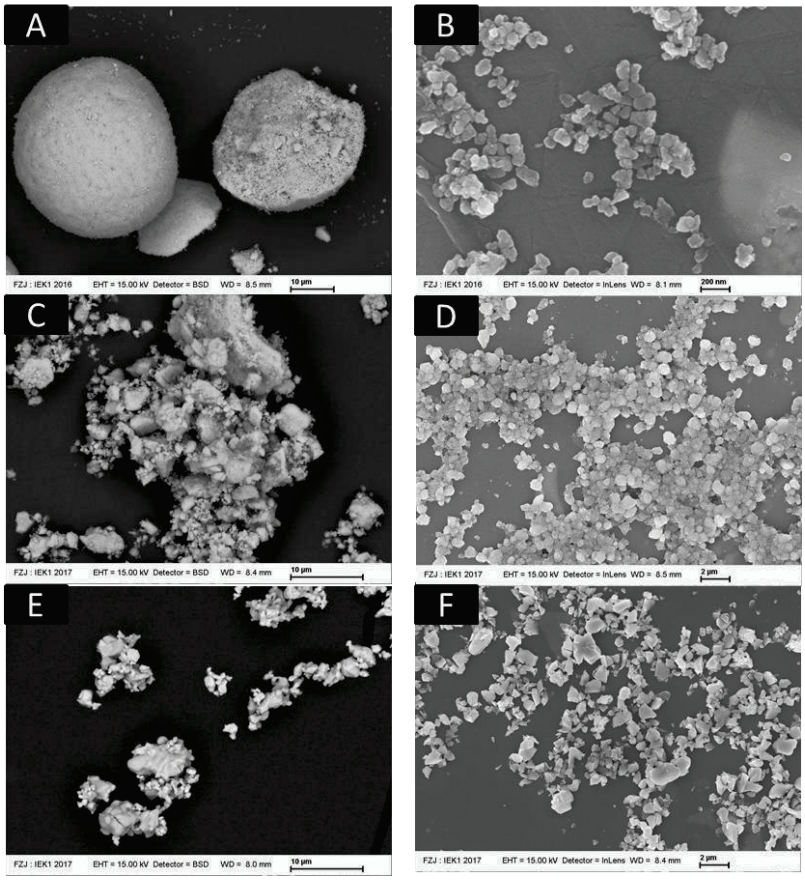

Fig. 3.4 SEM images of raw Tosoh powder (A), milled Tosoh powder (B), raw NAMI powder (C), milled NAMI powder (D), raw GZO powder (E) and milled GZO powder (F).

A homogeneous and stable suspension was made by dispersing raw powder in ethanol with addition of a dispersant agent (PEI, Ploysciences, Warrington, PA, USA) and zirconia milling balls (d = 3 mm, Sigmund lindner GmbH, Warmensteinnach, Germany). The suspension was then kept in a plastic

bottle and milled on roller bank with a rotating speed of 120 r/min for 24 hours. After milling the particle size distribution of powder was measured with a HORIBA LB-550 nanoparticle size analyzer (Retsch Technology GmbH, Haan, Germany). Finally, milling balls were sifted out from the suspension and the left suspension was diluted with ethanol to different solid contents for using. The viscosity of the suspension was measured with a viscosimeter (Physica MCR 301, Anton Paar Germany GmbH, Ostfildern, Germany) at a shear rate of 10 s^{-1}. Particle morphology was also investigated with SEM and the images are presented in Fig. 3.4. Compared with raw powder, the particle size of powder after milling was greatly reduced. The recipe for making suspension is presented in Table 3.2. Basic properties of suspension and particle size of powder after milling are presented in Table 3.3. A 7.5 wt% YSZ suspension (TZ-4Y) was obtained by mechanically mixing TZ-5Y and TZ-3Y powders with a weight ratio of 1:1.

Table 3.2 Recipe for making the suspension.

Ingredient	Amount
Powder	300 g
Dispersant agent (PEI)	4.5 g
Milling ball (ZrO_2)	900 g
Ethanol	700 g

Table 3.3 Characteristics of the suspensions.

Suspension	Chemical composition of solid	Solid content (wt.%)	Viscosity at a shear rate of 10 s^{-1} (mPa·s)	Particle size after milling (μm)		
				D_{10}	D_{50}	D_{90}
TZ-5Y	9.7 wt% YSZ	10	1.63	0.16	0.19	0.27
		5	1.48			
TZ-4Y	7.5 wt% YSZ	5	1.62	0.16	0.19	0.32
NAMI	8.8 wt% YSZ	10	9.63	0.44	0.84	2.60
GZO	$Gd_2Zr_2O_7$	5	1.50	0.33	0.55	1.11

3.3 Characterization Methods

3.3.1 Scanning Electron Microscope (SEM)

In the Scanning Electron Microscope (SEM), an electron beam with an energy ranging from 0.5 to 40 keV is thermionically emitted from an electron gun with a tungsten filament cathode. The electron beam is focused by one or two condenser lenses to a spot about 0.4-5 nm in diameter. Typically, in the final lens, the electron beam is deflected in the x and y axes so that it scans in a raster mode over a rectangular area of a sample surface. When the electron beam interacts with the sample, the electrons lose energy by scattering and absorption with a teardrop-shaped volume which is called interaction volume, as shown in Fig. 3.5. This volume extends from less than 100 nm to around 5 μm

below the surface. The SEM characterization requires high vacuum condition and the specimen must be vacuum compatible and electrically conductive. The charge-up effects of non-conductive samples can be compensated by coating them with a thin layer of metal film (Au, Pt) or carbon layer. SEM has an excellent depth field. For example, at a magnification of 200 ×, the depth field is 100 µm; at a magnification of 10000 ×, the depth field is still 2 µm. This makes an observation on fracture surface be possible. By reacting with samples, electrons (auger electrons, secondary electrons, backscattered electrons) and photons (characteristic X-ray) carrying different informations can be generated.

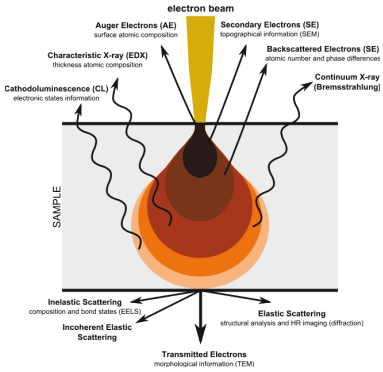

Fig. 3.5 Schematic of signals from a thin sample generated by impinging electrons [142].

Secondary electrons with low energy (<50 eV) generated by inelastic scattering interactions between beam electrons and specimen atoms are the most common collected electrons. With secondary electrons, a high resolution (about 3.5 nm) image can be obtained. As these electrons are sensitive to the orientation of different surface morphologies, secondary electron image has advantages on evaluating sample's surface topography. Generally, in the thermal spraying field, secondary images are often used to observe single splats, surface morphology, metallographic polished surfaces and fracture surfaces of coatings [117].

Backscattered electrons are high energy electrons produced by an elastic collision of the beam electrons with specimen atoms. By collecting these electrons, an image on elemental composition distribution and surface topography can be obtained. Its image resolution (5.5 nm) is lower than that of the secondary electron image, but its brightness is proportional to the atomic number. This makes getting an intuitive elements distribution of sample be possible.

The interaction between beam electrons and specimen atoms results in an emission of characteristic X-rays. The number and energy of the X-rays emitted from the specimen can be measured by an energy-dispersive spectrometer. As the energy of the X-rays is the energy difference between two shells of the emitting element, the elemental composition of the specimen can be measured. This

analytical technique is called Energy-Dispersive X-ray Spectroscopy (EDS). EDS can be used to determine which chemical elements present in a sample and their relative abundance.

In this work, SEM was performed with Zeiss Ultra 55 FEG-SEM (Carl Zeiss microscopy GmbH, Oberkochen, Germany) and Hitachi TM3000 (Hitachi High-technologies Europe GmbH, Krefeld, Germany).

3.3.2 Image Analysis (IA)

Thermal spray coatings, especially APS coatings, have a large amount of defect features such as globular pores, inter-lamellar pores, cracks etc.. Knowledge of these defects is critical since they influence a wide range of coating properties and behaviors in service. Thus characterizing microstructures in reasonable detail is very important.

Many methods are employed to measure the porosity of coatings which is a prevalent feature in the microstructure. Among them, Archimedean Porosimetry, Mercury Intrusion Porosimetry (MIP) and Image Analysis (IA) are the most widely used techniques for measuring the porosity of thermal sprayed coatings. Archimedean Porosimetry is inexpensive and simple in operation. However, its accuracy is relatively lower compared with other methods. MIP is able to detect open porosity with high precision, but it gives a lower porosity compared with other methods as its inability to detect closed pores [143]. Image analysis is able to measure both open and closed pores. Furthermore, it is able to detect pore size distribution and pore morphology. Due to the high contrast between the dark pores and the more highly reflective coating material, porosity of thermal sprayed coatings can be easily detected with IA. The coating porosity is often measured according to the Delesse principle: if the porosity is randomly distributed throughout the coating, then the percentage of the porous area in a coating cross-section is identical to the percentage of porous volume in the entire coating [117]. Both images obtained with optical microscopy or SEM can be used for image analysis. For optical microscopy images, the magnification is generally 500× or below; while for SEM images, magnification values can be up to 1000× or more. Even though high magnification allows detecting detailed features (pores and cracks), the image characteristic dimension should be between 10 and 15 times larger than the objects of interest to be analyzed. Thus statistical measurements (generally 10 to 15 measurements in different locations within coatings) are necessary to ensure a representative result for quantitative analysis. Zhang et al. have proposed a measuring procedure divided into four steps: gray level transformation, fuzzy enhancement of the image, binary segment of image and removing the impurities and identification of pores and micro-cracks. By following these steps, a confidence level of 95 % can be achieved [144].

There still are some limitations on image analysis. The first one is its limited resolution. This makes it difficult to take into consideration features smaller than 0.1 µm. The second one is the results are sensitive to the quality of observed metallographic cross-section. For example, insufficient polishing can result in considerably underestimation of porosity [144].

In this work, all the image analysis work was performed with software AnalySIS (AnalySIS pro, Olympus Soft Imaging Solution GmbH, Hamburg, Germany). To ensure the reliability of the porosity results, 10 images taking from different locations were used for each porosity measurement.

3.3.3 X-ray Diffraction (XRD)

The X-ray diffraction is a versatile, nondestructive technique which is often used to study the atomic and molecular structure of a crystal. When a monochromatic X-ray beam with wavelength λ is projected on a crystalline material with an incident angle θ, diffraction occurs when the travel distance difference of rays reflected from successive crystal planes meats n (integer number) times of wavelength. This law (Bragg's law) is described as following [145]:

$$n\lambda = 2d_{hkl}\sin\theta \tag{3.1}$$

where d_{hkl} is the distance between atomic layers with the same Miller indices (hkl). By varying the incident angle θ, the Bragg's law is satisfied by different *d*-spacing. By plotting the angular position and intensities of the diffracted radiation peaks, a characteristic pattern of a sample can be obtained. If the measured sample contains different phases, the resultant diffractogram is formed by overlaying the individual patterns. Thus the identification of the crystalline phase is based on the comparison of experimental diffractogram with the data pattern of literature (Joint Committee Powder Diffraction Standard). The penetration depth of X-ray beam into the sample can vary from few to several micrometers depending on the sample characteristics and wavelength of the beam. XRD is widely used in thermal spraying field. For example, it can be used to investigate the phase changing in powder, as-sprayed coatings and thermal cycled coatings.

In addition of characterizing phase composition of samples, XRD is also used to estimate the average grain size of sample. An overall broadening of XRD peaks can be observed in XRD diffractograms. This broadening of peaks is due to three effects: instrumental effects, crystallite size and lattice strains. The crystallite effect is that the peaks become broader due to the effect of small crystallite size. Thus an analysis of peak broadening can be used to determine crystallite size. This crystallite effect can be described by the Scherrer equation [146]:

$$\tau = \frac{K\lambda}{D\cos\theta} \tag{3.2}$$

where τ is the broadening of diffraction line measured at Full-Width at Half-Maximum (FWHM), λ is the wavelength of the X-ray radiation; D is the mean dimension of the ordered domains, which may be smaller or equal to the grain size; θ is Bragg angle; *K* is Scherrer constant, the common value of which is 0.9. However, this method is limited to nano-scale grains. It cannot be used for measuring grain size larger than 200 nm. Another point need to pay attention to is it provides a lower bound on the grain size.

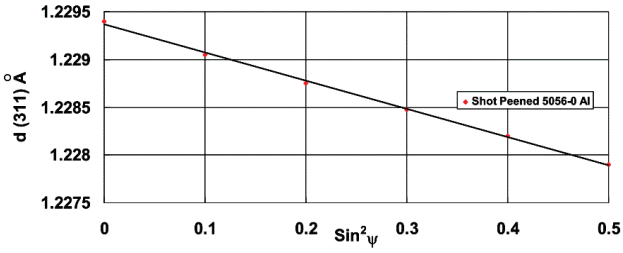

Fig. 3.6 Example of d-spacing versus $\sin^2\Psi$ [147].

X-ray diffraction also makes it possible to measure residual stress which can lead to lattice strain in the sample. By Bragg's Law, there is a clear relationship between the diffraction pattern and the spacing distance between atomic planes as shown in equation (3.1). When the material is strained, elongations and contractions are introduced into the grain. This will cause a change on d-spacing. This change will cause a shift in the diffraction pattern. By precisely measuring this shift, the change in the d-spacing can be measured. According to mathematic relationships between the d-spacing and the strain, strain in the material can be deduced. Finally, by using Hooke's law, residuals stress in a sample can be obtained.

The most commonly used method for stress determination with XRD is the $\sin^2\Psi$ method. A number of XRD measurements are made by tilting sample with an angle of Ψ. By plotting d-spacing as a function of $\sin^2\Psi$ as shown in Fig. 3.6, a curve can be obtained. When there is no shear force in the angled sample, this curve will be a straight line. Then the stress can be calculated with the following equation:

$$\sigma_{residual} = \left(\frac{E_{bulk}}{1+\nu}\right) m \tag{3.3}$$

where $\sigma_{residual}$ is the residual stress; m is the slope of d-spacing vs $\sin^2\Psi$ curve; E_{bulk} is the elastic modulus of the bulk material; ν is the Poisson's ratio. More detailed information can be accessed from ref. [147].

In this work, phases and domain size analysis by XRD were conducted with a D4 Endeavor diffractometer Bruker AXS GmbH, Karlsruhe, Germany) using Cu Kα radiation. The scanning range 2θ was set from 10˚ to 80˚ with a step size of 0.02˚ and a count time of 0.75 s/step. The phase and domain size of measured samples were determined with a Rietveld refinement analysis [148]. Moreover, residual stress in the sample was also investigated with this XRD technique (Empyrean, PANalytical GmbH, Netherlands). The samples were mounted in a five-axis cradle. High angle peak (323) with Bragg angle 2θ = 125.6° was selected for measuring residual stress. The tilt angle Ψ ranged from 0° to ± 56.79°.

3.3.4 Indentation Based Mechanical Properties Tests

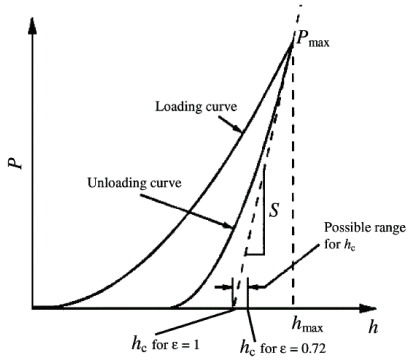

Fig. 3.7 Schematic of a typical indentation load-displacement curve [149].

As illustrated in the introduction part, mechanical properties of TBCs, such as hardness, adhesion, elastic modulus and fracture toughness, are very important for the coating's lifetime under harsh service condition. For thermal sprayed coatings, it is usually very difficult to detach coatings from the substrates. Thus indentation tests on a nano-scale or micro-scale are the most widely used technique to measure mechanical properties of thermal sprayed coatings.

Upon penetration with a load of *P*, an indent can be formed on the measured sample, due to plastic deformation. With specific indenter geometry, the penetration depth depends on the load. During indentation, the load and the penetration depth h are recorded as a function of time. And then a load-displacement relationship can be obtained, as shown in Fig. 3.7.

At first, the load is progressively increased from 0 to the maximum load P_{max} as seen in the loading curve. At the same time, the maximum depth h_{max} is reached. After a certain holding time, the load is reduced to 0, gradually, as seen in the unloading curve. Due to plastic deformation, the unloading curve is different from the loading curve. When the indenter is removed, only elastic deformation can be recovered, leaving a residual deformation. The standard way to estimate the elastic modulus from indentation load-displacement curve is by analyzing the initial unloading slope *S*. The basic idea is that even for materials with plastic deformation, the initial unloading is elastic. The detailed formula derivation was given by Malzbender in ref. [149]. The reduced elastic modulus E_r can be obtained with the following formula:

$$E_r = \frac{\sqrt{\pi}}{2}\frac{S}{\sqrt{A}} \tag{3.4}$$

where *S* is the initial unloading slop, *A* is the projected area of the contact between the indenter and the material at that point. For Vickers indenter, the *A* can be correlated with contact depth h_c as following:

$$A = 24.5{h_c}^2 \tag{3.5}$$

Contact depth h_c can be estimated with the following formula:

$$h_c = h_{max} - \varepsilon \frac{P_{max}}{S} \tag{3.6}$$

where ε is a parameter which relates to the geometry of indenter; P_{max} is maximum applied load; h_{max} is the maximum depth. The parameter ε ranges from 1 for a flat punch to 0.72 for a conical indenter. Commonly, a value of 0.75 is used for Vickers and Berkovich indenters [149]. As the reduced elastic modulus E_r can be easily obtained from the load-displacement curve, the elastic modulus of material can be calculated with the following formula:

$$\frac{1}{E_r} = \frac{1-{\nu_i}^2}{E_i} + \frac{1-\nu^2}{E} \tag{3.7}$$

where $\mathrm{E_i}$ and ν_i are the elastic modulus and the Poisson's ratio of the indenter material, E and ν are the elastic modulus and the Poisson's ratio of indented material.

In this work, all the indentations were performed on metallographic cross-sections of samples. The hardness and elastic modulus of coatings were measured with H-100 Fischerscope (Helmut Fischer GmbH, Sindelfingen, Germany). To get reliable results, the maximum load 1 N was used. After indenting, an effective elastic modulus was automatically given by the indentation facility. The effective elastic modulus E_{eff} is given in the following equation:

$$\frac{1}{E_{eff}} = \frac{1}{E_r} - \frac{1-{\nu_i}^2}{E_i} \tag{3.8}$$

Thus elastic modulus of indented material can be easily obtained with the following formula:

$$E = E_{eff}(1-\nu^2) \tag{3.9}$$

Traditionally, the hardness is measured by making an indentation with a certain load. The harness is defined as the ratio between maximum load P_max and area of indent after removing the load. However, in modern micro or nanoindentation tests, the definition hardness H is different with this traditional one. It is determined by:

$$H = \frac{P_{max}}{A} \tag{3.9}$$

where *A* is the projected area of the contact between the indenter and the material at the initial unloading point. This area is slightly larger than the area of indent after removing the load.

In addition to the hardness and the elastic modulus, the fracture toughness of coatings can also be obtained by indentation tests. This technique is simple and easy to operate. However, indentation fracture toughness results depend on the crack type, equations and constants used for the

calculation. Thus when compare indentation fracture toughness of coatings, it should be done very carefully [150]. The principle for this technique is generating cracks on materials with indentations. The growth of cracks is determined by the elastic and plastic properties of the indented material and also by fracture toughness of the indented material. Thus by analyzing crack features, the fracture toughness of the indented material can be estimated.

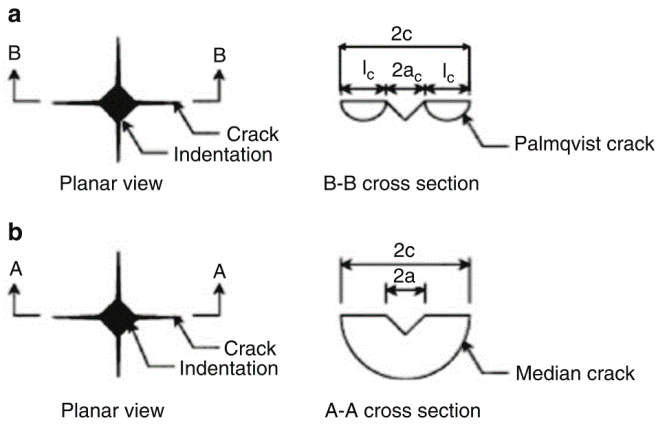

Fig. 3.8 Planar and cross-sectional views of (a) Palmqvist crack and (b) Median crack [117].

As shown in Fig. 3.8, cracks generated by Vickers indenters can be sorted into two groups: Palmqvist cracks and median cracks. The crack mode can be judged by measuring the ratio between crack length *l* and half diagonal length of indent *a* as shown in Fig. 3.8. Generally, for Palmqvist cracks, this ratio lies in the range of $0.25 < \frac{l}{a} < 2.5$; for median cracks, this ratio lays in the range of $\frac{l}{a} > 2.5$. In this work, all the cracks generated are Palmqvist cracks. Thus, the following equation [149, 150] was used for calculating the indentation fracture toughness:

$$K_{IC} = 0.018 \left(\frac{E}{H}\right)^{\frac{2}{5}} H a^{\frac{1}{2}} \left(\frac{a}{l}\right)^{\frac{1}{2}} \tag{3.10}$$

where K_{IC} is the indentation fracture toughness (MPa·m$^{1/2}$), H is the indentation hardness (MPa), E is the elastic modulus (MPa), a is the indentation half-diagonal length (m), and l is the crack length (m). To avoid large deviation and get reliable results, 15 indentations are used for each indentation measurement. And, ν = 0.22 was used for both YSZ and GZO materials [23].

3.3.5 Thermal Cycling Tests

To evaluate thermal cycling performance of coatings under thermal gradient, thermal cycling tests were performed with a burner rig facility. Details on the setup of the burner rig facility were given by Traeger et al. in ref. [151]. During the test, the sample is periodically heated and cooled. Each cycle

contains 5 min of heating phase and 2 min of cooling phase. During the heating phase, the front side of the tested sample is heated by a gas/oxygen burner. Simultaneously, the rear side is cooled with compressed air to maintain a thermal gradient (0.4-1.0 K/µm) across the sample. After the heating phase, the sample is intensively cooled with compressed air from both sides to room temperature within 2 min. The surface temperature of the sample is monitored with an infrared pyrometer. A substrate temperature is also measured with a NiCr/Ni thermo couple which is embedded inside the substrate [152]. In this work, disk-shaped IN738 superalloy substrates were used as substrates. They have a diameter of 30 mm and a thickness of 3 mm. To reduce the stress level and avoid failure at the sharp edge, the outer edge of samples is machined into a curvature with a radius of 1.5 mm. A more detailed description on the thermal cycling samples can be found in ref. [151]. For thermal cycling test, the surface temperature of sample was set to be 1400 ± 30 ˚C, while the substrate temperature was adjusted to be 1050 ± 30 ˚C by adjusting the flow rate of natural gas and cooling gas. To evaluate the thermal cycling performance of TBCs, bond coat temperature T_{BC} (˚C) can be calculated with the following formula:

$$T_{BC} = T_{sub} - \left(\frac{H_{top}}{\frac{H_{sub}}{c_{sub}} + \frac{H_{BC}}{c_{BC}} + \frac{H_{top}}{c_{top}}} \right) \left(T_{top} - T_{sub} \right) \tag{3.12}$$

where T_{sub} (˚C) is the average substrate temperature detected with thermo couple; T_{top} is the average surface temperature (˚C) measured with infrared pyrometer; H_{sub} is the half thickness of substrate (1.5×10^{-3} m); H_{BC} is the thickness of bond coat (2.2×10^{-4} m); H_{top} is the thickness of top coat (m); c_{sub} is the thermal conductivity of substrate (26.0 W/mK); c_{BC} is the thermal conductivity of bond coat (31.0 W/mK); c_{top} is the thermal conductivity of top coat (W/mK). Without of specification, c_{top} is assumed to have a value of 1.0 W/mK [153]. Cycling was stopped when an obvious delamination (with an area larger than 5×5 mm^2) occurred or the thermal gradient through the TBC cannot be maintained. Thermal cycling lifetime of a sample was defined as the number of cycles that the sample survived before its failure. To ensure the reliability of thermal cycling results, two samples were tested for each batch.

3.3.6 Thermal Cycling Tests under CMAS Attack

Table 3.4 Composition of the precursor solution and CMAS [95].

Composition in precursor	Fraction in mol%	Composition of CMAS	Fraction in mol%	Fraction in wt%
Colloidal silica	50	SiO_2	52.8	52.4
$Ca(NO_3)_2{\cdot}4H_2O$	38	CaO	39.4	37.2
$Mg(NO_3)_2{\cdot}6H_2O$	5	MgO	5.2	3.5
$Al(NO3)_3{\cdot}9H_2O$	4	Al_2O_3	2.1	3.6
$NaNO_3$	1	Na_2O_5	0.5	0.5
KNO_3	1	K_2O	0.5	1.4
$Fe(NO_3)_3{\cdot}9H_2O$	1	Fe_2O_3	0.5	1.4

In this work, CMAS tests were carried out with a modified burner rig facility which combines thermal cycling test and CMAS deposition. To simulate the actual service situation in turbine engines under CMAS attack, a water-based CMAS precursor solution was continuously injected into the flame. The composition of the CMAS precursor was designed to mimic the deposits observed on turbine blade. The specific composition of the precursor is given in Table 3.4 [95]. As for the cycling test, each cycle consists of 5 min heating phase and 2 min cooling phase. During the heating phase, samples were heated to a target temperature with the burner. In the cooling phase, both sides of samples were intensively cooled with compressed air to room temperature. The front surface temperature of the tested sample was set to be 1250 ± 30 ˚C which is just above the melting point (1240 ˚C) of most CMAS glassy deposits. And the surface temperature was monitored by an infrared thermo meter. The substrate temperature was measured with a thermo couple which was embedded into the center of the substrate. Same as thermal cycling test, disk-shaped IN738 superalloy substrate with a diameter of 30 mm, a thickness of 3 mm was used as substrates. The 0.1 wt.% CMAS solution was directly injected into the flame through the central axis of the burner nozzle. The feeding rate of the CMAS solution was set to be 1.2 g/min. As a result of the injection method, the distribution of CMAS on the surface of samples is not homogeneous. Due to the deposition of CMAS, it is difficult to scale the spallation area. Thus here a failure of a coating is defined as the thermal gradient through the TBCs cannot be maintained by adjusting gas and cooling air flux. This indicates the coating lost its thermal barrier functionality. Detailed information about cycling CMAS test facility was given by Steinke in ref. [152].

3.3.7 Erosion Tests

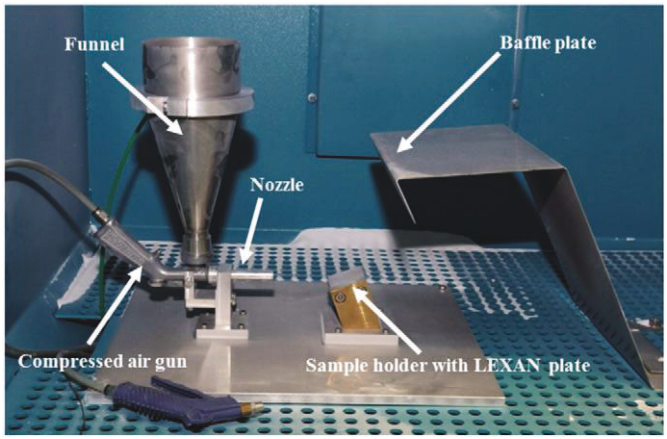

Fig. 3.10 Setup of the erosion test facility [154].

In this work, erosion tests were performed according to ASTM G76-13 at room temperature. The setup of the erosion test facility is presented in Fig. 3.10. It mainly contains a funnel, from where

sand is filled, a nozzle and a sample holder. Sands filled from the funnel are accelerated by compressed air and projected to surface of the tested sample. By measuring the loss of coating thickness, erosion resistance of coatings can be evaluated. The tested sample with a size of 50×50×2 mm^3 was firmly fixed on the holder which has an angle of 20˚ to the axes of the blasting nozzle. And the distance between the nozzle outlet and coating surface was set to be 100 mm. Compressed air with pressure of 0.34 MPa was used. Alumina sands with a grit size of #240 (53 μm in average diameter) were used. Before testing, the surface of the as-sprayed coating was lightly sanded with #60 sandpaper to remove the high spots on the coating surface.

After erosion, erosion resistance of the coatings can be quantitatively evaluated with the following equation:

$$E_{errosion} = \frac{T}{H_{errosion}} \tag{3.14}$$

where $E_{errosion}$ (s/μm) is the erosion resistance of coating, T is the time consumed for erosion (s), $H_{errosion}$ (μm) is the thickness loss on coating after erosion test. A higher $E_{errosion}$ indicates a better erosion resistance of the tested coating.

4 Results and Discussion Part Ⅰ: Relations of Spraying Parameters, Microstructure, Mechanical Properties and Thermal Cycling Lifetime

In this section, effects of spraying parameters such as bond coat roughness, spraying distance, gun power, solid content in suspension and spraying meander on the microstructure of YSZ ceramic top coat were investigated. Based on this work, well developed columnar structured coatings with different porosity level were selected for thermal cycling tests. And then mechanical properties of top coats such as hardness, elastic modulus and fracture toughness of coating were investigated. Finally, a simplified model is built to correlate the mechanical properties and the lifetime of SPS coatings.

4.1 Effect of Spraying Parameters on Microstructures of Coatings

To investigate the effects of spraying parameters on microstructures of coatings, stainless steel plates (25×25×2 mm^3) coated with 200 µm High-Velocity Oxy Fuel (HVOF) bond coat (Amdry 9954, d_{50} = 20 µm) were used as substrates. To make different roughness, the bond coat surfaces were carefully surface-treated with: (1) mirror polishing; (2) grinding; (3) mirror polishing followed by grit blasting; and (4) as-sprayed. Additionally, a rougher HVOF bond coat was also prepared with Amdry 995C (d_{50} = 69 µm) which has a larger particle size than Amdry 9954 [155]. The roughness of bond coats after surface treatment was measured with a non-contact metrology system (CT 350T, Cyber Technologies GmbH, Germany) and the obtained roughness is listed in the Table 4.1. In this work, two kinds of suspension TZ-5Y and TZ-4Y were used. Detailed information of the suspension is listed in section 3.2.

Table 4.1 Surface roughness of bond coats after different surface treatments.

Surface treatment	Roughness (Ra, µm)	Roughness (Rz, µm)
Mirror polishing	0.06	0.27
Grinding	0.26	1.89
Mirror polishing fllowed by grit blasting	2.82	21.6
As-sprayed	10.4	67.4
As-sprayed (coarse)	14.4	87.5

4.1.1 Effect of Bond Coat Roughness on the Microstructure of Coatings

To investigate the effect of bond coat roughness on the microstructure of top coats, a set of top coats were sprayed on bond coats with different roughness at a spraying distance of 70 mm. Detailed spraying parameters are listed in the appendix. To easy description, top coat sprayed on mirror polishing, grinding, grit blasting and as-sprayed bond coat were named as sample A, B, C and D. After spraying, as-sprayed cross-section microstructures of top coats are presented in Fig. 4.1.

Obviously, the microstructures of top coat are greatly affected by the roughness of bond coat. Top coats deposited on relatively smooth surfaces, as shown in Fig. 4.1 (a) sample A and (b) sample B, exhibit a microstructure with vertical cracks penetrating through the entire top coat thickness. It has been reported that vertical cracks in APS TBCs can improve strain tolerance of TBCs during thermal cycling [120]. Therefore, it can be expected that the vertical cracks in the SPS coatings are benefit to the thermal cycling performances of the coatings, as well. The formation of vertical cracks in traditional APS TBCs is related to the cooling and shrinkage of the deposited splats, which results in tensile stress and subsequent cracking during cooling. For SPS coatings, a similar mechanism for the formation of vertical cracks is assumed. Due to the high deposition temperature which can improve wetting between splats, and then the contact between splats was improved. This makes the whole coating work as a single body. This can also lead to high thermal conductivity and high heat flux. When impacted on a relatively cold substrate, the molten splats cool down very quickly. However, the shrinkage of splats is constrained by the massive substrate. Thus tensile stresses are introduced into the coating. When these stresses exceed the strength of the coating, vertical cracks are formed.

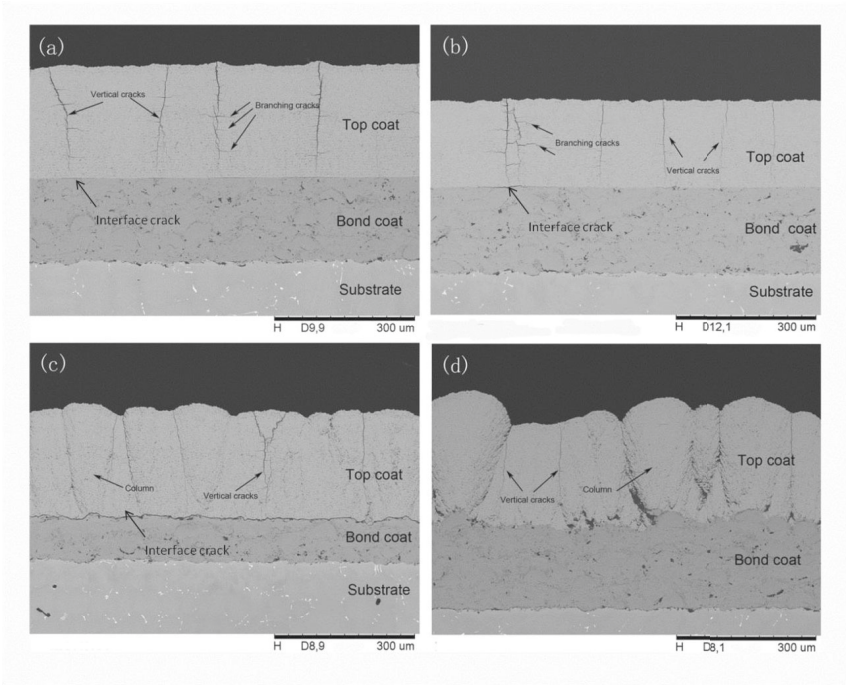

Fig. 4.1 Cross-section SEM image of as-sprayed YSZ top coats (sample A-D) deposited at a spraying distance of 70 mm, on bond coats with different surface treatments: (a) mirror polishing; (b) grinding; (c) mirror polishing followed by grit blasting; and (d) as-sprayed.

As shown in Fig. 4.1 (a) and (b), a large amount of branching cracks which originate from vertical cracks and propagate along porous bands can be observed in top coats. Even though these branching cracks can reduce the thermal conductivity of coatings, they are detrimental to thermal cycling performances of coating [156]. Porous bands existing between successive cracks passes of spraying torch provide an easy pathway for the propagation of such branching cracks under stresses. The formation of porous bands can be attributed to poorly heated, un-molten particles or resolidified particles traveling in jet fringes [157]. The extent of porous bands is largely reduced by axial feeding compared with radial feeding [158]. With axial feeding, a large fraction of the suspension was directly fed into the plasma plume. Thus the number of particles traveling in jet fringes and the amount of un-melted particles was greatly reduced. Additionally, these porous bands can be further reduced by changing the spraying pattern and suspension solid load content.

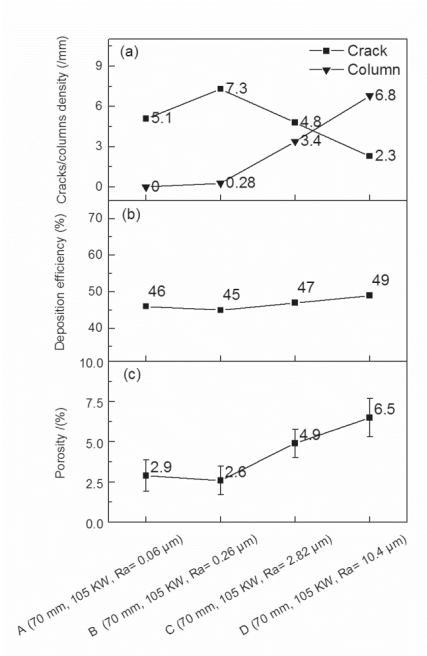

Fig. 4.2 Crack/column density (a), deposition efficiency (b) and porosity (c) for as-sprayed YSZ top coats deposited on bond coats with different surface roughness.

As shown in Fig. 4.1 (c) sample C, columns start to grow on asperities of the bond coat which has a roughness of Ra = 2.82 µm; at the same time, vertical cracks coexist in the top coat. The microstructure of this top coat shows a mixture microstructure with vertical cracks and columns. On as-sprayed bond coat which has a roughness of Ra = 10.4 µm, as shown in Fig. 4.1 (d) sample D, a

typical columnar structure was obtained. All the columns growing on the asperities of the bond coat were separated by porous gaps. This observation is consistent with the proposed column growth mechanism by VanEvery et al. [132]. When particles approach to the substrate, the plasma drag force changes the particle's trajectory from normal to along substrate surface. These particles preferentially impact on asperities of bond coat. With a shadow effect, columns grow on asperities. The porous column gaps are expected to increase strain tolerance of coatings leading to a better thermal cycling performance.

Vertical crack density and column densities as important features of coatings are presented in Fig. 4.2. Column and vertical crack density of coatings were counted from cross-section SEM images (300 ×) of top coat. A straight line parallel to the substrate was drawn at half thickness of the coating. Vertical cracks and columns intercepting this line were counted. The counted area had a length of 7 mm. The Vertical crack density decreased from sample B to D, while the column density showed an opposite tendency. It seems vertical cracks compete with columns and so the cracks density has an obvious correlation with column density. Probably, opening of columns can release tensile stress within the top coat, which is a prerequisite condition for generating vertical cracks. One point should be mentioned here is that during deposition of sample A, a small part of top coat peeled off from the substrate due to the poor bonding with the bond coat. The tensile stress accumulated in top coats was probably partially released leading to the unexpected low crack density of sample A. At the interface of sample A, B and C, cracks can be clearly observed. This indicates low bonding strength between the top coat and the bond coat.

Deposition efficiency of top coats was calculated by dividing the weight difference of samples before and after spraying with the weight of YSZ powder used during spraying. The deposition efficiency η can be obtained with the following equation:

$$\eta = \frac{G_c}{G_s} \times 100\% \tag{4.1}$$

in which, G_c (g) is the weight of top coats deposited on the substrate, G_s (g) is the weight of YSZ powder used for forming coatings. The deposition efficiency of samples A, B, C and D is roughly constant (45-49 %). It seems bond coat roughness barely affects the deposition efficiency.

The porosity of the top coats was also investigated with image analysis as shown in Fig. 4.2 (c). Porosity can be easily detected due to the high degree of contrast between the dark pores and the high brightness coating material [159]. The image analysis results show sample A and B have very low porosity level only about 2.9% and 2.6%, respectively. The porosity level of top coats increased with the increase of bond coat roughness (from sample B to D). Probably, columns can introduce additional porosity, specifically column gaps, into the top coats. In summary, bond coat roughness can affect the porosity of top coats by affecting the microstructure of top coats. Due to the limited resolution of images, very fine porosity of top coat in nanometer range is not accessible. The porosity of top coat might be underestimated.

4.1.2 Effect of Spraying Distance on Microstructures of Coatings

To investigate the effect of spraying distance on microstructures of coatings, a set of top coats was deposited on bond coats with different roughness at a longer spraying distance (100 mm). They are named as E, F, G, H and I. They were deposited on a mirror polished, grinded, grit blasted, as-sprayed and as-sprayed coarse bond coat, respectively. Cross-sectional microstructures of the top coats are presented in Fig. 4.3. All the top coats showed a columnar microstructure. In addition, columnar structured top coats can even be obtained on a smooth surface as shown in Fig. 4.3 (a) and (b). It seems increasing spraying distance promote the growth of columns. This can be explained by considering the Stokes number S_t, as shown in equation (2.3).

At a longer spraying distance, particles and plasma gas have lower velocity. This leads to a thicker boundary layer and hence a reduction of particle Stokes number. Particles with lower Stokes number are more easily to follow the plasma gas and deposit preferentially on asperities of bond coat surface forming columns. In other words, increasing spraying distance promotes formation of columns. The columns formed on smooth surface, as shown in Fig. 4.3 (a) sample E and (b) sample F, do not directly grow on surface of bond coat, but has a certain distance away from the bond coat surface. This indicates that previously deposited ceramic top coat surface can provide asperities for column growth. These asperities should have a proper size which is related to the spraying conditions and is able to trigger the growth of columns. Cracks were also observed at interface for sample E, F and G which were deposited on mirror polished, grinded and grinded followed by sandblasting surfaces. It seems bonding strength between top coats and bond coat is very weak. This implies the bonding mechanism between top coat and bond coat is mainly mechanical bonding. Mechanical interlocking between splats and asperities of bond coat provides the bonding strength.

Column density, deposition efficiency, as well as porosity are presented in Fig. 4.4. It seems column density drops gradually with the increase of the bond coat roughness. This observation can also be explained with the deposition mechanism proposed by VanEvery et al. [132]. Increasing roughness of bond coat reduces the number of asperities which promote the growth of column in a specific area.

Deposition efficiency of the top coat is only about 21-22%. It is significantly reduced compared with that of top coats deposited at 70 mm spraying distance, as shown in Fig. 4.2 (b). A longer spraying distance increases the number of particles with Stokes number below 1. These particles follow plasma gas when approach to substrate and might never impact on it. Furthermore, longer spraying distance can lead to cooling down of particles and reduced substrate temperature. Both factors might lead to lower sticking probability of particles.

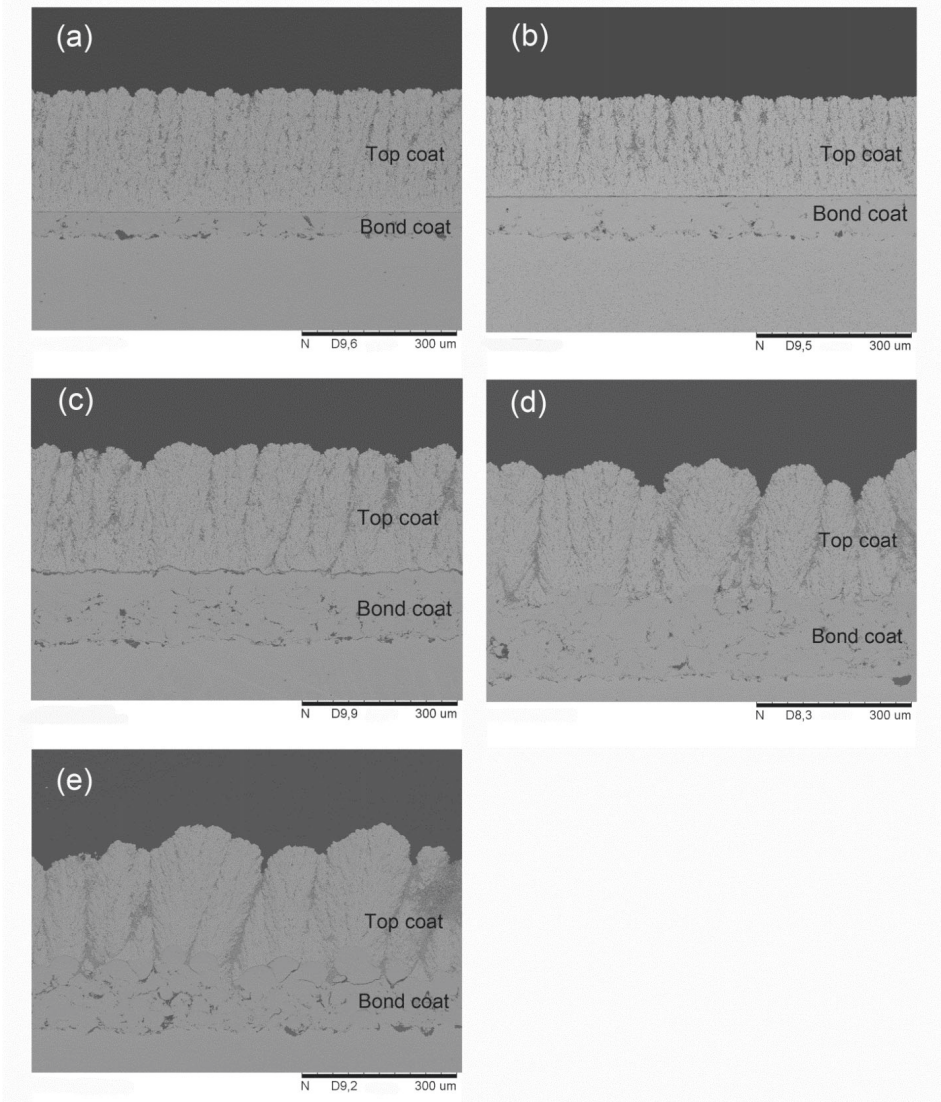

Fig. 4.3 Cross-section SEM images of as-sprayed YSZ top coats (sample E-I) deposited at spraying distance of 100 mm, on bond coats with different surface treatments: (a) mirror polishing; (b) grinding; (c) mirror polishing followed by grit blasting; (d) as-sprayed; (e) as-sprayed (coarse).

The porosity of top coats measured with image analysis is presented in Fig. 4.4 (c). All the top coats have higher porosity compared with the top coats deposited at 70 mm spraying distance. This probably relates to reduced droplet temperature and velocity impacting on substrates. With an increase of bond coat roughness, from $R_a = 0.06$ µm to $R_a = 2.82$ µm, the porosity of top coat increases gradually and only a slight increase can be observed from sample G to I. It seems porosity of top coat is not sensitive to high roughness bond coat when the roughness of bond coat is higher than 2.82 µm.

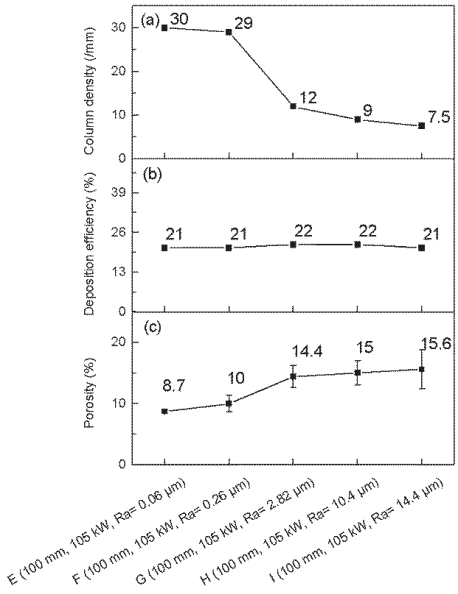

Fig. 4.4 Columns density (a), deposition efficiency (b) and porosity (c) for as-sprayed YSZ top coats (sample E-I) deposited at spraying distance of 100 mm on bond coats with different roughness.

4.1.3 Effect of Gun Power on Microstructures of Coatings

By reducing the input power from 105 kW to 84 kW, as shown in the Appendix, top coat (sample J) was deposited on an as-sprayed HVOF bond coat. The microstructure of sample J is presented in Fig. 4.5. The top coat was columnar microstructure. Column density was about 8.8 /mm which is higher than the value of sample D, as shown in Fig. 4.2 (a). Moreover, it had a higher porosity of about 18.5%. It seems reducing input power can promote the growth of column and increase the porosity of top coats. This is because, with reducing gun power, particle velocity, temperature and flattening were also reduced when impacting on the substrate. This led to poor contact between splats

resulting in higher porosity. Deposition efficiency of top coat was about 48 % which is similar to that of sample D. It seems slightly reducing input power barely affect the deposition efficiency.

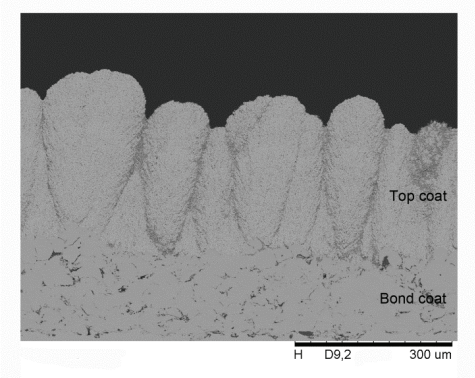

Fig. 4.5 Cross-section microstructure of as-sprayed YSZ top coat (sample J) deposited at 70 mm spraying distance with 84 kW input power on an as-sprayed bond coat.

4.1.4 Effect of Solid Content on Microstructures of Coatings

By reducing solid content in suspension from 10 wt.% to 5 wt.%, sample K and L were deposited on as-sprayed HVOF bond coat with spraying distance 70 mm and 100 mm, respectively. The detailed spraying parameter is shown in the Appendix. Cross-section microstructure of as-sprayed top coats is presented in Fig. 4.6. Both top coats were well developed columnar structured coatings. No vertical cracks could be found from the cross-section. Column density for sample K and L was 10.4 and 11.0 /mm, respectively. Furthermore, the porosity of top coats was 19.3% and 28.0 %. Compared with sample D (Fig. 4.2) and sample H (Fig. 4.4), it seems lowing solid content in suspension from 10 wt.% to 5 wt.% can promote column growth and increase porosity of the coating. In addition, deposition efficiency of sample K and L was 60.7 % and 27.2 %, which is surprisingly improved compared with samples sprayed at same spraying distance. Due to different injection method, axial SPS is able to reach higher deposition efficiency than radial SPS. The deposition efficiency of sample K could reach the same level as APS, which can be 60% and even above [160]. It is supposed that by further shortening spraying distance, deposition efficiency can be further increased.

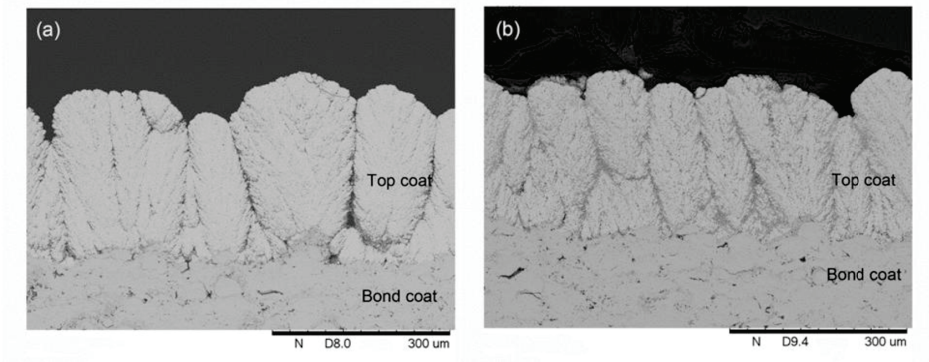

Fig. 4.6 Cross-section images of as-sprayed YSZ top coat (sample K (a) and L (b)) deposited with 5 wt.% solid content suspension on as-sprayed bond coats.

4.2 Relations of Mechanical Properties and Thermal Cycling Lifetime of Coatings

4.2.1 Microstructure and Thermal Cycling Performance of Coatings

Based on the investigation on the relationship between spraying conditions and microstructures, two well-developed columnar structured top coats (sample M and N) were deposited on IN738 substrate with a layer of VPS bond coat (Amdry 9954). After spraying, these samples were subjected to thermal cycling tests. As-sprayed microstructures of sample M and N are presented in Fig. 4.7. Column density of sample M and N was 10.1 /mm and 12.7 /mm, respectively. The porosity of top coats measured with image analysis for sample M and N was up to 22.8% and 29.1%. With high-resolution images, a large number of micropores and microcracks with size several micrometers could be clearly seen within columns. Sample N with higher column density and porosity are expected to have a higher strain tolerance and a better thermal cycling performance. Thermal cycling testing conditions and lifetime are presented in Table 4.2. It turned out that the average thermal cycling lifetime for sample M and N were 177 and 76 cycles, respectively. Photographs and cross-section microstructure of thermal cycled samples are presented in Fig. 4.8. It can be seen from photographs that a bit of white YSZ residue attached on the substrate at the delaminated area. This indicates that the delamination happened within the ceramic top coat.

Furthermore, both samples had a very thin layer of TGO with a thickness of about 2-3 µm. Compared with typical TGO thickness of APS coatings at failure (6-12 µm), TGO here observed in sample M and N was very thin and far from reaching to the critical thickness [161]. This observation indicates that the growth of TGO is not the major reason for the premature failure of the top coat with respect to APS coating.

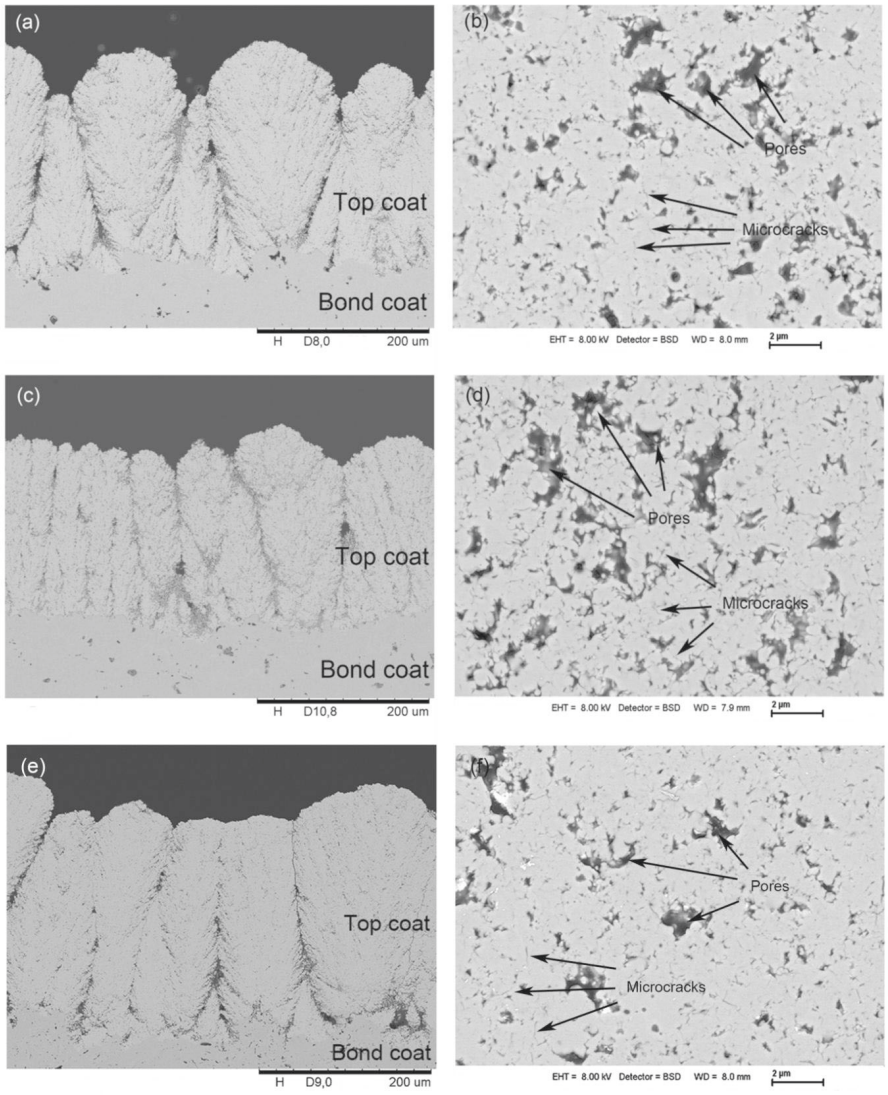

Fig. 4.7 Cross-section microstructure of as-sprayed YSZ top coats (a) sample M, (c) sample N, (e) sample O; and detailed microstructure within columns: (b) sample M, (d) sample N, and (f) sample O.

Table 4.2 Overview on the thermal cycled sample M, N, O and P.

Sample	WDS No.	Thickness (µm)	Bond coat/top coat interface temperature (˚C)	Top coat surface temperature (˚C)	Top coat temperature gradient (˚C/µm)	Lifetime (cycles)
M	1	~255	1119	1346	1.10	193
	2	~257	1098	1284	0.78	160
N	1	~257	1118	1384	1.10	81
	2	~245	1121	1362	1.14	71
O	1	~289	1094	1277	0.63	218
	2	~317	1089	1283	0.61	269
P	1	~428	1087	1355	0.63	166
	2	~408	1085	1344	0.64	136

It was reported by Vassen in ref. [27], YSZ shows an insufficient phase stability at temperature above 1200 ˚C. The metastable t' phase, which is formed due to rapid cooling during deposition process, undergoes phase transformation into equilibrium tetragonal and cubic phase at temperature above 1200 ˚C. Upon cooling, the tetragonal phase transforms into monoclinic phase accompanying a large volume change (4 vol%). This volume change which can introduce additional stress into the coating is detrimental to thermal cycling lifetimes. Thus XRD analysis was performed on thermal cycled samples to investigate the phase evolution of the coating during the thermal cycling. X-ray diffractograms of as-sprayed and thermal cycled samples are presented in Fig. 4.9. All the peaks distinguished from as-sprayed sample XRD patterns can be attributed to the tetragonal phase. According to lattice parameter results, the ratio $^{c}/_{a\sqrt{2}}$ for tetragonal phase falls into the range of 1.010 to 1.000. This indicates that the tetragonal phase found in as-sprayed samples is non-transformable [67, 148]. After cycling, no monoclinic phase was detected in the XRD patterns. And also non-transformable tetragonal phase was detected from both thermal cycled sample M and N; in addition, a cubic phase was detected from thermal cycled samples. According to quantitative analysis, around 12 wt% cubic phase was found in both thermal cycled samples. The cubic phase which has low fracture toughness is detrimental to the thermal cycling lifetime of coatings, as well. The reason for the relatively large amount of cubic phase in thermal cycled samples probably is the fairly high yttria content in coating which is up to 9.7 wt%.

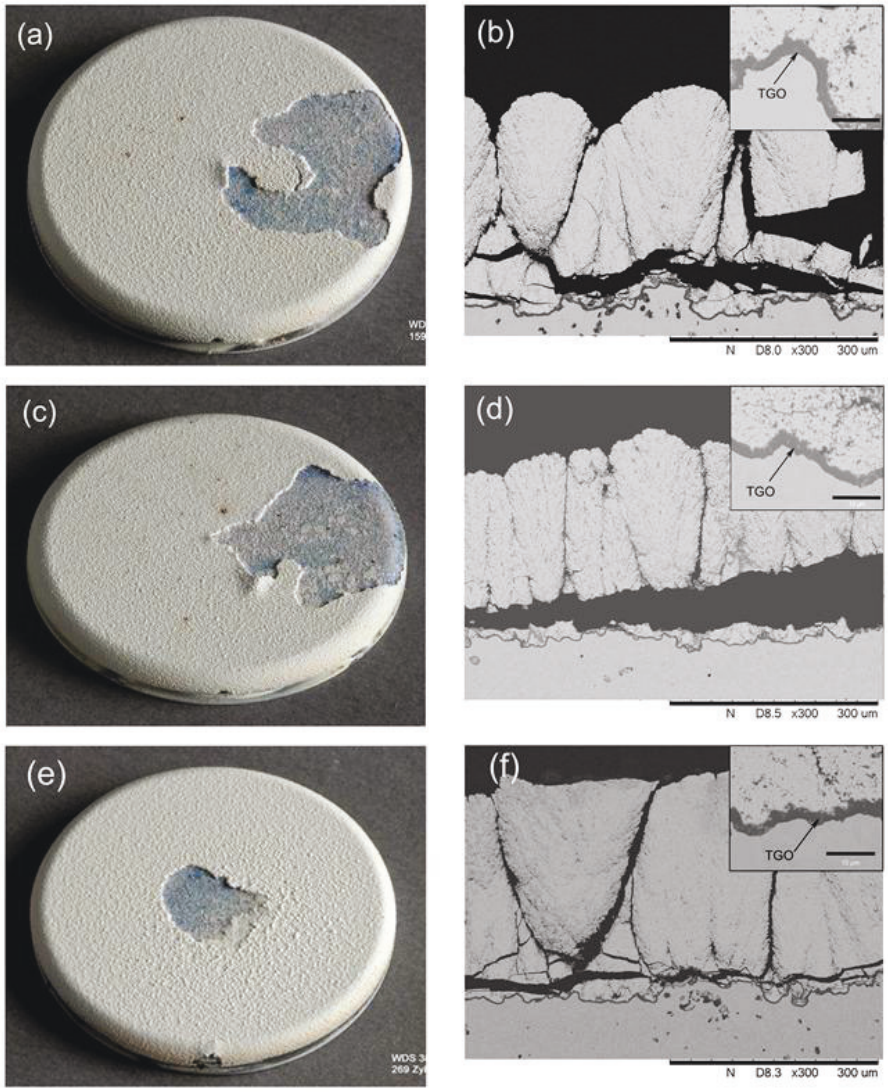

Fig. 4.8 Photographs of thermal cycled samples: (a) sample M, (c) sample N and (e) sample O; cross-section SEM images of thermal cycled samples: (b) sample M, (d) sample N and (f) sample O.

In order to exclude the effect of high Yttria content on thermal cycling lifetime of coatings, sample O was deposited with 7.5 wt% YSZ powder which was made by physically mixing TZ-3Y with TZ-5Y powder. The as-sprayed microstructure of sample O is presented in Fig. 4.7 (e) and (f). As a result of using the same spraying parameters, sample O with a porosity of 17.6%, exhibited similar columnar structure as sample M. and the column density of sample O was 10.1 /mm which is same with sample M. After spraying, sample O was subjected to thermal cycling test. The average thermal cycling lifetime for sample O was about 244 cycles, as shown in Table 4.2. Compared with sample M, thermal cycling lifetime of sample O was improved, but this lifetime was still short when compared with APS coatings [161]. Photograph and cross-section SEM image on the thermal cycled sample O is presented in Fig. 4.8. It seems failure mode of sample O was similar to that of sample M and N. Delamination occurred within top coats and was near to the bond coat interface. XRD diagrams on sample O are also presented in Fig. 4.9. From as-sprayed sample O, only non-transformable t' phase can be found. In thermal cycled sample O, both non-transformable t' phase and cubic phase can be found. However, the amount of cubic phase decreased to about 7 wt%. It seems by reducing Yttria content in coatings, cubic phase amount was successively reduced. Having in mind that the lifetime was still relatively low, it can be concluded that relatively high yttria content and phase transformation of YSZ were not the main reasons for the premature failure of these SPS coatings.

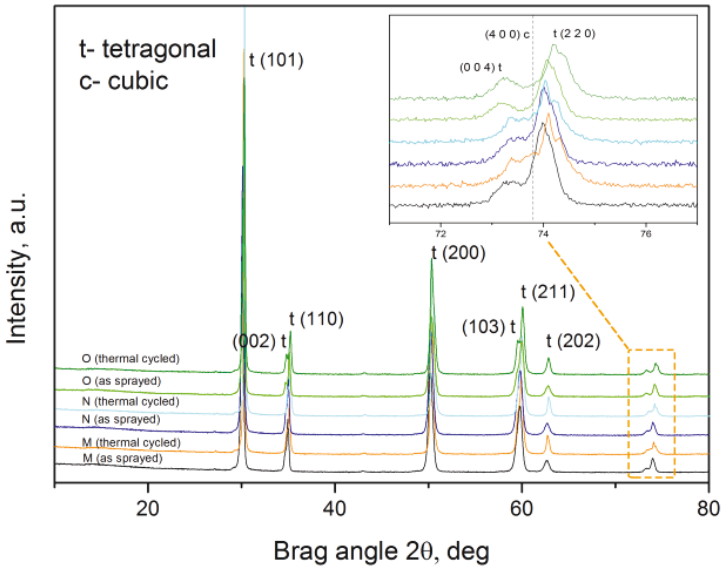

Fig. 4.9 X-ray diffractograms of as-sprayed and thermal cycled YSZ samples.

Another possible explanation for the premature failure of SPS top coats with respect of APS top coat might be related to the mechanical properties of top coats, such as elastic modulus, fracture toughness. Hence, the mechanical properties of top coats were investigated with indentation tests. This part of the results will be discussed in the next section.

4.2.2 Relations between Mechanical Properties and Thermal Cycling Lifetime

Mechanical properties of top coats, such as hardness, elastic modulus and fracture toughness, were measured with indentation tests. Especially, the fracture toughness of as-sprayed top coats and thermal cycling lifetime are presented in Fig. 4.10. Fracture toughness of sample M, N and O were lower than the value of typical APS coatings, which is about 2.0-3.3 MPa·m$^{1/2}$ [162]. Furthermore, it seems that thermal cycling lifetime was related to fracture toughness of these three samples. This indicates low fracture toughness of these top coats might be the reason for premature failure of SPS coatings. Probably, by further increasing fracture toughness of the top coat, the lifetime of TBCs could be further improved.

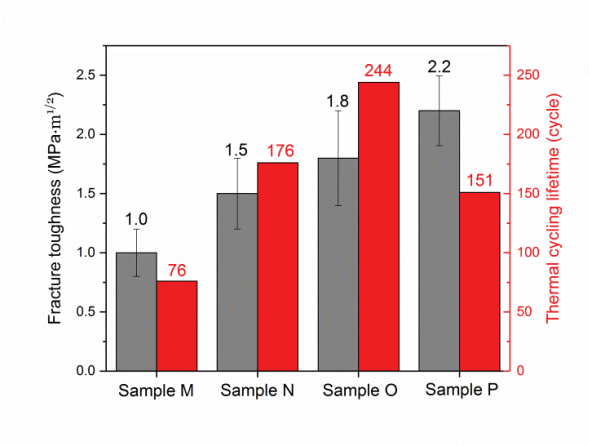

Fig. 4.10 Fracture toughness (left column) and thermal cycling lifetime (right column) of sample M, N, O and P.

Here comes the question, how can improve the fracture toughness of coatings. As reported by Guazzato [163], porosity in the ceramic material generally has a negative correlation with fracture toughness. This is consistent with the observation on samples from M to O. Sample O had the lowest porosity, while it exhibited the highest fracture toughness. Thus we tried to further decrease the porosity of coating by increasing deposition temperature. There are several ways to achieve this target. One is decreasing spraying distance. But this will greatly change microstructure of the coating such as column density. Therefore, the other way, increasing deposition temperature by keeping a plasma plume on substrate for a longer time was used.

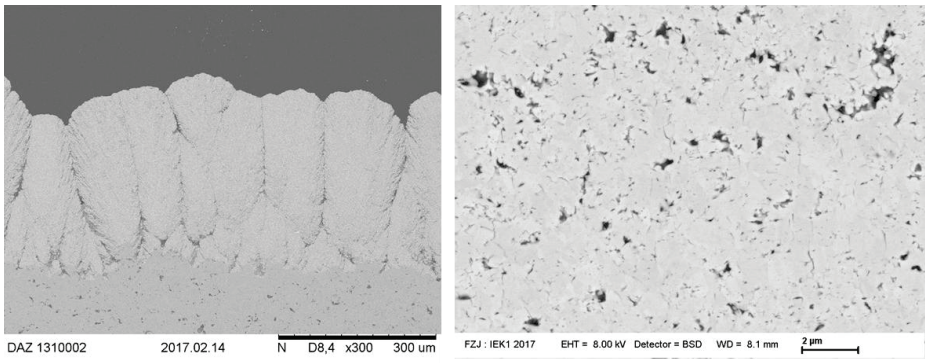

Fig. 4.11 Cross-section microstructure of as-sprayed sample P (a) and detailed microstructure within column (b).

A shorter meander (200 mm instead of 320 mm, as seen in the Appendix) was used to deposit sample P. As a result of the reduced meander, deposition temperature was increased from the range of 280-370 ˚C to 400-550 ˚C. Microstructure of as-sprayed sample P is presented in Fig. 4.11. Sample P exhibited also a well-developed columnar structure. Within columns, a large amount of micropores and microcracks with micrometer size or even submicron-meter size could be found. Deposition efficiency, column density and porosity within the column which is more related to indentation fracture toughness of coating are investigated and are presented in Fig. 4.12. The porosity here was obtained with image analysis. For the porosity within the columns and exclude columns gaps, all SEM images used were taken from the center of columns with a magnification of 3000 ×. It seems deposition temperature barely affect deposition efficiency and column density of the coating. Sample P had a deposition efficiency of 56.7% and a column density of 9.7 /mm. Both were similar to those of sample O. However, deposition temperature had a significant effect on porosity within the column. By increasing deposition temperature, porosity within column decreased from 6.7% (sample O) to 4.8% (sample P). It seems porosity within column was successively decreased. Fracture toughness of sample P is also presented in Fig. 4.10. Sample P had a fracture toughness of 2.2 MPa·$m^{1/2}$. So the fracture toughness of the coating was also successively increased by increasing deposition temperature.

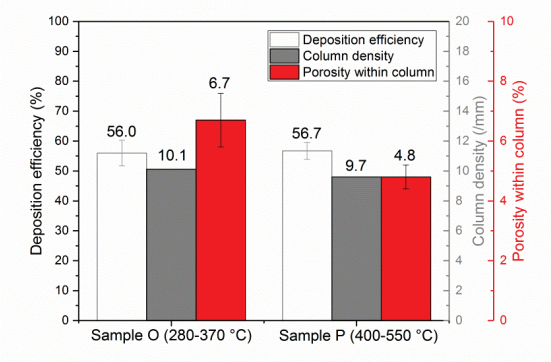

Fig. 4.12 Effect of deposition temperature on deposition efficiency, column density and porosity within columns.

After spraying, sample P was subjected to a thermal cycling test. Testing conditions and lifetime are summarized in Table 4.2. Even though with a high fracture toughness, sample P exhibited a large reduction on lifetime. It had an average lifetime of about 155 cycles. Photograph and cross-section microstructure of the thermal cycled sample P is presented in Fig. 4.13. It seems, sample P had a similar failure mode to sample M, N and O. Delamination occurred within the top coat and was near to bond coat interface. TGO layer was also found on the bond coat, but the thickness was very thin (2-3 µm). Sample P not only had a high fracture toughness but also a high elastic modulus. Hence, a high thermal stress level is expected during thermal cycling. In order to obtain a better insight into how elastic modulus and fracture toughness affect thermal cycling lifetime of coatings, a simplified evaluation was made.

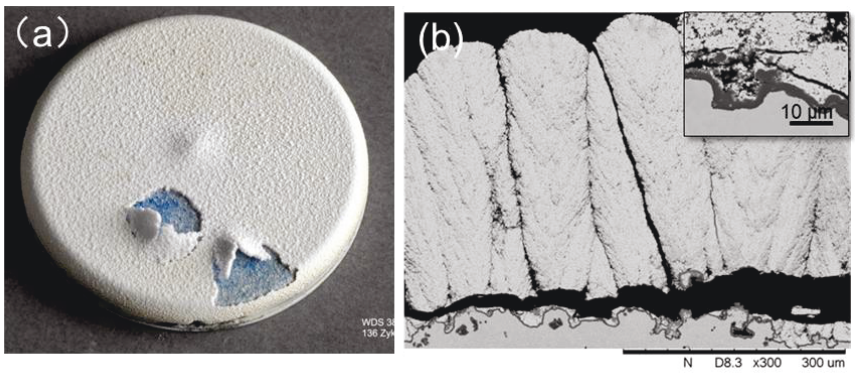

Fig. 4.13 Photograph (a) and cross-section microstructure SEM image (b) on thermal cycled sample P.

Due to the thermal expansion mismatch between the YSZ top coat and the metallic substrate, thermal stress which is the driving force for crack propagation is built up during the thermal cycling. This stress is determined by the strain $\Delta\varepsilon$ which is proportional to the mismatch of thermal expansion coefficients of coating and substrate (~5×10^{-6} /K) multiplied by temperature change (~1000 K) during cycling and elastic modulus E of the top coat. This is a typical estimation of APS coatings [164]. Due to the column gaps and vertical cracks penetrating through the whole thickness of top coat, a great reduction of thermal strain is expected in columnar structured SPS coatings [20, 165]. Thus, a half strain of APS coating is estimated in columnar SPS coatings.

Hence, crack propagation and resultant failure is governed by stress intensity factor K_I of the coating, which is proportional to thermal stress multiplied by square root of defect size c and a geometry factor Y. To simplify the model, geometry factor Y = $2/\pi^{1/2}$ for spherical pores is assumed. Stress intensity factor can be described with the following equation:

$$K_I = Y\sigma\sqrt{c} \approx Y\Delta\varepsilon E\sqrt{c} \tag{4.2}$$

Generally, the crack propagation rate of crack $\frac{\mathrm{dc}}{\mathrm{dt}}$ is proportional to the ratio of stress intensity factor to critical stress intensity factor K_{IC} (or fracture toughness) with an exponent *n* (often rather high). Assuming initial crack size *c* is much smaller than the critical crack size c_c, the lifetime of coating t_f obtained by integration can be estimated by:

$$t_f \propto c\left(\frac{K_{IC}}{Y\Delta\varepsilon E\sqrt{c}}\right)^n \tag{4.3}$$

The results are given in Table 4.3. The initial defect size *c* was estimated with image analysis. In order to ensure distinction on statistics results, only the largest 10% pores were counted. The average equivalent circle diameter of pores is presented in Table 4.3.

Table 4.3 Input parameters and evaluation according to equation (4.3) for SPS coatings.

Sample	Defect size (μm)	Strain	Hardness (GPa)	Elastic modulus (GPa)	Fracture toughness (MPa·$m^{1/2}$)	Lifetime (cycle)	K_{IC}/K_I	Lifetime/defect size (cycle/μm)
M	0.93	0.0025	9.6	113.7	1.5	177	4.8	190.3
N	1.38	0.0025	6.2	81.9	1.0	76	3.7	55.1
O	0.67	0.0025	8.3	100.7	1.8	244	7.7	364.2
P	0.31	0.0025	8.9	125.6	2.2	151	11.3	503.3

A plot of the data points plotted on a log-log scale is shown in Fig. 4.14. The rather linear distribution of data points in this plot indicates that equation (4.3) might be an appropriate description of the relations between mechanical property and lifetime data. It seems both elastic modulus and fracture toughness play an important role in determining the lifetime of coatings. Increasing fracture toughness by decreasing porosity inevitably leads to high elastic modulus which will introduce high

thermal stress during cycling. It seems mechanical properties of the top coat has already been optimized. Thus further increase fracture toughness of coatings along can not improve the lifetime of TBCs. Premature failure of top coat might be related to factors which are independent of mechanical properties. Thus new methods to further increase the lifetime of coatings are explored and discussed in chapter 5.

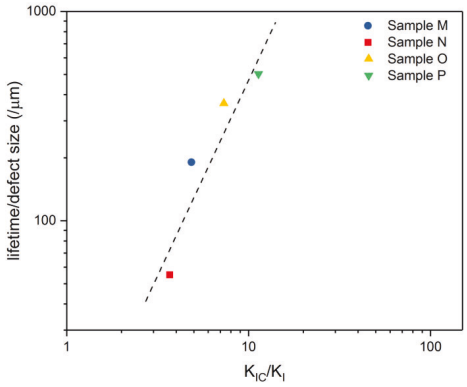

Fig. 4.14 Plot of lifetime t_f divided by initial defect size c as a function of the critical stress intensity factor divided by the apparent one (as shown in equation 4.3) for sample given in Table 4.3.

5 Results and Discussion Part Ⅱ: New Approaches to Improve Thermal Cycling Lifetime of Coatings

In the previous part, Chapter 4, a relationship between mechanical properties and lifetime of coatings was introduced. Both elastic modulus and fracture toughness of top coat greatly affected the lifetime of TBCs. By adjusting the Yttria content and mechanical properties of the coating, the lifetime of coatings was improved; but this improvement is limited. The lifetime of SPS TBCs compared with APS TBCs was still short. Thus in this part, innovative methods were explored to improve the lifetime of SPS TBCs.

5.1 Analysis of the Failure Mechanism of Columnar Structured SPS TBCs

For typical APS coatings, there are three basic failure modes under thermal gradient cycling condition. One is related to Al depletion in bond coat resulting in the formation of large amounts of Ni, Cr-rich spinel oxides [61]. This failure mode also indicates the potential of TBCs. For the second mode, delamination happens along the interface of the top coat and TGO or within TGO. This delamination is related to the elastic strain energy accumulated in TGO during cooling [60]. However, often, especially for those coatings under high cyclic load conditions, the delamination usually occurs within the top coat and near to the bond coat interface. The driving force for such delamination is thermal stress introduced by thermal misfit between the ceramic top coat and the metallic bond coat/superalloy. At elevated temperature, thermal stress in the top coat is assumed to be released by creep. When the top coat is cooled down to room temperature, the top coat is under an overall compressive stress [7]. Moreover, the highly undulation nature of bond coat (typically 5-10 μm in Ra), which is essential to the bonding between the overlaying ceramic top coat and the bond coat, introduces additional radial stress in the vicinity of TGO/top coat interface [164]. A typical failure mechanism of APS TBCs under thermal cycling load is simply illustrated in Fig. 5.1. Generally, when the TGO layer is very thin, APS coatings have a tensile stress at areas on top of bond coat asperities, and a compressive stress at areas in the valleys, as shown in Fig. 5.1 (a). Cracks at areas under the tensile stress start to horizontally grow toward both sides. When these cracks reach to areas where is under compressive stress, the growth of cracks is stopped. With increase of cycling time, TGO layer grows thicker. As a result of the TGO growth, asperities of bond coat constitute a large fraction of TGO. Thus, the radial thermal stress is locally dominated by the thermal misfit between the ceramic top coat and bond coat/TGO composite, rather than just the top coat and bond coat. When TGO exceeds a critical thickness (5-6 μm), the coefficiency of thermal expansion for the bond coat/TGO composite becomes lower than that of the top coat [10] [62]. This reverses radial thermal stress in valleys from a compressive stress to a tensile stress, as shown in Fig. 5.1(c). Therefore, cracks reached valley areas are able to continuously propagate and converge with adjacent cracks leading to a final failure of TBCs. Penetration of crack through the valley area controls such failure of APS TBCs [166]. As one precondition for such failure is that the TGO exceeds the critical thickness, coatings with such failure mode generally has a relatively long lifetime.

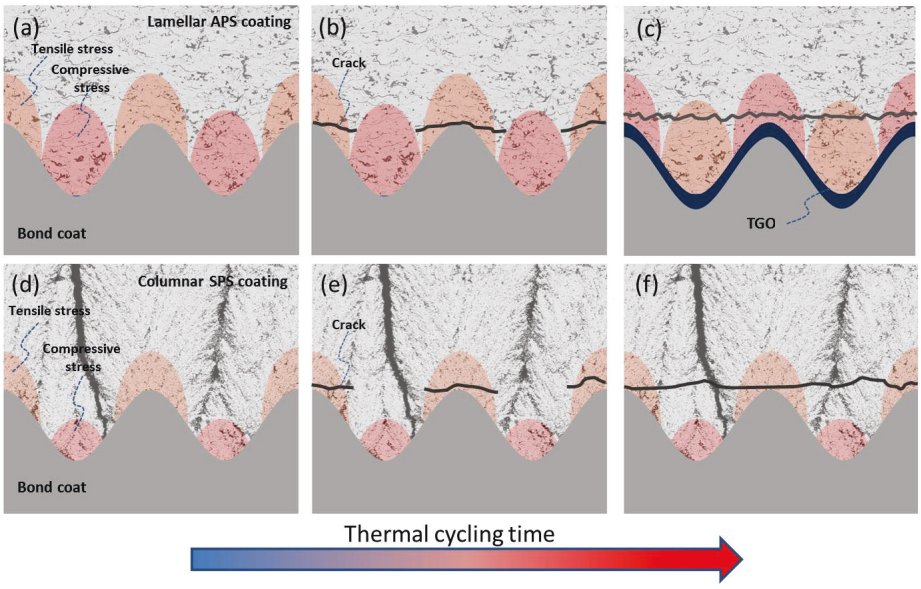

Fig. 5.1 Schematic illustration on the typical failure mechanism of lamellar APS TBCs and promoted failure mechanism of columnar SPS TBCs under thermal cycling load.

As presented in the previous Chapter, SPS coatings exhibited a similar failure mode with APS coatings under high cyclic thermal load. Delamination happened within top coat and was close to the bond coat interface. The major difference is that SPS coatings failed before TGO exceeds the critical thickness. The TGO only has a thickness of about 2-3 µm at its failure. To explain such premature failure of SPS coatings, a failure mechanism of columnar structured SPS TBCs is developed.

Due to the deposition mechanism of SPS, columns naturally grow on asperities of bond coat, as shown in Fig. 5.1(d) [132, 167]. In addition, porous gaps and vertical cracks originate from the valleys of bond coat and vertically penetrate through the whole top coat. This special structure might lead to a redistribution of the radial thermal stresses at the vicinity of top coat/bond coat interface. Due to the undulation of bond coat, radial thermal stresses are also introduced into the vicinity of top coat/bond coat interface. Similar to APS TBCs, columnar SPS TBCs have a tensile stress at area on top of bond coat asperities and a compressive stress at areas in the valley. However, due to the porous column gaps and vertical cracks in valley, the compressive stress is greatly reduced and the area under compressive stress is also reduced as illustrated in Fig. 5.1(d). Under the tensile stress, cracks initiate on top of asperities, as shown in Fig 5.1(e). These cracks horizontally propagate towards both sides. As the areas under compressive stress are greatly reduced, cracks need not penetrate the areas which are under compressive stress. Therefore cracks are able to easily

penetrate the valleys without TGO reaching to the critical thickness and conjoin with adjacent cracks leading to final failure of columnar SPS TBCs. Redistribution of radial thermal stress, especially reduction of compressive stress in the valley areas, might be the reason for the premature failure of the SPS TBCs.

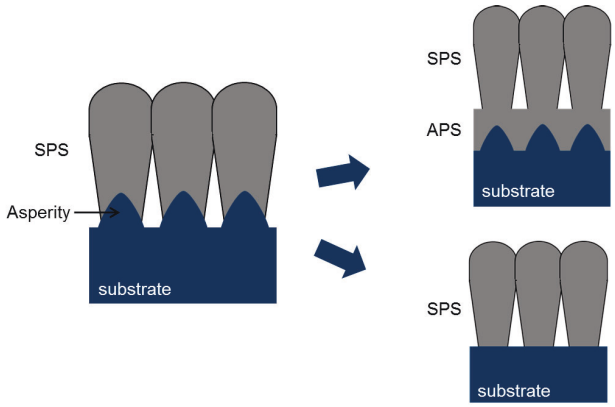

Fig. 5.2 Schematic on the architecture of columnar SPS coatings sprayed on a highly rough bond coat and two novel architecture designs for SPS coatings.

According to this promoted failure mechanism, two novel architecture designs were promoted as shown in Fig 5.2. One is a double-layered design. Before depositing columnar SPS top layer, a thin layer of APS under-layer is deposited. With this design, the compressive stress in the valley area is expected to be kept. And also the columnar structured top layer is expected to impart high strain tolerance to the coating leading to excellent thermal cycling performance. The other one is depositing SPS top coat on a low roughness bond coat. As reported by Ahrens [168], both radial tensile stress and radial compressive stress are positively correlated to the amplitude of asperities. By reducing the amplitude of bond coat asperities, radial thermal stress level would be reduced. This might lead to a better thermal cycling performance of TBCs.

5.2 APS YSZ/SPS YSZ Double-Layered Coatings

The APS YSZ/SPS YSZ double-layered coating named as sample Q consists of two YSZ ceramic layers, SPS top layer and APS under-layer. The top layer was sprayed with TZ-4Y suspension with a solid content of 5 wt%. The detailed information on this suspension and the corresponding powder are listed in section 3.2. Spraying parameters for SPS top layer is listed in the Appendix. The under-layer is a standard APS YSZ layer. A commercially available YSZ powder Metco 204 NS (Sulzer Metco, Wohlen, Switzerland) with internal number YSZ 412 M was used. APS YSZ under-layer was deposited with a TriplexPro 210 plasma torch (Sulzer Metco, Wohlen, Switzerland) on as-sprayed bond coats (VPS, Amdry 9954). Spraying parameter for standard APS YSZ under-layer is listed in the Table 5.1.

Table 5.1 Spraying parameters for standard YSZ under-layer.

Spraying parameter	Value
Spraying distance (mm)	200
Speed of torch (mm/s)	500
Plasma gas (slpm)	Ar (46), He (4)
Current (A)	420
Input power (kW)	37.6
Torch	TriplexPro 210

Microstructures of as-sprayed sample Q is presented in Fig. 5.3. For as-sprayed sample Q, the under-layer was a typical lamellar structured APS coating (100 µm in thickness) with a large amount of pores and cracks. Some pores and cracks had a size of tens of microns. It seems this APS layer thoroughly fit into the valley of the bond coat. Above this under-layer, a SPS top layer with a thickness of about 436 µm was applied. It had a mixed microstructure of columnar and vertical cracked. Columns and vertical cracks originating from the top layer/under-layer interface can be obersved in the top layer, as shown in Fig. 5.3. It seems APS under-layer was able to provide asperities for the growth of columns. But the number of asperities, which are suitable for column growth, was limited. Some region shows few columns. This led to an accumulation of tensile stress in the top coat and finally led to vertical cracks. As shown in Fig. 5.3 (b), the top layer perfectly fit into the rugged under-layer surface. Due to the same contrast under SEM, the interface between these two layers cannot be clearly seen. As no delamination was found in this area, the bonding between these two layers was good. Due to the much smaller splats sizes of SPS, the top layer showed a much finer microstructure with submicron pores and cracks [13, 129]. In addition, a large number of spherical particles filling in column gaps were also clearly seen in Fig. 5.3 (b). These particles probably formed by solidification of droplets before reaching to the substrate.

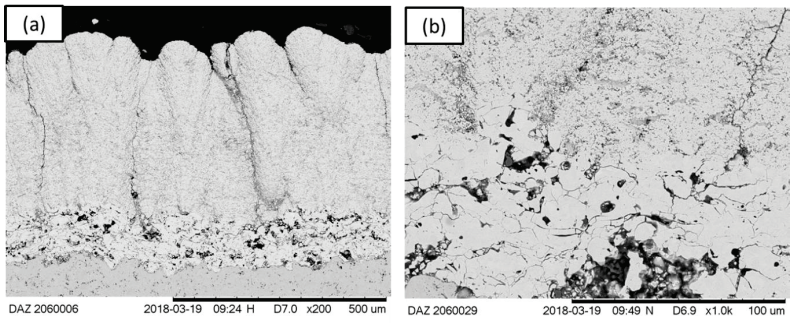

Fig. 5.3 Microstructure of as-sprayed sample Q (a) microstructure at top layer/under-layer interface (b).

Table 5.2 Overview on thermal cycled sample Q.

Sample	WDS No.	Thickness (μm)	Bond coat/top coat interface temperature (˚C)	Top coat surface temperature (˚C)	Top coat temperature gradient (˚C/μm)	Lifetime (cycles)
Q	WDS 3909	~564	1075	1387	0.55	1512
	WDS 3910	~547	1093	1396	0.51	1196

Sample Q was subjected to thermal cycling test. Overview of testing conditions and cycling lifetime are presented in table 5.2. After cycling, sample Q had an average lifetime about 1354 cycles which is much longer than that of standard APS coatings tested at similar conditions [161]. Photograph of the thermal cycled sample Q is presented in Fig. 5.4 (a). Even though the coating is still attached at the substrate; a large area of delamination occurred beneath the top coat. In addition, curl-up of top coat at failed area can be observed clearly. This curl-up might be attributed to different shrinkage rates of the top layer and under-layer at high testing temperature. This difference on shrinkage rate could be attributed to different intrinsic shrinkage rates of these two layers and thermal gradient through the coating thickness [169, 170]. Lamellar structured under-layer had a lower shrinkage rate in the in-plane direction as a result of the high aspect ratio of the splat. This results that the top layer shrank much larger than under-layer in the in-plane direction. In addition, thermal gradient about 300 ˚C through top layer led to faster sintering and larger shrinkage rate at the area close to surface.

The cross-sectional microstructure of the thermal cycled sample Q is presented in Fig. 5.4 (b). It seems sintering led to obvious modification on top coat microstructure. Due to the sintering, broadening of column gaps was clearly observed. These wide column gaps penetrated through the top layer and ended at the top layer/under-layer interface. In addition, the column gaps exhibited an elongated inverted triangle shape. Closer to surface, the column gap was wider. This also indicates different shrinkage rates through the top layer. There is no delamination observed at top layer/under-layer interface. The bonding between these two layers was strong enough to survive from the harsh cycling tests. The delamination happened at the interface of top coat/TGO, as seen in Fig. 5.4 (c). The thickness of TGO was more than 7 μm. Except for the dense alumina, porous and fast-growing spinel phase comprising Cr/Ni/Co oxides was also found in the TGO [171]. As a result of long cycling lifetime, Al depletion happened in bond coat leading to the formation of fast-growing spaniel oxides. It seems the growth of TGO, especially fast-growing oxides, led to the final failure of the TBCs.

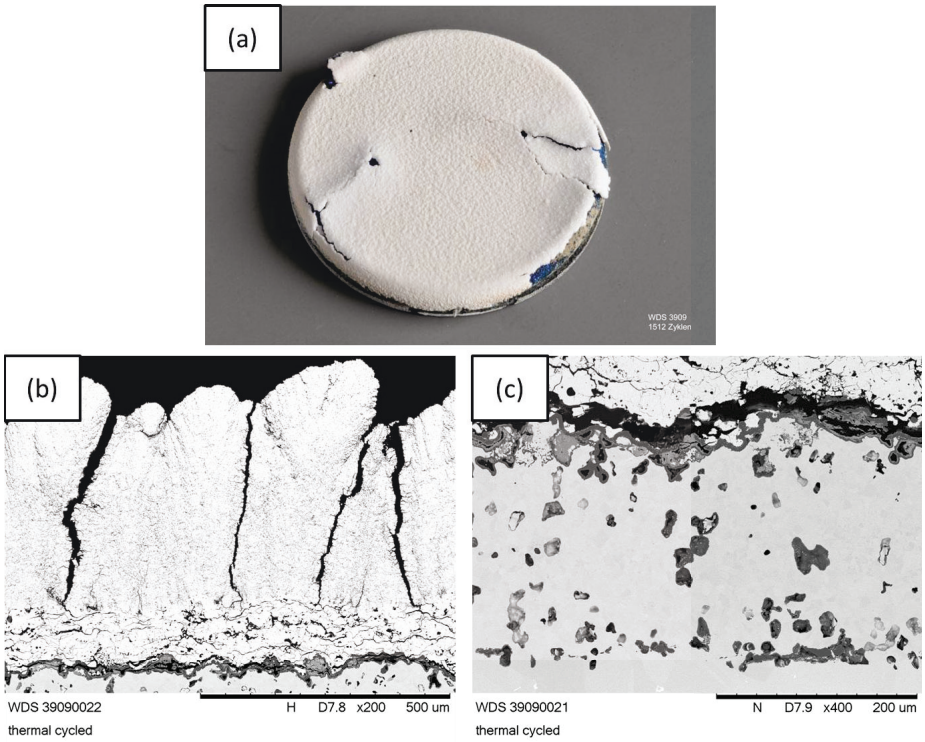

Fig. 5.4 Photograph of thermal cycled sample Q (a), the microstructure of thermal cycled top coat (b), the microstructure of thermal cycled bond coat (c).

To investigate the phase evolution of YSZ, XRD analysis was also performed on as-sprayed and thermal cycled samples Q, as presented in Fig. 5.5. Only peaks of tetragonal t' YSZ phase was detected in the as-sprayed sample Q. After cycling, obvious sharpening of tetragonal peaks was observed. This indicates significant grain growth in the coating during cycling. In addition, as shown in Fig. 5.5 (b), peak t (004) shifted to a lower angle while peak t (220) shifted to a higher angle. The shift of peak t (004) towards lower angle indicates tetragonal phase in thermal cycled sample Q had a higher $^{c}/_{a\sqrt{2}}$ ratio. A new peak appeared between t (004) and t (220), indicating the formation of the cubic YSZ phase [67, 148]. The formation of cubic phase could reduce fracture toughness of the coating; but no peak of monoclinic phase was observed from the thermally cycled sample as shown in Fig. 5.5 (c). As no delamination happened within top coat, Phase transformation was probably not the cause of coating failure in this case.

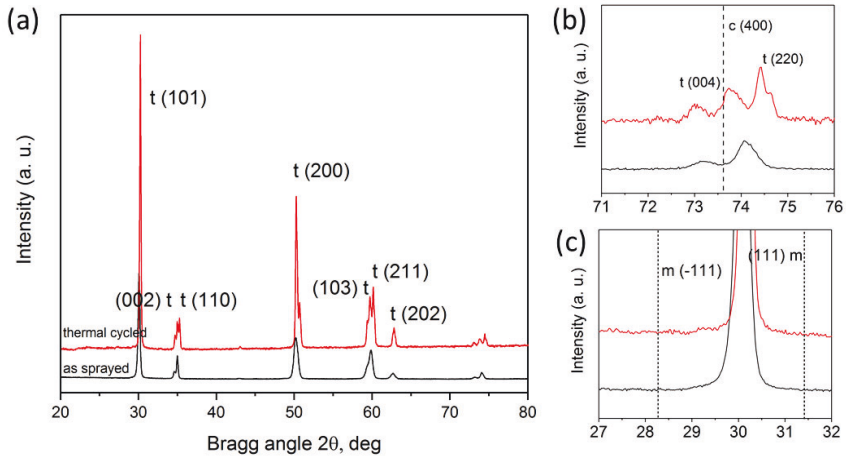

Fig. 5.5 XRD diagram of sample Q (a), diagrams zoomed in Bragg angle range of 70-76 ˚ (b) and 27-32 ˚ (c).

As reported by Nordhorn et al. [172], lifetimes of APS coatings are very sensitive to bond coat temperature which determines the growth rate of TGO. With 30 ˚C increase on bond coat temperature, the lifetime of TBCs could be halved. In order to accurately compare thermal cycling lifetime with APS coatings, bond coat temperature of samples Q must be known. To calculate bond coat temperature, the thermal conductivity of SPS top layer was assumed to be 1.0 W/mK.

The lifetimes of samples Q as well as standard APS coatings are plotted into an Arrhenius plot as shown in Fig. 5.6. The logarithm of high-temperature dwelling time is plotted as a function of inverse one-thousandth bond coat temperature. Due to the similar bond coat chemical composition with APS TBCs, same fitting line slop with APS TBCs is assumed for samples Q. The fitting line of sample Q is obviously higher than that of standard APS coatings. This implies samples Q had a better cycling performance than APS coatings. This excellent cycling performance could be attributed to the columnar top layer which is able to impart high strain tolerance to TBCs and lamellar structured APS under-layer which is able to keep the compressive stress in valleys and retard crack growth in the top coat. The success of such double-layered design suggests that the failure mechanism of columnar SPS TBCs proposed in section 5.1 is correct.

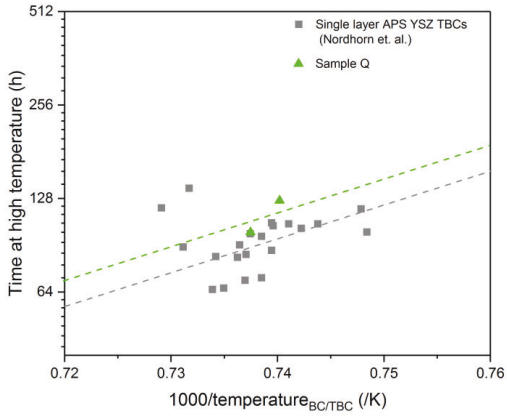

Fig. 5.6 Arrhenius plot on thermal cycling lifetime of samples Q and standard APS coatings.

5.3 Coatings Deposited on Grinded Surfaces

According to the promoted failure mechanism of columnar SPS TBCs, the other architecture design is to deposit top coat on a low roughness bond coat. Similar with APS coatings, SPS coatings are also formed by overlaying splats. For APS coatings, the bonding mechanism between top coats and bond coats is mechanical interlocking between splat and asperities of the bond coat. Therefore, the same mechanical bonding mechanism is assumed for SPS coatings. As introduced in section 5.1, the undulation of bond coat is very important for the bonding of APS coatings. To deposit top coat on lower roughness bond coat without reducing the bonding strength of SPS coatings would be challenging. As presented in chapter 4, Fig. 4.1 and Fig. 4.3, SPS top coats were deposited on mirror polished, grinded and sandblasted bond coat with different spraying distances. All these samples showed poor bonding as horizontal cracks exist at the top coat/bond coat interface. This indicates conventional surface treatment would greatly weaken the bonding strength.

In this part of the work, the as-sprayed bond coat was firstly grinded with sandpaper to reduce roughness. But at the same time, the asperities which act as anchors providing bonding strength were also destroyed. As illustrated in ref. [117] and [128] for best mechanical adhesion, the size of asperities must be adapted to the mean size of the splats. In addition, the flattening splat must be able to penetrate within the undercuts. Thus small asperities with sizes suitable for SPS splat size are necessary. To ensure enough bonding strength between top coats and grinded substrates, the grinded substrates were oxidized in air to form a thin layer of TGO. The oxidation parameters are listed in Table 5.3. After oxidation, the roughness of the bond coats (Ra) was increased from 0.2 to 0.5 µm.

Table 5.3 Oxidation parameters for grinded samples.

Sample condition	Roughness after grinding (Ra, µm)	Heating up rate (K/min)	Target temperature (˚C)	Dwelling time (hour)	atmosphere	Roughness after oxidation (Ra, µm)
Grinded with #800 sand paper	**0.2**	**10**	**1050**	**18**	**air**	**0.5**

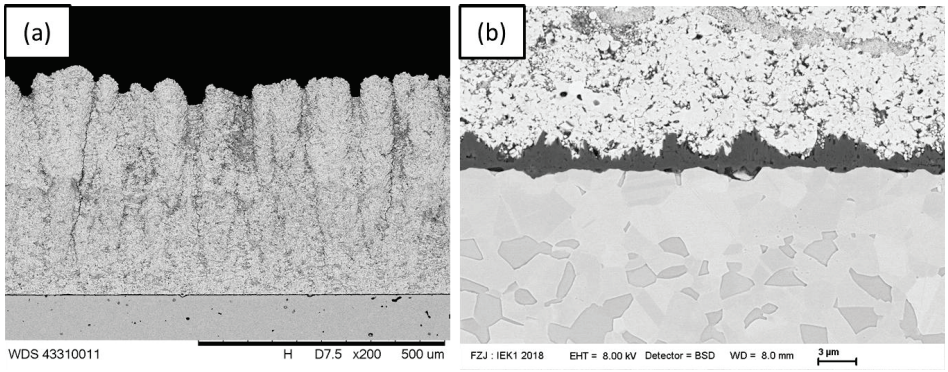

Fig. 5.7 Microstructure of as-sprayed sample R (a) and detailed microstructure of as sprayed sample R at the top coat/bond coat interface with a higher magnification (b).

After oxidation, SPS top coat was sprayed on this oxidized substrate (sample R). The detailed spraying parameters are listed in the Appendix. The microstructure of the as-sprayed samples R is presented in Fig. 5.7. As a result of the long spraying distance (100 mm) and low roughness bond coat, sample R had a microstructure similar to sample E and F (Fig. 4.2). Sample R exhibited a columnar structure with a high column density. Similar to sample E and F, these columns did not directly grow on the bond coat but developed in a distance from it. At regions close to bond coat, as shown in Fig. 5.7 (a), coating had a homogeneous microstructure. No column and vertical cracks can be found in this area with a thickness of about 100 µm. Detailed microstructure at the top coat/bond coat interface is also presented in Fig. 5.7 (b). Due to oxidation, a thin layer of TGO with a thickness of about 2 µm was formed on the bond coat. Beneath this TGO layer, an Al depletion zone with a thickness of about 5-7 µm was also found. This TGO layer had an undulated surface with a large number of micron-sized asperities. These alumina asperities were also able to introduce radial out of plane thermal stress into the top coat. But due to the smaller thermal misfit between Alumina

(8.0×10^{-6} K^{-1} in CTE) and top coat (10.7×10^{-6} K^{-1} in CTE), the thermal stress level was expected to be lower [173]. Due to the small size of splats, the top coat perfectly fit into the undulated TGO surface. As no crack could be found at top coat/bond coat interface, the bonding strength between them is expected to be strong.

Table 5.4 Overview of thermal cycled sample R.

Sample	WDS No.	Thickness (μm)	Bond coat/top coat interface temperature (˚C)	Top coat surface temperature (˚C)	Top coat temperature gradient (˚C/μm)	Lifetime (cycles)
R	WDS 4332	~500	1086	1393	0.61	366
	WDS 3887	~514	1088	1397	0.57	342

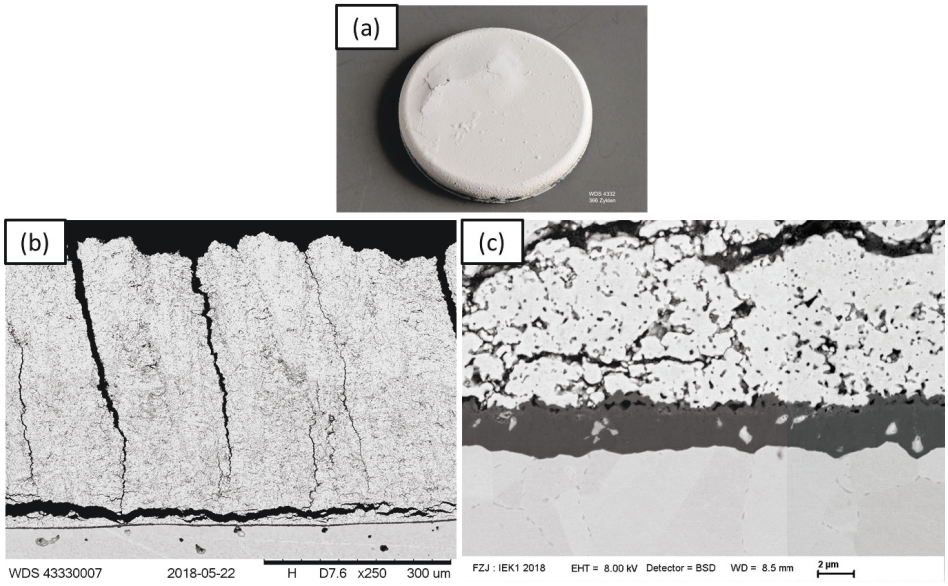

Fig. 5.8 Photograph and SEM images of thermal cycled sample R.

After spraying, sample R was tested in a thermal cycling test. The testing conditions are listed in Table 5.4. Photograph and microstructure of the thermal cycled sample R are also presented in Fig. 5.8. Even though, the coating still attached on the substrate, a large area of buckled coating could be observed. Thermal gradient through TBCs could not be maintained. Thus the cycling tests were stopped. After cycling, as shown in Fig. 5.8 (b), some column gaps opened up and reached the interface of TGO. Delamination occurred within top coat and close to the TGO interface. Within the bond coat, an Al depletion zone with a thickness about 20 μm was found. A higher magnification

picture is presented in Fig. 5.8 (c). The thickness of the TGO was 3-4 μm. It can be found that the TGO layer consisted of two layers with difference on porosity. As reported by Naumenko et al. [60], during cycling, the growth of TGO is often controlled by inward oxygen diffusion. The new TGO is formed beneath the original TGO layer which remains unaffected. Thus it is speculated that the top layer with higher porosity was probably formed by pre-oxidation. And the dense layer was formed during cycling. It should be notified that the bonding between top coat and TGO was very good, as no delamination was found at the interface. It is hard to say the bonding strength only derive from the mechanical interlocking. Probably chemical bonding could also play a role in the bonding. The bonding mechanism for SPS coatings needs to be further investigated.

The average thermal cycling lifetime for sample R was 354 cycles. Compared with sample N (76 cycles) which was sprayed with the same spraying parameters but on an as-sprayed bond coat, lifetime of SPS TBCs was greatly improved. It seems this innovative design with low roughness bond coat is able to effectively improve lifetime by reducing out of plane stress. Compared with standard APS coatings, the lifetime of sample R was still short. Mechanical properties of sample R was tested with indentation. As-sprayed sample R had a hardness of 4.2 ± 0.5 GPa, an elastic modulus of 61.8 ± 4.2 GPa and a fracture toughness of 0.9 ± 0.2 MPa·$m^{1/2}$. Fracture toughness of sample R was much lower than that of samples M, N, O and P as seen in Table 4.3. Even though out of plane stress was reduced by reducing the roughness of bond coat, the relatively lower fracture toughness fascinate propagation of cracks during thermal cycling [2]. Probably by further optimizing the mechanical properties of sample R, such as increasing fracture toughness, the cycling lifetime of TBCs could be further improved.

6 Results and Discussion Part Ⅲ: Sintering Behavior of Columnar Thermal Barrier Coatings

As introduced before, TBCs are exposed to high temperature during service. Sintering effects can lead to significant modifications on microstructures of top coats, such as the healing of cracks, decrease of porosity and growth of grain size. As results of these processes, elastic modulus, hardness and fracture toughness of top coats are increased upon annealing. The change of mechanical properties can promote the failure of coatings [174-176]. Thus study on sintering effects can help to understand the failure mechanisms of TBCs. Thus in this part of the work, effects of sintering on microstructure and mechanical properties of SPS coatings was investigated. Furthermore, potential sintering effects on thermal cycling lifetime of coatings was also investigated and discussed.

6.1 Sintering Effect on Microstructure of Coatings

In this part of work, ethanol-based suspension made of NAMI YSZ powder with 10 wt% solid content was used to spray top coat. Detailed information on raw powder and suspension is presented in section 3.2. Nickel-based super-alloy IN738 plates (20×18×3 mm^3) with an MCrAlY (Amdry 9954) VPS bond coat (200 µm in thickness) were used as substrates. Detailed spraying parameters can be found in the Appendix. After spraying, samples were isothermally annealed at 1373 K for 1 h, 3 h, 10 h and 50 h, respectively. To facilitate description, these samples were named as S-1 h, S-3 h, S-10 h and S-50 h, respectively. The as-sprayed sample is named as S-0 h. In order to protect the substrates from oxidation, a mixture of Ar (97 vol.%) and H_2 (3 vol.%) was used as annealing atmosphere. After annealing, microstructure and mechanical properties of coatings were characterized as a function of annealing time.

Cross-section microstructures of coatings with different annealing time are presented in Fig. 6.1. The as-sprayed top coat, as shown in Fig. 6.1 (a), has a columnar structure with columns growing on asperities of bond coat. Columns are segmented by porous column gaps which are perpendicular to the bond coat and penetrate through the whole thickness of the top coat. In addition to the columns gaps, vertical cracks with a size of several hundred micrometers penetrating through whole top coat are also observed. These microstructure features are expected to impart high strain tolerance to the top coat [177, 178]. As a result of the relatively large particle size of powder in suspension (as shown in Table 3.1), sample S-0 h has a lower porosity compared with sample O which was sprayed with same spraying parameters.

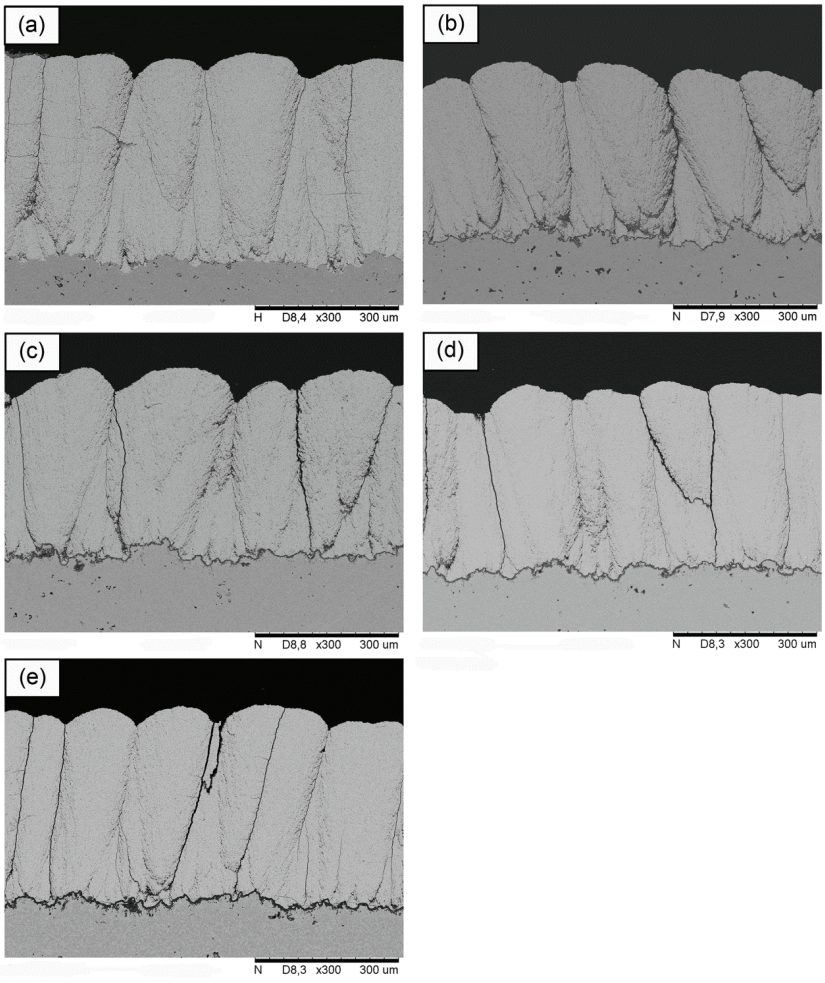

Fig. 6.1 Cross-section microstructure of top coats annealed at 1100 ˚C for different time; (a) as-sprayed (S-0 h), (b) 1 hour (S-1 h), (c) 3 hour (S-3 h), (d) 10 hour (S-10 h) and (e) 50 hour (S-50 h).

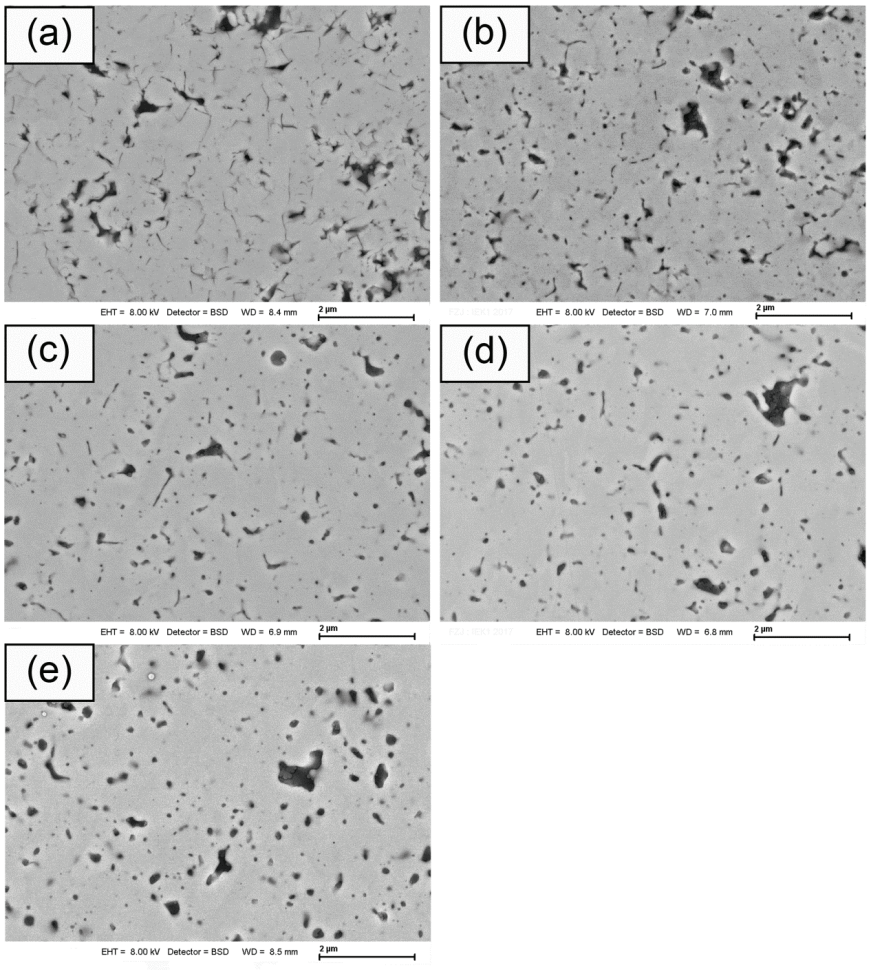

Fig. 6.2 Detailed cross-section microstructure of top coats annealed at 1100 ˚C with different time; (a) as-sprayed (S-0 h), (b) 1 hour (S-1 h), (c) 3 hour (S-3 h), (d) 10 hour (S-10 h) and (e) 50 hour (S-50 h).

With a higher magnification image, as presented in Fig. 6.2, the detailed microstructure within columns can be observed. A lot of microcracks and micropores with sizes of several micrometers or even in the submicron meter range can be observed. Micro-pores with irregular geometry randomly distributes in the coating. One interesting observation is that the most of the micro-cracks exhibit an orientation perpendicular to the bond coat interface as shown in Fig. 6.2 (a). Similar oriented

vertical micro-cracks were also reported in APS coatings [8, 179, 180]. It is assumed that vertical cracks found in sample S-0 h were formed due to the same mechanism. Formation of vertical micro-cracks in sample S-0 h might be attributed to the tensile stress formed in the coating during spraying. Due to the high deposition temperature (470-570 ˚C), as seen in the appendix, wetting between splats was improved leading to better contact of overlaid splats [2]. This also led to higher thermal conductivity and higher heat flux. Upon impacting on substrates, the molten splats were cooled down very quickly. However, shrinkage of the splats was restricted by the underlying massive body. Thus an extensive tensile stress was formed within splats. When this stress exceeds the strength of splats, vertical micro-cracks were formed.

Even though samples were annealed in Ar/H_2 atmosphere, a thin layer of TGO was still found on the bond coat of annealed samples as shown in Fig. 6.1. This thin layer of TGO barely affects the microstructures of the top coat. Vertical cracks and column gaps were well retained in the coatings after a long time of annealing. Column and vertical crack density are presented in Fig. 6.3. The evaluation on which Fig. 6.3 based was carried out as follows. A line parallel to the bond coat interface was drawn at the middle of top coat thickness. Vertical cracks and columns intersected with this line were counted. The column density varies from 4.8 /mm to 6.5 /mm and the vertical crack density varies from 6.2 /mm to 7.6 /mm. Considering associated error, there seems to be no obvious change in column and vertical crack density during annealing. This indicates that vertical cracks and column gaps which penetrate through the whole thickness remain after long-term annealing.

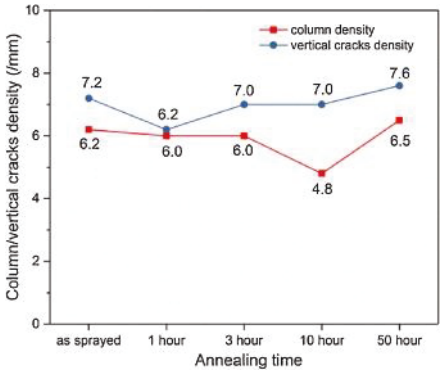

Fig. 6.3 Vertical cracks and column density of top coats as a function of annealing time.

Furthermore, due to the shrinkage of the coatings, as shown in Fig. 6.1, the width of vertical cracks/column gaps expand gradually with the increase of annealing time. Even after one hour of annealing, the expansion of cracks and column gaps can already be clearly seen. Due to the large size of the vertical cracks and column gaps compared to micro-cracks and column gaps, it is assumed that porosity with Equivalent Circle Diameter (ECD) larger than 2 µm mainly contributed to vertical

cracks and column gaps. Based on this assumption and by carefully setting the threshold, porosity with ECD larger than 2 µm was counted with image analysis. The statistical results are presented in Fig. 6.4. For as-sprayed coating (S-0 h), the porosity was only about 1.3 %. With the increase of annealing time, the porosity increased gradually. After 50 hours of annealing, porosity of sample S-50 h increased up to 2.3 %. As mentioned before, through thickness vertical cracks and column gaps could impart strain tolerance to coatings. Thus, this indicates sintering effect might increase the strain tolerance of coatings by expanding vertical cracks and column gaps [181].

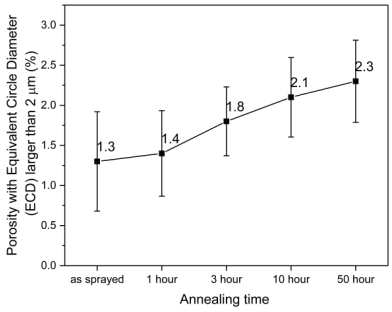

Fig. 6.4 Porosity with equivalent circle diameter larger than 2 µm of coatings after different annealing time at 1373 K.

The sintering effects on the microstructure of coatings were also investigated on basis of higher magnification SEM images, as seen in Fig. 6.2. It seems sintering has a great influence on the microstructure of coatings. Already after one hour of annealing, the number of micro-cracks within column was greatly reduced. Most of micro-crack healed and extremely fine elongated pores remained in situ. The sharp tip of remained micro-cracks and micro-pores blunted. After 3 hours, the number of micro-cracks further decreased and the extremely fine pores turned into more spherical coarser pores. After 10 hours, micro-cracks could be barely observed from the cross-section. After 50 hours of annealing, all micro-cracks disappeared and micro-pores became courser and more spherical. As reported by Golosnoy et al. [182], both surface and grain boundary diffusion as transport mechanism are active at 1100 ˚C. The healing of micro-cracks and spheroidization of micro-pores can be explained by surface diffusion; atoms present on the surface of micro-cracks and micro-pores would diffuse in the direction of decreasing chemical potential, in other words, in the direction of reducing surface area.

6.2 Sintering Effect on Phase and Grain Size of the Coatings

The XRD patterns of as sprayed and annealed samples are depicted in Fig. 6.5. All the observed peaks in the coatings belonged to the tetragonal phase. Due to a relatively low annealing temperature (1373 K), no obvious phase transformation can be detected. Based on XRD

measurements, domain size was also calculated and presented in Fig. 6.6. It seems sintering effect had a significant effect on domain size (significant grain growth occurred). For as-sprayed coating, a domain size of about 50 nm was calculated. With an increase of annealing time, domain size increase gradually. Finally, after 50 hours of annealing, a domain size about 200 nm was detected from sample S-50 h. limited by measurement range (< 200 nm) through XRD technique, the exact domain size of the coating after 50 hours of annealing could not be obtained. Overall, a significant grain growth was detected on the coating. This observation is consistent with the observation of Ganvir et al. on the sintering of SPS coatings [177, 183].

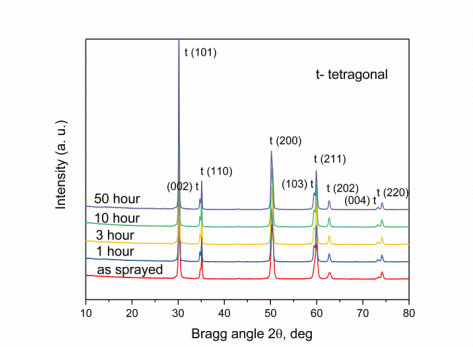

Fig. 6.5 X-ray diffractograms of coatings after different annealing time at 1373 K.

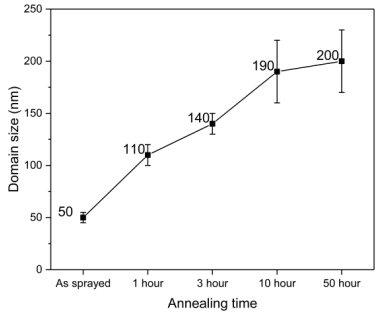

Fig. 6.6 Domain size of coatings after different annealing time at 1373 K.

6.3 Sintering Effect on Porosity of Coatings within Columns

Porosity within columns as an important character of coatings was also measured with image analysis. To avoid effects of column gaps and vertical cracks, SEM images with high magnification (10000 ×) were taken from the center of the columns. In order to get reliable results, 10 images with

similar contrast and brightness were used. The porosity of coatings after different annealing time is depicted in Fig. 6.7. Porosity of as-sprayed coating was about 9.4 ± 1.8 %. Due to sintering effects, porosity within column gradually decreased with increasing of annealing time. After 50 hours of annealing, porosity of coating decreased to 5.8 ± 0.4 %. The porosity of coating as an important character relating to mechanical properties will be discussed later. The decrease of porosity can be attributed to the grain boundary diffusion which can lead to volume change.

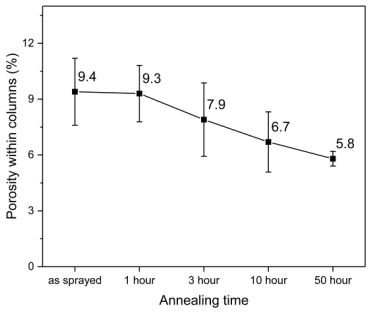

Fig. 6.7 Porosity of coating within columns after different annealing time at 1373 K.

6.4 Sintering Effect on Mechanical Properties of Coatings

Hardness and elastic modulus of coatings as a function of annealing time were measured with indentation tests and the respective results are presented in Fig. 6.8. To avoid effects of vertical cracks and porous column gaps, all the indentations were made at the center of the columns. For as-sprayed coatings, the hardness was 11.2 ± 0.4 GPa; the elastic modulus was 103.6 ± 4.4 GPa. After annealing, hardness and elastic modulus showed similar trends, both of them increased gradually with increasing annealing time, although the elastic modulus data already indicates a saturation effect. After 50 hours of annealing, hardness increased to 12.9 ± 1.0 GPa; the elastic modulus increased to 159.4 ± 8.3 GPa. It seems sintering has a more significant effect on elastic modulus. The increase of hardness and elastic modulus can be attributed to sintered microstructure modification, such as decrease of porosity and healing of micro-cracks as shown in Fig. 6.2 and 6.7.

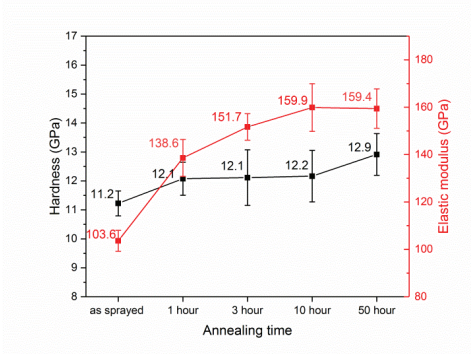

Fig. 6.8 Hardness and elastic modulus of coatings after different annealing time at 1373 K.

Fracture toughness of coatings was also characterized via Vickers indentation fracture toughness tests. To simplify the discussion, the direction running parallel to the substrate was defined as “in-plane”, while the direction perpendicular to the substrate was referred to as “out of plane”. Images of indentation print made on the cross-section of coatings were taken with a confocal laser microscope and are presented in Fig. 6.9. The size of indentation print was more than 20 µm which is much larger than the size of micro-pores. For as-sprayed coating, the in-plane cracks which were induced by indentation appeared to be significantly shorter than the out of plane cracks which were also induced by indentation. This implies that the as-sprayed coating had an anisotropic fracture toughness. However, after 50 hours of annealing, this different on crack length disappeared. This indicates after a long time of annealing, the fracture toughness of coating is isotropic.

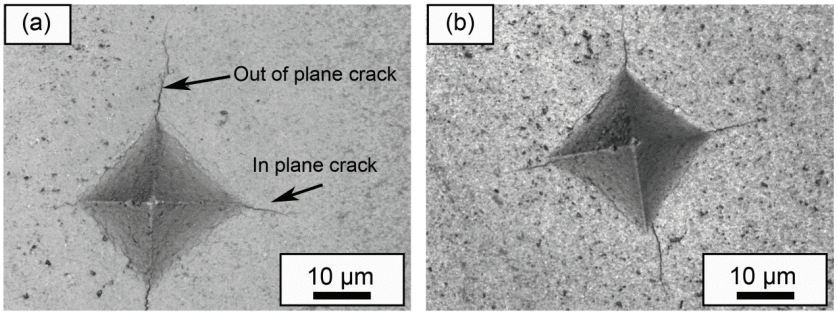

Fig. 6.9 Images of indentations imprinted on the cross-section of coatings. (a) as-sprayed, (b) annealed for 50 hours at 1373 K.

To quantify this difference in fracture toughness, the fracture toughness of coatings in different directions was evaluated and presented in Fig. 6.10. It seems that the as-sprayed coating possessed

the largest difference in fracture toughness which accounts to 0.6 MPa·m$^{1/2}$. After one hour of annealing, the out of plane fracture toughness increased from 2.0 ± 0.3 MPa·m$^{1/2}$ to 2.3 ± 0.4 MPa·m$^{1/2}$. The remaining fracture toughness difference narrowed to only about 0.1 MPa·m$^{1/2}$. Considering the relatively large experimental uncertainty, this difference appears to be not significant. With further increasing annealing time, the fracture toughness of coating in both directions increased gradually. After 50 hours of annealing, the fracture toughness increased to about 3.0 MPa·m$^{1/2}$. The apparent anisotropic fracture toughness of the as-sprayed coating might be attributed to orientated microstructure and residual stress in the coating. As shown in Fig. 6.2, the as-sprayed coating had an orientated microstructure. Most of the micro-cracks had an out of plane orientation. These orientated micro-cracks provided free surfaces for propagations of cracks and led to lower out of plane fracture toughness.

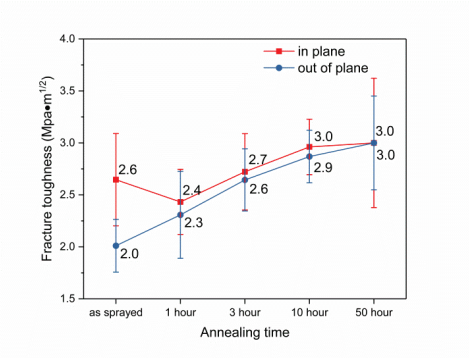

Fig. 6.10 Fracture toughness of coating after different annealing time at 1373 K.

Probably, the textured microstructure is not the only reason for anisotropic fracture toughness. Residual stress existing in coating could also contribute to anisotropic fracture toughness. Thus with a sin$^2\Psi$ technique, residual stress in the as-sprayed coating was investigated [184, 185]. The change of the inter-planar d-spacing (323) is plotted as a function of sin$^2\Psi$ in Fig. 6.11. By substituting slope of fitting line as shown in Fig. 6.11 into formula (3.3), a residual stress value can be obtained. ; E_{bulk} with a value of 210 GPa [27] and ν with a value of 0.22 [23] was used.

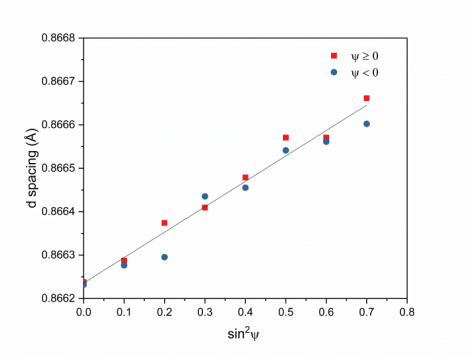

Fig. 6.11 (3 2 3) d-spacing against $\sin^2\Psi$ used for residual stress characterization of the as-sprayed coating.

In as-sprayed coating, a tensile stress with a level of about 100 MPa was determined with $\sin^2\Psi$ technique. This value is much higher than what was measured in columnar EB-PVD coatings (20-40 MPa) [186]. As shown in Fig. 6.1 (a), different to columns observed in EB-PVD coatings, columns were still slightly bonded with neighbor columns. Furthermore, the size of columns was much larger than the sizes of columns in EB-PVD coatings. It seems that the residual stress in the coating cannot be easily released by column gaps. These probably are the reasons for such high tensile stress in the as-sprayed coating. These tensile stresses might further reduce out of plane fracture toughness. In summary, the oriented micro-cracks and tensile stress both are assumed to contribute to anisotropic fracture toughness of as-sprayed SPS coating.

6.5 Sintering Effect on Thermal Cycling Lifetime of Coatings

In addition to sintering effects on the microstructures and the mechanical properties of coatings, the effect of sintering on thermal cycling lifetime of coatings was also investigated. As-sprayed (S-0h) and one hour pre-annealed (S-1h) coatings were selected for burner rig thermal cycling test. Cross-section microstructure of thermal cycled samples is presented in Fig. 6.12. It seems both samples had a similar failure mode. Cracks nucleated within the top coat. The growth of cracks which were parallel and near to the bond coat interface finally led to a failure of the coating. Furthermore, this failure mode was also similar to thermal cycled coating reported in section 4.

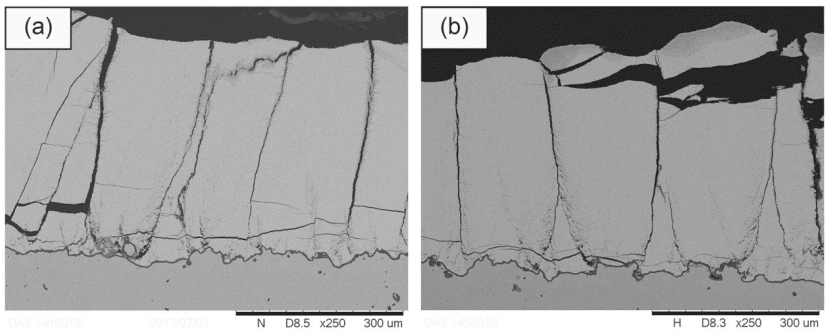

Fig. 6.12 Cross-section SEM image of thermal cycled coatings, (a) as-sprayed (S-0h), (b) pre-annealed for 1 hour at 1373 K before cycling (S-1h).

Table 6.1 Overview of thermal cycled sample S-0h and S-1h.

Sample	WDS No.	Thickness (µm)	Bond coat/top coat interface temperature (˚C)	Top coat surface temperature (˚C)	Top coat temperature gradient (˚C/µm)	Lifetime (cycles)
S-0h	WDS 3886	~360	1086	1295	0.58	124
	WDS 3887	~386	1090	1276	0.47	75
S-1h	WDS 3889	~391	1094	1337	0.62	328
	WDS 3890	~368	1091	1325	0.64	199

An overview of these samples is summarized in table 6.1. The average lifetime for sample Y-0h was about 100 cycles. The average lifetime for pre-annealed sample Y-1h was about 263 cycles which were more than twice of sample Y-0h. Hence, it seems that short time of pre-annealing improves the thermal cycling lifetime of the SPS coatings.

According to the work reported in section 4, thermal cycling lifetime, mechanical properties and microstructure of coatings can be correlated with formula 4.4. For a pre-annealed sample, as shown in Fig. 6.2 (b), most of the micro-cracks were healed after one hour of annealing. This decreased the initial defect size of the coating. In addition, due to the blunting of micro-pores and micro-cracks tips, the geometry factor was reduced. Both factors are assumed to lead to an increase of thermal cycling lifetime of the coating after 1 hour of pre-annealing. One thing needs to be clarified is that during thermal cycling test, the coating was also under sintering. However, high-temperature phase for one cycle is only about 5 min. this is too short to make significant modification on microstructure. Thus the effect of the first cycle on the initial microstructure of coating is neglected.

7 Results and Discussion Part Ⅳ: Performances of APS YSZ/SPS GZO Multi-layer Coatings

As introduced in the introduction, $Gd_2Zr_2O_7$ (GZO) as a promising TBC material attracted a lot of interest for more than two decades [20]. It has a high melting point (2570 ˚C) [25, 26], very good phase stability [29], a considerably low thermal conductivity (1.2 W/mK) [97], excellent CMAS penetration resistance [87] and a high CTE (9-11 × 10^{-6}/K) [97] which is close to that of YSZ. However, the relatively low fracture toughness of GZO which can lead to crack propagation even at very low-stress levels [112]. Furthermore, as reported by Leckie et al., GZO tends to react with alumina and forms a porous $GdAlO_3$ interphase [29]. This reaction product can weaken the protective function of alumina TGO and compromises the integrity of the TBC system. Thus a YSZ diffusion barrier layer is suggested at the interface between the bond coat and GZO layer to prevent this reaction. Double-layered structure can also take advantages of the high thermal stability, the low thermal conductivity of GZO and the high fracture toughness of YSZ leading to better performing TBCs [28].

In addition of searching new ceramic materials, achieving high strain tolerance microstructure which is critical for long-lifetime TBCs is another attractive research issue [2, 9]. Suspension Plasma Spraying (SPS) as a relatively new and cost-effective spraying technology has a great flexibility on the microstructure of sprayed coatings. With SPS, homogeneous, vertical cracked and columnar structured coating can be easily obtained. Especially, vertical cracked and columnar structured coatings with high strain tolerance make SPS a great potential technology for applying high-performance TBCs. As reported by Bakan et al. [30, 113] and Viswasnathan et al. [187], the strain tolerance of GZO coating is critical to thermal cycling lifetime of TBCs. Therefore, SPS was explored to apply the high strain tolerance GZO layers in this work.

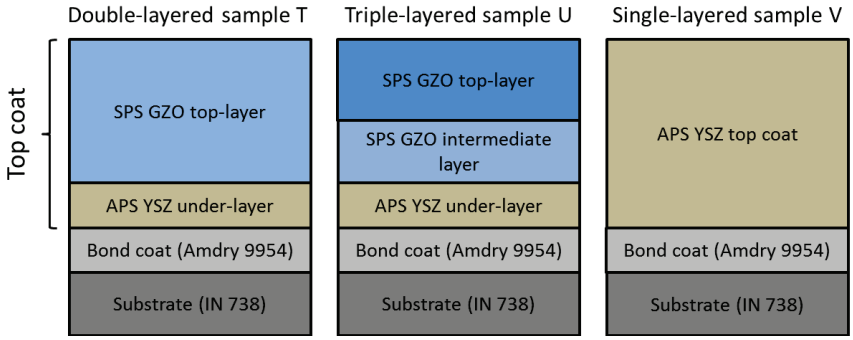

Fig. 7.1 Schematic diagram on the proposed architecture of sample T, U and V.

Two TBCs with multilayered top coats, as presented in Fig. 7.1, were designed in this work: one had a double-layered top coat named as sample T, the other one had a triple-layered top coat named as sample U. Double-layered top coat of sample T was composed of a lamellar structured APS YSZ under-layer and a columnar SPS GZO top-layer; the triple-layered top coat of sample U was composed of a lamellar structured APS YSZ under-layer, a columnar SPS GZO intermediate layer and a vertical cracked SPS GZO top-layer. As a reference for thermal cycling test under CMAS attack, a traditional TBC with single-layered APS YSZ top coat named as sample V was also produced.

In this work, the microstructures, thermal cycling behaviors, CMAS resistance of these multi-layered TBCs were investigated and compared with traditional single layered APS YSZ TBCs. The infiltration mechanism of CMAS under thermal gradient cycling condition was also investigated.

7.1 Microstructure of APS YSZ/SPS GZO Multi-Layer Coatings

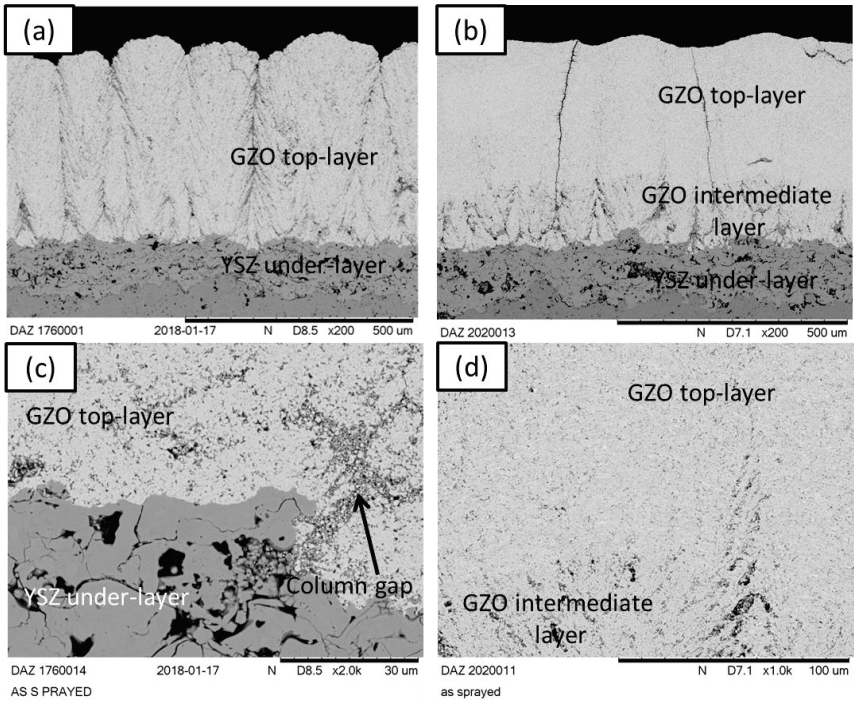

Fig. 7.2 As-sprayed microstructures of sample T (a) and sample U (b); Microstructure of sample T at the interface between YSZ under-layer and GZO top layer (c); microstructure of sample U at the interface of porous GZO intermediate layer and dense GZO top layer (d).

7 Results and Discussion Part IV

For spraying YSZ under-layer of sample T, U and top coat of sample V, a commercially available YSZ powder Metco 204 NS (Sulzer Metco, Wohlen, Switzerland) with internal number YSZ 412 M was used. For the GZO layer, a homemade GZO powder was used. The detailed information about the GZO powder and the corresponding suspension is given in section 3.2. The YSZ under-layer was deposited with a TriplexPro 210 plasma torch (Sulzer Metco, Wohlen, Switzerland) on as-sprayed bond coats (VPS, Amdry 9954). Detailed spraying parameters for the APS YSZ under-layer is presented in Table 5.1. And the spraying parameters for GZO top-layer are presented in the appendix.

The as-sprayed microstructures of sample T and U are presented in Fig. 7.2. Sample T (Fig. 7.2 (a)) had a double-layered top coat with a thin layer of ASP YSZ under-layer and columnar SPS GZO top-layer. The under-layer had a typical lamellar microstructure with a thickness of about 110 µm. Within this under-layer, a large number of pores and cracks with sizes tens of microns could be observed. Above this under-layer was a well-developed columnar structured SPS GZO layer with a thickness of about 490 µm. Columns directly grew on the top surface of the under-layer. YSZ under-layer provided asperities for the growth of columns. The formation of columns depends on suspension droplet trajectory just before the final impact. As the size of suspension droplets was smaller than 5 µm, they were easily redirected by the drag of plume in the boundary layer close to the substrate. Then, these droplets deposited at a shadow angle on asperities of under-layer leading to the formation of columns [132, 136, 156]. These columns with porous column gaps originating from under-layer/top-layer interface are expected to impart high strain tolerance to TBCs. Column density for sample T was about 7.6 /mm. Microstructure at the under-layer/top-layer interface is presented in Fig. 7.2 (c). Due to the high contrast of YSZ and GZO under SEM, the under-layer/top-layer interface could be clearly seen. In GZO top-layer, numerous micro-pores with sizes of several micrometers can be found. Column gaps were filled with a large amount of submicron spherical particles which were formed by solidification of droplets before impacting on the substrate. The top-layer perfectly fitted into rough APS under-layer surface without forming cracks at the interface. As no obvious cracks can be found at the interface, the bonding between these two layers was quite good. This could be attributed to the small size of SPS splats and good wetting between YSZ and GZO.

Sample U, as shown in Fig. 7.2 (b), had a triple-layered structure with an APS YSZ under-layer (~110 µm), a porous GZO intermediate layer (~150 µm) and a dense GZO top-layer (~300 µm). As a result of using the same spraying parameters, GZO intermediate layer had a similar porous columnar structure as top-layer of sample T. By shortening spraying distance from 100 mm to 70 mm, a dense vertical cracked top-layer was formed on top of the columnar intermediate layer. In this layer, vertical cracks originating from column gaps of the intermediate layer and penetrating through top-layer could be observed. The density for vertical cracks was about 3.3 /mm. With a high magnification image at the interface, as shown in Fig. 7.2 (d), an obvious porosity difference can be observed between these two GZO layers. In some areas, the shift from high porosity to low porosity was completed within 10 µm. However, at areas above the porous column gaps of the intermediate layer, this shift took more than 100 µm. Porous column gaps of intermediate layer were kept to

some extent in the dense top-layer. This porous part in dense top-layer was weak part providing easy paths for vertical cracks. Under tensile stress, vertical cracks initiated from this weak part and penetrate through the dense top-layer.

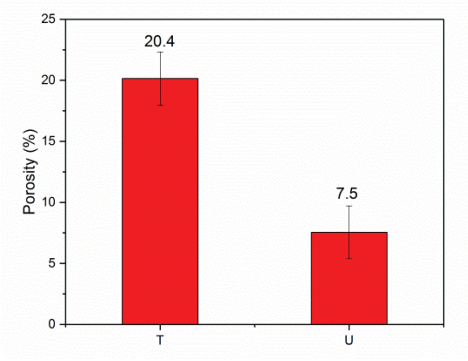

Fig. 7.3 Porosity of top layer for sample T and U.

The porosity of top layers for both samples was measured with image analysis. The results are presented in Fig. 7.3. The top layer of sample T had a porosity of 20.4%. As a result of shortening the spraying distance, top layer of sample U had a much lower porosity level of about 7.5%. The intermediate layer of sample U was sprayed with the same spraying parameters as that of the top layer of sample T. Thus the intermediate layer of sample U is expected to have a similar porosity level as the top layer of sample T.

7.3 Thermal Cycling Lifetime of APS YSZ/SPS GZO Multi-layer Coatings

After spraying, these two samples were subjected to thermal cycling tests. Thermal cycling testing conditions and thermal cycling lifetime of these two samples are listed in Table 7.2. To compare the thermal cycling performance of these two samples, the same testing conditions were used for both samples. The surface temperature was set to be 1400 ˚C, while the substrate temperature was set to be 1050 ˚C. As shown in Table 7.2, both samples had extremely long thermal cycling lifetime. Sample T had an average lifetime of about 1660 cycles, while sample U exhibited an average thermal cycling lifetime of about 1439 cycles. Even though sample U had a slight reduction on lifetime compared with sample T, it still had a significant longer lifetime than that of single layered APS YSZ TBCs [172]. Photographs and microstructures of thermal cycled samples are presented in Fig. 7.4. Both samples exhibited similar failure mode with a quite large failed area. At the exposed failed area, oxides scales with blue and gray color can be observed. This indicates the delamination occurred at the top coat/bond coat interface. In addition, some part of the cycled coating still attached to the substrate.

Table 7.2 Overview on thermal cycled sample T and U.

Sample	WDS No.	Thickness (μm)	Bond coat/top coat interface temperature (˚C)	Top coat surface temperature (˚C)	Top coat temperature gradient (˚C/μm)	Lifetime (cycles)
T	WDS 3902	~599	1080	1394	0.52	1598
	WDS 3903	~650	1081	1401	0.49	1722
U	WDS 3908	~590	1083	1397	0.53	1439

Microstructures of the thermal cycled sample T and U are presented in Fig. 7.4 (c) and (d), respectively. For both samples, the delamination of coating occurred at the bond coat/top coat interface. No delamination was observed at the GZO/YSZ layer interface. This indicates strong bonding between these two layers. This good bonding could be attributed to the good wetting between YSZ and GZO during spraying. In addition, diffusion between GZO and YSZ layer at high temperature might also improve the bonding. Similar observations were reported by Schlegel et al. and Schmitt et al. [33, 188]. For sample T, the expansion of column gaps penetrating through the GZO top layer could be clearly observed. This expansion could be attributed to high-temperature sintering which can lead to shrinkage of the coating. For sample U, only the expansion of vertical cracks could be observed. In addition, these vertical cracks extended into porous intermediate layer along column gaps and reached the APS under-layer. These expanded column gaps and vertical cracks probably played a critical role for the excellent thermal cycling performances of these multilayer coatings as they imparted high strain tolerance to TBCs.

Microstructures of bond coats after cycling are also presented in Fig. 7.4 (e) and (f). Overlaying MCrAlY bond coat consists of γ-Ni matrix with light color and β phase with dark color under SEM [60]. The β phase as an Al-rich phase provides Al for the formation of dense slow growing alumina TGO. However, after cycling, a total depletion of β phase was observed in both cycled bond coats. A large number of dispersed inclusions of alumina oxide and pores existed in the bond coat. Thick TGO with thickness of more than 7 μm could be found at the surface of bond coats. Except for Alumina, a large amount of gray contrasted oxides which typically are spinels comprising of Cr/Ni/Co oxides were also found at the top of bond coat [171]. These fast-growing spinel oxides are only formed when Al in bond coat is depleted below a critical level. Therefore this indicates Al depletion in both bond coats was very severe.

As introduced before, there are three main failure modes for APS TBCs. One is related to thermal mechanical properties of top coats. The second one is related to the TGO growth. The third one is Al depletion failure which is more related to the bond coat [171]. Generally, a lifetime potential of TBCs is limited by the bond coat Al depletion. APS coatings tested with burner rigs especially those with frequent cycles and harsh thermal loading, normally failed before a total depletion of β phase and have a depletion thickness about 30-40 μm [161]. In this work, both sample T and U exhibited an Al depletion failure mode. As complete depletion of β phase in bond coat, limit of bond coat was

reached for both samples. The formation of Alumina TGO as well as fast-growing oxides introduced additional stress and led to a final failure of TBCs [62].

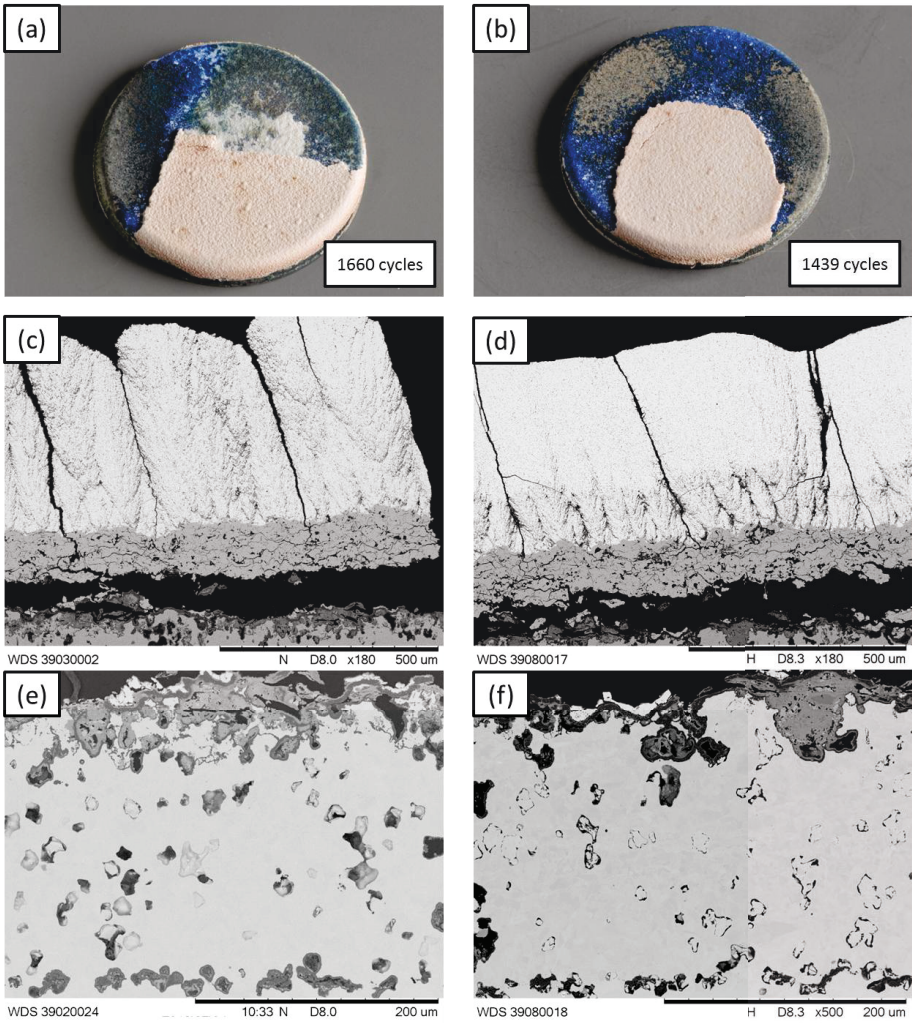

Fig. 7.4 Photographs of thermal cycled sample T (a) and U (b); SEM images on the cross-section of thermal cycled sample T (c) and U (d); SEM images of bond coats of sample T (e) and U (f).

The excellent thermal cycling performance for both samples might be attributed to their high strain tolerance of top coats and good sintering resistance of the GZO. At high temperature, due to the large thermal expansion misfit between the ceramic top coat and the metallic substrate, tensile stresses are introduced into the top coat. Column gaps and vertical cracks as a weak part of coating were able to open up under stresses. Thus thermal stress was reduced. The remaining thermal stress was assumed to be released by creep at high temperature. When the coating was cooled down to room temperature, the corresponding strain and stress were also reduced leading to high thermal cycling lifetime. With good sintering resistance, the decrease of porosity in the coating which reduces apparent elastic modulus was retarded. Thus the increase of thermal stress for cracks propagation in the top coat was retarded, as well [20, 60].

Column gaps and vertical cracks imparted high strain tolerance to TBCs. Thus thermal stress was reduced leading to long thermal cycling lifetime. As a result of good sintering resistance of GZO, the increase of apparent elastic modulus of top coat was retarded. Furthermore, the increase of thermal stress which is proportional to the elastic modulus was retarded, as well [20, 60]. The excellent thermal cycling performance of both samples might be attributed to the high strain tolerance structure and good sintering resistance of GZO.

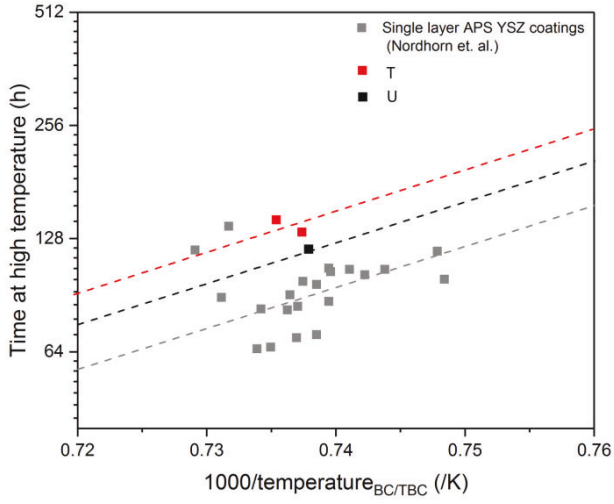

Fig. 7.5 Arrhenius plot of thermal cycling lifetime of multilayered APS/YSZ SPS/GZO sample T, U and single layered APS/YSZ samples.

As reported by Nordhorn et al. [172], lifetimes of APS coatings are very sensitive to bond coat temperature which determines the growth rate of TGO. In order to intuitively compare thermal cycling lifetime with APS coatings, the lifetime of samples are plotted in Arrhenius plot as shown in Fig. 7.5. A logarithm of high-temperature dwelling time was plotted as a function of inverse one-thousandth bond coat temperature. Due to similar bond coat chemical composition, the same slop of fitting line as that of APS TBC was assumed for sample T and U. Sample T and U have a significant improvement on thermal cycling lifetime compared with APS coatings. Even though sample U had a slight reduction on cycling performance compared with sample T, its cycling performance was still much better than APS coatings. The reduction of sample U could be attributed to the dense top layer and low vertical crack density, which reduces the strain tolerance of TBCs.

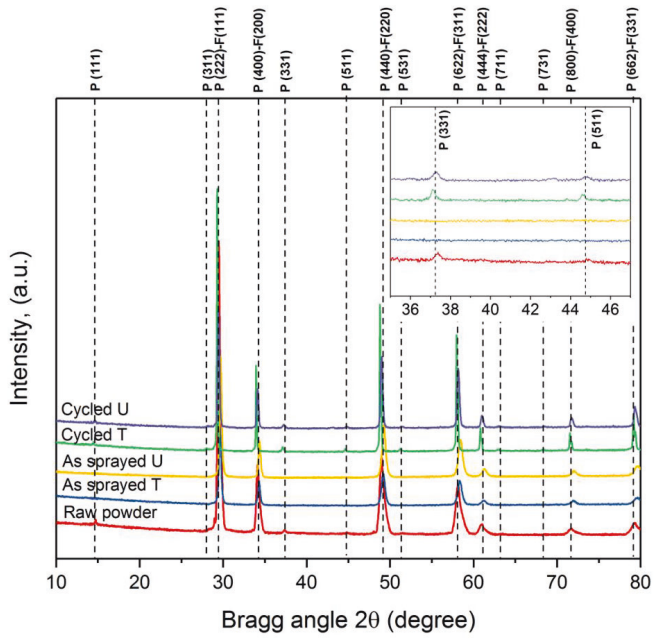

Fig.7.6 XRD pattern of raw powder, as-sprayed coatings and thermal cycled coatings.

XRD patterns of GZO raw powder, as-sprayed coatings and thermal cycled coatings are presented in Fig. 7.6. Fluorite phase was detected from all tested samples. By zooming in the Bragg angle range of 35˚ to 47˚, as presented in at the up-right corner in Fig. 7.6, Small peaks of pyrochlore phase can be found in GZO raw powder and thermal cycled sample T and U. Due to the overlapping of strongest peaks, the exact ratio of phases cannot be determined. In as sprayed samples, no pyrochlore phase can be found. During the SPS spraying process, molten GZO droplets impacted on cold substrates

(200-500 ˚C), they were cooled down very quickly and solidified into fluorite phase. With further cooling (below 1530 ˚C), Fluorite phase should have transformed into equilibrium pyrochlore phase. However, this cooling process was too fast for atoms to rearrange positions. Thus this phase transformation was kinetically suppressed. Finally, a metastable pyrochlore phase was kept in the as-sprayed coating until room temperature. During thermal cycling test, the surface temperature of the tested sample was up to 1400 ˚C. At such high temperature, fluorite phase undergoes phase transformation into an equilibrium pyrochlore phase [108, 189]. After a long time of cycling, more than 100 hours, pyrochlore phase can be detected in thermal cycled coating again. Although there was phase transformation during cycling, the phase transformation from a fluorite phase to a pyrochlore phase essentially has very small volume and thermal conductivity changes [190]. It is expected that this phase transformation has no harm to the thermal cycling performance of coatings [108].

7.4 Thermal Cycling Performance of APS YSZ/SPS GZO Multi-layer Coatings under CMAS Attack

CMAS resistance for both sample T and U was also tested. To mimic realistic service environment of turbine blades under CMAS attack, a CMAS burner rig test was carried out on both samples. The testing conditions and thermal cycled results under CMAS attack are presented in Table 7.3. To make a comparison with APS coatings, a standard APS YSZ TBCs named as sample V was produced with spraying parameter shown in Table 5.1 as a reference sample. Detailed setup about the CMAS burner rig facility is accessible in ref. [20, 152]. In addition, the chemical composition of CMAS solution was presented in Table 3.4 [20]. All these three samples were tested with the same testing conditions which were given in Table 7.3.

Compared with cycling results without CMAS, the lifetime of sample T and U was greatly reduced. The reference sample V had a lifetime of 163 cycles. Sample T had a lifetime about 115 cycles which were slightly shorter than the reference sample V. Sample U had an excellent lifetime about 308 cycles which were almost double of the reference sample V.

Table 7.3 Overview on thermal cycled sample T, U and V under CMAS attack.

Sample	WDS No.	Thickness (µm)	Bond coat/top coat interface temperature (˚C)	Top coat surface temperature (˚C)	Top coat temperature gradient (˚C/µm)	Lifetime (cycles)	Feeding rate of CMAS solution (ml/min)
T	WDS 3904	~620	1040	1285	0.36	115	1.2
U	WDS 3906	~621	1028	1268	0.35	308	1.2
V	WDS 3893	~586	1024	1279	0.44	163	1.2

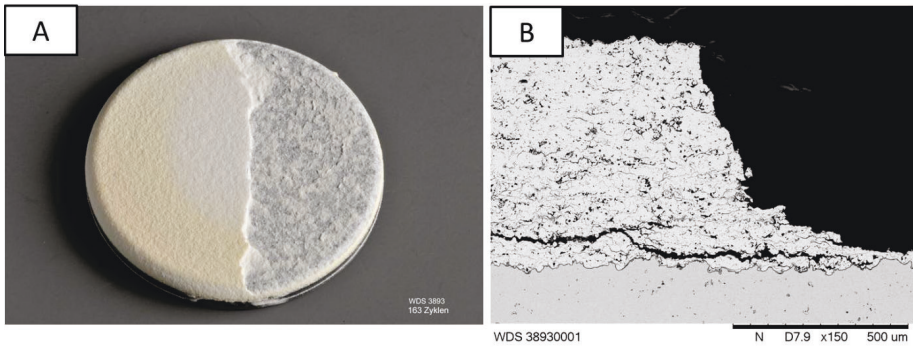

Fig. 7.7 Photograph (A) and SEM image on cross-section of the microstructure (B) of failed sample V under CMAS attack.

Firstly, the failure modes of reference sample V were investigated. Photograph and SEM image of the failed sample V is presented in Fig. 7.7. The failed sample V had a quite large failure area with a large amount of white YSZ residuals attaching on the substrate. In Fig. 7.7 (b), the delamination happened within the top coat and near to the bond coat. It seems the thermal misfit between the top coat and substrate upon cooling is the driving force for the delamination. Due to the infiltration of CMAS, sample V was stiffened with an increase of elastic modulus and reduction in strain tolerance. Upon cooling, a higher thermal stress level was produced leading to an early failure of TBCs [80, 87].

To investigate the failure modes of sample T and U under CMAS attack, photographs and SEM on failed samples were presented in Fig. 7.8. From the photos of failed sample T and U, as shown in Fig. 7.8 (a) and (b), pitted surface with white shrouds can be seen. The white shrouds are supposed to be CMAS solids. As a result of CMAS injection process, distribution of CMAS on the sample surface had a radial gradient. This led to different damage degrees on the sample surface. At the center of CMAS covered area of both samples, they had deeper pits which imply heavier damage; at the edge of CMAS covered area, the damage was reduced. Thus observations on the CMAS covered area at different positions were made. At the center of sample T, as shown in Fig. 7.8 (c), the external part of coating which was infiltrated by CMAS had already peeled off. Similar peeling was also observed from sample U as shown in Fig. 7.8 (d). Due to the peeling of the infiltrated coating, the accurate maximum CMAS infiltrated depth for both samples was not available. For sample T, except for delamination of CMAS infiltrated layer, a large amount of horizontal cracks at a deeper level were observed. These cracks initiated from column gaps and propagated horizontally into the coating. Column gaps here seems to work as channel cracks which were illustrated by Krämer et al. [88].

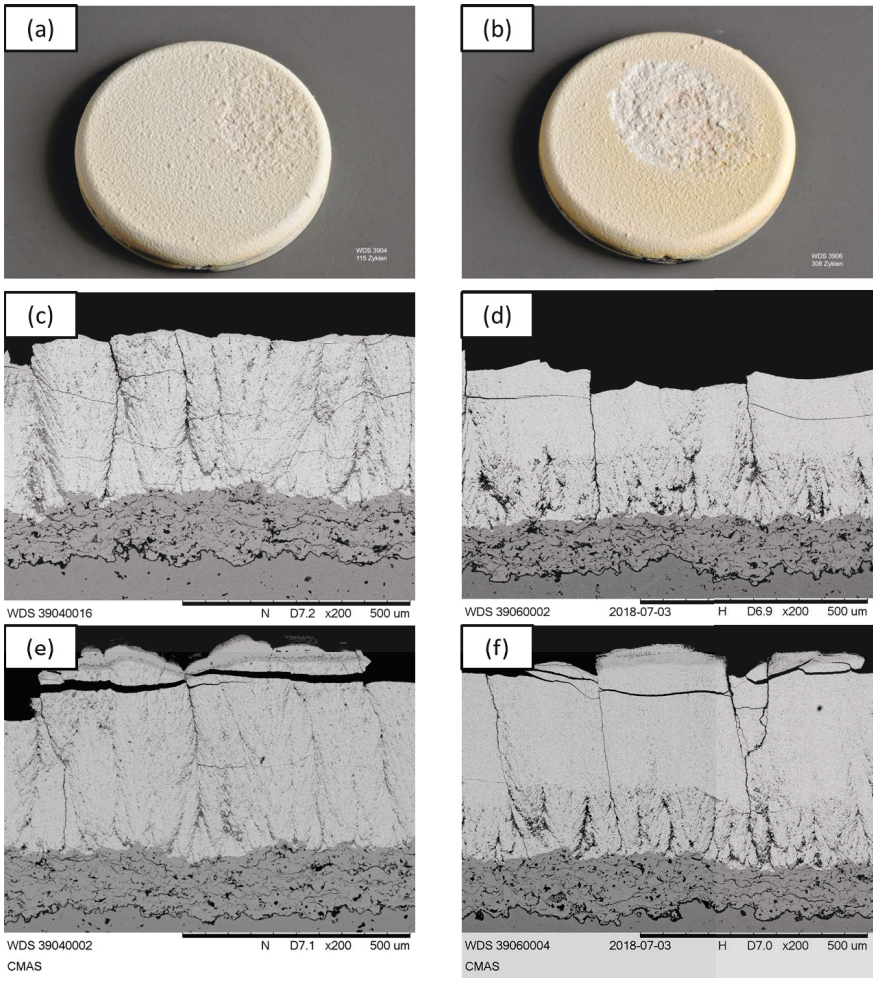

Fig. 7.8 Photograph of CMAS tested sample T (a) and U (b); failed microstructure of sample T (c) and U (d) at the center of CMAS covered area; failed microstructure of sample T (e) and U (f) at the edge of the CMAS covered area.

Even though, horizontal cracks at a deeper level were also found in sample U, as shown in Fig. 7.8 (d); the number of cracks was greatly reduced after an even longer testing time. At the edge of the CMAS covered area for both samples, a CMAS infiltration zone with a thickness of about 50 µm was seen. Even though, delamination of CMAS infiltration zone occurred. No horizontal cracks at a deeper level were found for both samples. As all delamination happened near to the surface instead

of vicinity of bond coat, it indicates that the spallation is cold shock introduced [80, 87, 88, 91, 95]. During CMAS cycling test, after high-temperature phase, the samples were extensively cooled with compressive air from both sides. The surface temperature of the coating was cooled down very quickly, while the bond coat temperature reduces slowly. As the surface was cooled faster than the bond coat, a thermal stress developed from self-constrain of coating was introduced into the coating [80]. It seems sample U was more resistant to this cold shock and the horizontal cracks at the deeper level were suppressed. To get a better insight on reasons of sample U's better performance under CMAS attack, mechanical properties of both samples were investigated with indentation tests. The obtained elastic modulus and fracture toughness for the top layer of both samples are presented in Fig. 7.9.

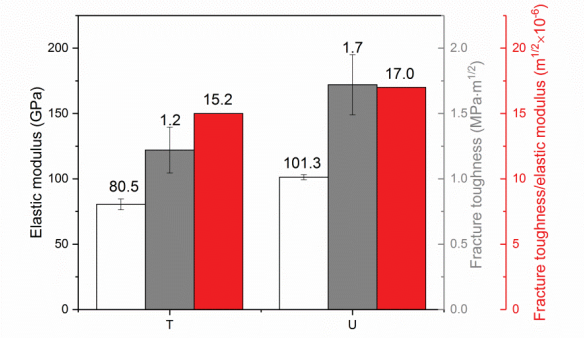

Fig. 7.9 Elastic modulus, fracture toughness, a ratio of fracture toughness to elastic modulus of sample T and U.

Top layer of sample T had a lower elastic modulus (80.5 ± 4.2 GPa) and a lower fracture toughness (1.2 ± 0.2 MPa·m1/2). As a result of low density as shown in Fig. 7.3, sample U had a higher elastic modulus (101.3 ± 2.0 GPa) and a higher fracture toughness (1.7 ± 0.2 MPa·m1/2). Even though sample U had higher fracture toughness, the relatively higher elastic modulus could introduce a higher thermal stress into the coating. Generally, the crack growth rate is proportional to the ratio of stress intensity factor to the critical stress intensity factor (fracture toughness) with a rather high exponent n, as shown in the following equation:

$$\frac{dc}{dt} = A\left(\frac{\mathrm{K_I}}{\mathrm{K_{IC}}}\right)^{\mathrm{n}} \tag{7.1}$$

where, $\frac{\mathrm{dc}}{\mathrm{dt}}$ is the crack growth rate; $\mathrm{K_I}$ is the stress intensity factor; $\mathrm{K_{IC}}$ is the fracture toughness of coating; A is a constant, n is a value related to the nature of the material.

The stress intensity factor $\mathrm{K_I}$ can be estimated by:

$$\mathrm{K_I} = \mathrm{Y}\sigma\sqrt{\mathrm{c}} \tag{7.2}$$

where Y is the geometry factor of cracks; σ is the cold shock stress level; c is the crack length. To simplify the estimation, same geometry factor and crack length are assumed for sample A and B. As both samples A and B were tested with the same conditions, the same temperature trajectory was also assumed for both samples. According to the cold shock model built by Levi et al. [80], stress introduced by cold shock is proportional to the elastic modulus of the coating. Therefore, cold shock stress level is only determined by the elastic modulus of the coating. By introducing equation (7.2) into equation (7.3) and taking reciprocal on both sides of equation (7.3), the resistance of coating to cold shock introduced cracks $\frac{dt}{dc}$ can be expressed as following:

$$\frac{dt}{dc} = \frac{1}{A}\left(\frac{K_{Ic}}{Y\sigma\sqrt{c}}\right)^n \propto \left(\frac{K_{IC}}{E_c}\right)^n \tag{7.3}$$

where E_c is the elastic modulus of coating. It can be easily get that $\frac{K_{IC}}{E_c}$ would be a simplified and reasonable index to evaluate the resistance of coating to cold shock introduced cracks. The $\frac{K_{IC}}{E_c}$ value of both sample T and U is also presented in Fig. 7.9. Sample U had a higher $\frac{K_{IC}}{E_c}$ with a value of 17×10^{-6} $m^{1/2}$, while sample T had a value of 15×10^{-6} $m^{1/2}$. Even though the elastic modulus of sample U was increased by shortening spraying distance; the fracture toughness of it was increased more. Probably this is the mechanical reason why sample U was more resistant to cold shock and exhibited a longer lifetime under CMAS attack than sample T.

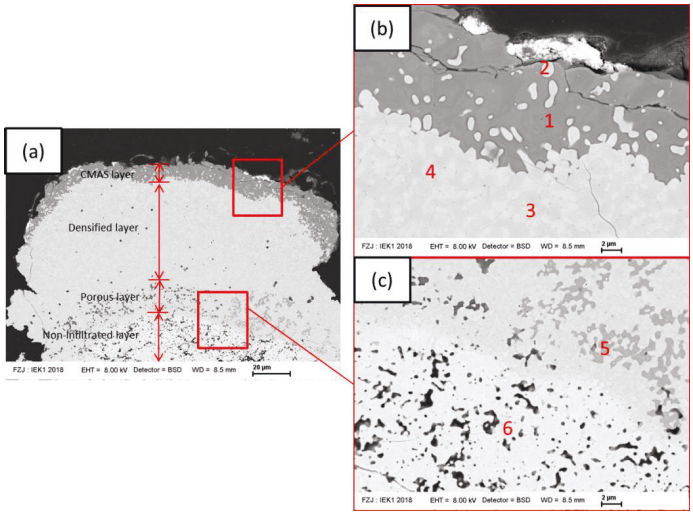

Fig. 7.10 SEM images of CMAS infiltration area (a), SEM images at interface of CMAS and CMAS infiltrated area (b), SEM image at interface of CMAS infiltrated area and GZO coating (c).

At the un-failed area, a thin layer of CMAS infiltrated zone with a thickness of about 50 µm was observed from both sample T and U, as shown in Fig. 7.10 (a). Generally, this CMAS infiltrated zone could be divided into three regions as a CMAS layer, a densified layer and a porous layer. The CMAS layer with a dark contrast had a thickness of 10-20 µm. A few of isolated spheroidized grains randomly distributed in this CMAS layer. Beneath this CMAS layer was a thick densified layer with a thickness of more than 40 µm. Although some isolated pores existed in this layer, it was an almost fully densified layer. At the bottom of the CMAS infiltrated zone, a porous layer with a thickness of about 20 µm was found. As a result of sintering, large amount of coarsening pores could be found in this layer. Interesting thing is in some area, these pores were filled with a dark contrast phase. Beneath this layer is non-infiltrated porous GZO layer. To get a better insight on the microstructure of infiltrated zone, observation with a higher magnification were made at the interface of these layers as shown in Fig. 7.10 (b) and (c). To investigate the chemical composition of different phases, EDS was performed on points marked with numbers as shown in Fig. 7.10 (b) and (c). Limited by resolution of EDS, a precise quantitative chemical composition was not available; but with the EDS results, a better insight on GZO decomposition and CMAS transportation mechanism was possible.

EDS results on each specific point are presented in Fig. 7.11. Point 1 was made in the CMAS layer. Elements of CMAS precursor, such as Si, Al, Mg and Ca, were detected. The limited amount of Fe in precursor was undetectable in this CMAS layer [95]. Except for the CMAS elements, a considerable amount of Gd and Zr were also detected. This implies GZO dissolved in CMAS during cycling. Points 2 was made on an isolated light contrast phase in the CMAS layer. The intensive Zr peak implies its main composition was ZrO_2. A limited amount of Ca, Gd and Si were detected from it, as well. According to Mechnich's research [86], this might be Ca/Gd co-stabilized ZrO_2. These ZrO_2 phase has a spherical morphology. Some ZrO_2 phase can even be found at the area close to top surface CMAS layer. As the original profile of GZO coating was unable to be determined, it is impossible to judge whether these ZrO_2 were formed by the re-precipitation or they were the residuals of the dissolved GZO [86]. With the BSE image shown in Fig. 7.10, it could be clearly observed that the densified layer contains two interlocking phases with different grey scales. Thus EDS point tests were carried on points 3 and 4. Point 3 was made on the darker gray scale phase, while point 4 was made on the lighter gray scale phase. CMAS elements such as Ca, Si, Al and GZO elements such as Gd, Zr were detected from both points. However, they exhibited different concentration in these two phases. Point 3 had a relatively higher concentration on Gd, Si and Ga; while point 4 had a higher concentration on Zr. These two phases clearly were decomposition products of GZO under CMAS infiltration. It can be deduced the lighter phase was ZrO_2, while the darker phase was an apatite $Ca_2Gd_8(SiO_4)_6O_2$ phase [84, 86]. Gd_2O_3 has a higher solubility than ZrO_2 in CMAS. This led to ex-solution of Gd_2O_3 from GZO, finally leads to forming ZrO_2 phase. As the enrichment of Gd_2O_3 in the CMAS, a new apatite phase $Ca_2Gd_8(SiO_4)_6O_2$ was formed. Due to the infiltration of CMAS, sintering of GZO was accelerated leading to fast densification of coating. Perhaps the CMAS can work as a medium of liquid sintering and accelerated sintering process of GZO coating [95]. As a result of densification of coating, infiltration of CMAS was slowed down. The third layer was a porous layer. Although this layer was infiltrated by CMAS, it was not fully densified. A large number of coarsened

pores existed in this area. Some pores were fully or partly filled with a dark contrasted solid phase, as shown in Fig. 7.10 (c). To confirm the chemical composition of this solid phase, a EDS test was made on point 5. It revealed that this phase mainly contained Gd, Zr, Si, Ca. In addition, limited amount of Al, Mg and Fe were also detected. It can be speculated that this dark phase is an infiltrated CMAS phase. Due to the dissolution of GZO, Gd and Zr were detected from this phase. As Si, Ca were consumed by forming apatite phase, the relative concentrations of Al, Mg, Fe in CMAS increased. Thus the undetectable Fe in the CMAS layer was detected here. At bottom of this porous layer, the infiltration front of CMAS can be clearly seen. Beneath this front, as seen in Fig. 7.11, no CMAS elements can be found from point 6.

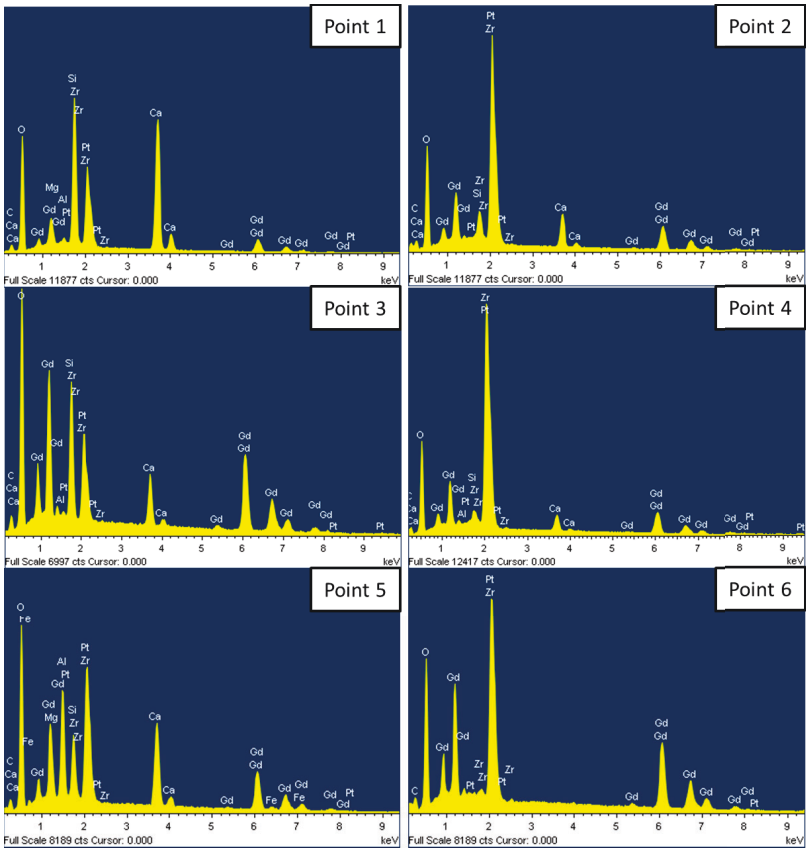

Fig. 7.11 EDS results corresponding to points marked in Fig. 7.10 (b) and (c).

The infiltration of CMAS under thermal gradient cycling condition was a very complex process. Due to the periodic heating and cooling, CMAS was periodically melted and solidified. At the high-temperature heating phase, GZO was continuously dissolved into CMAS. Upon infiltrated by CMAS, Gd was ex-soluted from GZO forming Zr based oxide. The ex-soluted Gd reacted with Ca and Si in CMAS to form new apatite phase $Ca_2Gd_8(SiO_4)_6O_2$. Due to the CMAS infiltration, a fast densification of CMAS infiltrated area was observed. Due to fast densification of the CMAS infiltrated area, further CMAS infiltration was retarded leading to a thinner CMAS infiltrated area.

7.5 Erosion Resistance of SPS GZO/APS YSZ Multi-layer Coatings

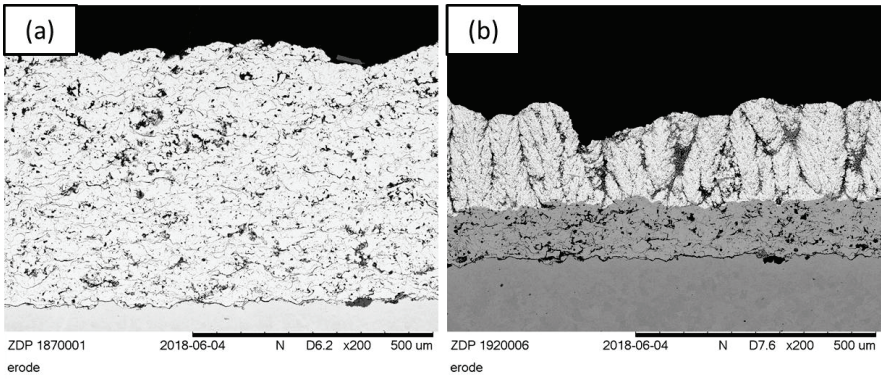

Fig. 7.12 Microstructure of eroded sample V (a) and T (b).

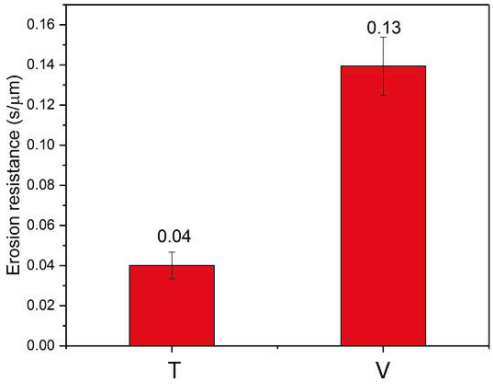

Fig.7.13 Erosion resistance of sample T and V.

Erosion resistance of sample T was also tested with a sand blasting erosion test. Standard single layered APS coating sample V was also tested as a reference. The cross-section microstructures of eroded samples are presented in Fig. 7.12. Both coatings exhibited similar failure mode. The damage

mechanism is related to single or multiple splat removal through crack propagation along the boundaries of single splat or cluster of splats. From cross-section of failed samples, it seems sample T was eroded much faster than sample V. To evaluate this difference, equation 3.14 was used to evaluate the erosion resistance of both samples.

Erosion resistances of both samples are presented in Fig. 7.13. Obviously, sample T was not as resistant to erosion as sample V. Sample T had a value of 0.04 s/µm while sample V had a value of 0.13 s/µm. This probably is related to the lower fracture toughness and the higher porosity of sample T [70].

8 Summary and Concluding Remarks

Suspension plasma spraying is an attractive and advanced thermal spraying technology especially for depositing thermal barrier coatings. In this thesis, potentials of SPS TBCs were explored. This thesis mainly contains four parts: (I) relations of spraying parameters, microstructures, mechanical properties and thermal cycling lifetime of coatings; (II) new approaches to improve thermal cycling lifetime of coatings; (III) sintering behaviors of columnar thermal barrier coatings; (IV) thermal cycling performances of APS/YSZ SPS/GZO multilayered coatings.

In the first part, effects of spraying conditions on microstructures and deposition efficiency were investigated. Among the spraying parameters, bond coat roughness and spraying distance played a dominant role on microstructure of top coats. Both increasing spraying distance and reducing bond coat roughness increased the column density of coating. Lowering solid content in suspension promoted the growth of columns. In addition, bond coat roughness, spraying distance and gun power had a significant effect on the porosity of top coats. Increasing bond coat roughness, spraying distance, lowering gun power, as well as solid content in suspension could enhance the porosity level of coatings. Compared with radial injection, SPS with axial injection had a higher deposition efficiency. The highest deposition efficiency achieved in this work was about 60.7 % which is similar to that of APS. The deposition efficiency was mainly influenced by the spraying distance. With increase of it, the deposition efficiency dropped largely.

YSZ coatings deposited on as-sprayed bond coats with a 5 wt.% solid content suspension appeared to have a well-developed columnar structure. Columns growing on asperities of bond coat were separated by porous column gaps. Based on the preliminary results, well developed columnar structured coatings with different porosity level were thermal cycled in a gas burner rig facility. In addition, mechanical properties of these coatings, such as hardness, elastic modulus as well as fracture toughness were measured. It was found that fracture toughness of coatings had a positive correlation with thermal cycling lifetime. Thus a coating with even higher density and higher fracture toughness were produced by increasing deposition temperature. The results turned out that further increasing fracture toughness of coating can not increase lifetime of coatings. To get a better insight into the relationship of lifetime and mechanical properties of coatings, a simplified model was built. It revealed that not only fracture toughness, but also elastic modulus affected thermal cycling lifetime of the coatings. By increasing density, both fracture toughness and elastic modulus were increased. Higher elastic modulus introduced higher thermal stress leading to a reduced thermal cycling lifetime.

In the second part, a failure mechanism of SPS coatings was promoted. Due to the highly undulation nature of the bond coat, radial thermal stresses were introduced into the vicinity of top coat/bond coat interface. For as-sprayed coating, a tensile stress existed on the top of asperities while a compressive stress existed in the valley. Due to the deposition nature of the columns in SPS, the columns always grow on asperities of bond coat with porous column gaps originating from valleys.

This led to a reduction of compressive stress in valley and make cracks be able to penetrate the valley areas without thickening of TGO. This might explain the premature failure of coating in part I. According to this failure mechanism, SPS TBCs with two innovative architecture designs were deposited. One was a double-layered design. Before depositing columnar SPS coating, a thin layer of APS was deposited. With this design, compressive stress at the valley could be kept and also it could take advantage of higher strain tolerance of columnar SPS top coats. Thermal cycling results revealed that this design was very successful. With this design, thermal cycling performance even better than APS coatings was obtained.

The other design was to deposit top coats on grinded bond coats. As the radial thermal stress level is proportional to the ratio of asperities amplitude to the period length A/L, lowering roughness of bond coat by grinding is able to reduce the radial thermal stress. Similar with splat overlaying APS coatings, bonding of SPS coating was assumed to derive from mechanical bonding. Thus the grinded bond coat was pre-oxidized to form a thin layer of TGO. With this thin TGO layer, the bonding between top coat and bond coat was strong enough to survive from the harsh thermal cycling tests. Compared with SPS coatings deposited with the same spraying parameters but on as-sprayed bond coat, lifetime of SPS coatings deposited on grinded bond coat was greatly improved. It seems this design was also worked. But mechanical properties of this coating were not optimized. With a further increase of fracture toughness, lifetime of such coating might be further increased.

In part III, the sintering behavior of columnar TBCs deposited with SPS was investigated. Columnar structured TBCs were deposited with 5 mol.% YSZ. After spraying, samples were isothermally annealed at 1373 K for 1 h, 3 h, 10 h and 50 h, respectively. Microstructures and mechanical properties (i.e., hardness, elastic modulus and indentation based fracture toughness) of coatings were investigated as a function of annealing time. It was found that annealing resulted in healing of micro pores, coarsening of pores and a growth of the domain size, accompanying with a decrease of porosity within columns. These modifications on microstructures lead to change of the mechanical properties, such as increase of hardness, elastic modulus and fracture toughness of the coatings.

In addition, significant fracture toughness anisotropy was observed in the case of as-sprayed SPS coatings. The as-sprayed coatings showed a higher fracture toughness in plane and a lower fracture toughness out of plane. The anisotropy in fracture toughness can be attributed to the textured microstructure and residual stress in coating. In addition, it was also found that short time pre-annealing could improve the thermal cycling lifetime SPS coatings. This might be related to the decrease of geometry factor due to reduction of defect sizes.

In the last part, the performance of multilayer APS YSZ/SPS GZO coatings was investigated. Two kinds of GZO/YSZ multilayer coatings were designed. One was APS YSZ/SPS GZO double-layered coatings with a thin lamellar APS YSZ under-layer and a porous columnar structured SPS GZO top layer. The other one was an APS YSZ/SPS GZO triple-layered coating with a thin lamellar APS YSZ under-layer, a porous columnar SPS GZO intermediate layer and a dense vertical cracked SPS GZO top layer. Both coatings showed excellent thermal cycling performance. Growth of TGO, especially

fast growing spinel phase, led to the final failure of both coatings. The excellent cycling performances for both coatings can be attributed to high strain tolerance and good sintering resistance of both coatings. Performances of both coatings under CMAS attack were also tested in a burner rig test. Both coatings failed due to cold shock. The triple layer coating had an excellent lifetime (308 cycles) under CMAS attack. Mechanic properties of the as sprayed top layer for both samples were measured with indentation tests. The excellent performance of the triple layered coating under CMAS attack could be attributed to its high ratio of the fracture toughness to elastic modulus which means it was more resistant to cold shock. Interactions of CMAS and TBCs under cycling were also investigated. The CMAS infiltration process was quite complex. It contained melting and re-solidification of CMAS, dissolution of GZO into CMAS, exsolution of Gd from GZO, forming new apatite phase, densification of infiltrated zone, chemical composition change of CMAS, accumulation of CMAS in deeper porous area.

In summary, SPS is a very promising process for fabricating TBCs. Excellent cycling performance of SPS TBCs was obtained. However, further study on failure mechanism of SPS coatings need to be done.

Reference

[1] M. Peters, C. Leyens, U. Schulz, W.A. Kaysser, Advanced Engineering Materials, 3 (2001) 193-204.
[2] D.R. Clarke, M. Oechsner, N.P. Padture, MRS bulletin, 37 (2012) 891-898.
[3] R. Vassen, A. Stuke, D. Stöver, Journal of thermal spray technology, 18 (2009) 181-186.
[4] J. Nicholls, MRS bulletin, 28 (2003) 659-670.
[5] H.-J. Rätzer-Scheibe, U. Schulz, Surface and coatings technology, 201 (2007) 7880-7888.
[6] S. Sampath, U. Schulz, M.O. Jarligo, S. Kuroda, MRS bulletin, 37 (2012) 903-910.
[7] N.P. Padture, M. Gell, E.H. Jordan, Science, 296 (2002) 280-284.
[8] R. Vassen, M.O. Jarligo, T. Steinke, D.E. Mack, D. Stover, Surface & Coatings Technology, 205 (2010) 938-942.
[9] G. Mauer, M.O. Jarligo, D.E. Mack, R. Vaßen, Journal of thermal spray technology, 22 (2013) 646-658.
[10] N.P. Padture, M. Gell, E.H. Jordan, Science, 296 (2002) 280-284.
[11] R. Vaßen, H. Kaßner, G. Mauer, D. Stöver, Journal of thermal spray technology, 19 (2010) 219-225.
[12] D. Zhou, O. Guillon, R. Vaßen, Coatings, 7 (2017) 120.
[13] A. Guignard, G. Mauer, R. Vaßen, D. Stöver, Journal of thermal spray technology, 21 (2012) 416-424.
[14] M. Marr, D. Waldbillig, O. Kesler, Journal of thermal spray technology, 22 (2013) 116-124.
[15] S. Mahade, R. Li, N. Curry, S. Björklund, N. Markocsan, P. Nylén, International Journal of Applied Ceramic Technology, 13 (2016) 443-450.
[16] P. Fauchais, M. Vardelle, S. Goutier, A. Vardelle, Plasma Chemistry and Plasma Processing, 35 (2014) 511-525.
[17] W. Fan, Y. Bai, Ceramics International, (2016).
[18] P. Fauchais, G. Montavon, Journal of thermal spray technology, 19 (2010) 226-239.
[19] A. Guignard, Development of thermal spray processes with liquid feedstocks, Forschungszentrum Jülich, 2012.
[20] E. Bakan, R. Vaßen, Journal of Thermal Spray Technology, 26 (2017) 992-1010.

[21] G. Dwivedi, V. Viswanathan, S. Sampath, A. Shyam, E. Lara‐Curzio, Journal of the American Ceramic Society, 97 (2014) 2736-2744.
[22] R. Vaßen, N. Czech, W. Mallener, W. Stamm, D. Stöver, Surface and Coatings Technology, 141 (2001) 135-140.
[23] X.Q. Cao, R. Vassen, D. Stoever, Journal of the European Ceramic Society, 24 (2004) 1-10.
[24] W. Pan, S.R. Phillpot, C. Wan, A. Chernatynskiy, Z. Qu, MRS bulletin, 37 (2012) 917-922.
[25] E. Bakan, in, Werkstoffsynthese und Herstellungsverfahren, 2015.
[26] C. Wang, (2006).
[27] R. Vassen, X.Q. Cao, F. Tietz, D. Basu, D. Stover, Journal of the American Ceramic Society, 83 (2000) 2023-2028.
[28] R. Vassen, F. Traeger, D. Stöver, International Journal of Applied Ceramic Technology, 1 (2004) 351-361.
[29] R. Leckie, S. Krämer, M. Rühle, C. Levi, Acta Materialia, 53 (2005) 3281-3292.
[30] E. Bakan, D.E. Mack, G. Mauer, R. Vassen, Journal of the American Ceramic Society, 97 (2014) 4045-4051.
[31] X. Cao, R. Vassen, F. Tietz, D. Stoever, Journal of the European ceramic society, 26 (2006) 247-251.
[32] K. Bobzin, N. Bagcivan, T. Brögelmann, B. Yildirim, Surface and Coatings Technology, 237 (2013) 56-64.
[33] M.P. Schmitt, A.K. Rai, R. Bhattacharya, D. Zhu, D.E. Wolfe, Surface and Coatings Technology, 251 (2014) 56-63.
[34] W. Commons, in, https://upload.wikimedia.org/wikipedia/commons/4/4c/Jet_engine.svg.
[35] L.S. Langston, Mechanical Engineering, 133 (2011) 30.
[36] u.s.D.o. Transportation, in, https://www.faa.gov/news/press_releases/news_story.cfm?newsId=12439, 2011.
[37] commons.wikimedia, in, CC BY-SA 3.0, https://commons.wikimedia.org/w/index.php?curid=835176.
[38] F. Yin, A.G. Rao, The Aeronautical Journal, 121 (2017) 1605-1626.
[39] T.K. Ibrahim, M. Rahman, International journal of energy engineering, 2 (2012) 9-14.
[40] J.-C. Han, S. Dutta, S. Ekkad, Gas turbine heat transfer and cooling technology, CRC Press, 2012.
[41] H. Xu, H. Guo, Thermal barrier coatings, Elsevier, 2011.

[42] S. Kumar, S. Kant, N. Suri, (2016).
[43] R. Rajendran, Engineering Failure Analysis, 26 (2012) 355-369.
[44] S. Stecura, Thin Solid Films, 150 (1987) 15-40.
[45] T.E. Strangman, Thin Solid Films, 127 (1985) 93-106.
[46] O.A. Ojo, N.L. Richards, M.C. Chaturvedi, Scripta Materialia, 50 (2004) 641-646.
[47] D. Furrer, H. Fecht, Jom, 51 (1999) 14-17.
[48] T.M. Pollock, S. Tin, Journal of propulsion and power, 22 (2006) 361-374.
[49] P. Caron, T. Khan, Aerospace Science and Technology, 3 (1999) 513-523.
[50] H.K.D.H. Bhadeshia, in, https://www.phase-trans.msm.cam.ac.uk/2003/Superalloys/superalloys.html.
[51] N. institute, in, https://www.nickelinstitute.org/en/TechnicalLibrary/INCO%20Series/0497_IN738_Alloy_PreliminaryData.aspx.
[52] T. Pollock, D. Lipkin, K. Hemker, MRS bulletin, 37 (2012) 923-931.
[53] J. Nicholls, N.J. Simms, W. Chan, H. Evans, Surface and Coatings Technology, 149 (2002) 236-244.
[54] J.-H. Park, T. Sudarshan, Chemical vapor deposition, ASM international, 2001.
[55] C. Lima, J. Guilemany, Surface and Coatings Technology, 201 (2007) 4694-4701.
[56] P. Richer, M. Yandouzi, L. Beauvais, B. Jodoin, Surface and Coatings Technology, 204 (2010) 3962-3974.
[57] G. Mauer, R. Vaßen, D. Stöver, Journal of thermal spray technology, 19 (2010) 495-501.
[58] A. Feuerstein, J. Knapp, T. Taylor, A. Ashary, A. Bolcavage, N. Hitchman, Journal of Thermal Spray Technology, 17 (2008) 199-213.
[59] I. Keller, D. Naumenko, W.J. Quadakkers, R. Vaßen, L. Singheiser, Surface and Coatings Technology, 215 (2013) 24-29.
[60] D. Naumenko, V. Shemet, L. Singheiser, W.J. Quadakkers, Journal of Materials Science, 44 (2009) 1687-1703.
[61] P. Niranatlumpong, C. Ponton, H. Evans, Oxidation of Metals, 53 (2000) 241-258.
[62] A. Rabiei, A.G. Evans, Acta Materialia, 48 (2000) 3963-3976.
[63] R.H. Hannink, P.M. Kelly, B.C. Muddle, Journal of the American Ceramic Society, 83 (2000) 461-487.

[64] S. Stecura, Thin Solid Films, 73 (1980) 481-489.
[65] D. Hasselman, L.F. Johnson, L.D. Bentsen, R. SYED, H.L. LEE, M.V. SWAIN, Am. Ceram. Soc. Bull, 66 (1987) 799-806.
[66] J. Chevalier, L. Gremillard, A.V. Virkar, D.R. Clarke, Journal of the American Ceramic Society, 92 (2009) 1901-1920.
[67] C. Viazzi, J.-P. Bonino, F. Ansart, A. Barnabé, Journal of Alloys and Compounds, 452 (2008) 377-383.
[68] K. Muraleedharan, J. Subrahmanyam, S.B. Bhaduri, Journal of the American Ceramic Society, 71 (1988).
[69] R. Vaßten, G. Kerkhoff, M. Ahrens, D. Stöver, Ceramic Materials and Components for Engines, (2001) 305-310.
[70] F. Cernuschi, L. Lorenzoni, S. Capelli, C. Guardamagna, M. Karger, R. Vaßen, K. von Niessen, N. Markocsan, J. Menuey, C. Giolli, Wear, 271 (2011) 2909-2918.
[71] J.R. Nicholls, M.J. Deakin, D.S. Rickerby, Wear, 233-235 (1999) 352-361.
[72] H. Eaton, R. Novak, Surface and Coatings Technology, 30 (1987) 41-50.
[73] J. Nicholls, M. Deakin, D. Rickerby, Wear, 233 (1999) 352-361.
[74] C.-J. Li, G.-J. Yang, A. Ohmori, Wear, 260 (2006) 1166-1172.
[75] R.L. Jones, Journal of Thermal Spray Technology, 6 (1997) 77-84.
[76] S.Y. Park, J.H. Kim, M.C. Kim, H.S. Song, C.G. Park, Surface and Coatings Technology, 190 (2005) 357-365.
[77] C. Batista, A. Portinha, R. Ribeiro, V. Teixeira, C. Oliveira, Surface and Coatings Technology, 200 (2006) 6783-6791.
[78] M. Habibi, L. Wang, S. Guo, Journal of the European Ceramic Society, 32 (2012) 1635-1642.
[79] W. Braue, P. Mechnich, Journal of the American Ceramic Society, 94 (2011) 4483-4489.
[80] C.G. Levi, J.W. Hutchinson, M.-H. Vidal-Sétif, C.A. Johnson, MRS bulletin, 37 (2012) 932-941.
[81] A.K. Rai, R.S. Bhattacharya, D.E. Wolfe, T.J. Eden, International Journal of Applied Ceramic Technology, 7 (2010) 662-674.
[82] S. Krämer, J. Yang, C.G. Levi, C.A. Johnson, Journal of the American Ceramic Society, 89 (2006) 3167-3175.
[83] C. Mercer, S. Faulhaber, A. Evans, R. Darolia, Acta materialia, 53 (2005) 1029-1039.
[84] S. Krämer, J. Yang, C.G. Levi, Journal of the American Ceramic Society, 91 (2008) 576-583.

[85] M. Vidal-Setif, N. Chellah, C. Rio, C. Sanchez, O. Lavigne, Surface and Coatings Technology, 208 (2012) 39-45.
[86] P. Mechnich, W. Braue, Journal of the American Ceramic Society, 96 (2013) 1958-1965.
[87] A.R. Krause, H.F. Garces, G. Dwivedi, A.L. Ortiz, S. Sampath, N.P. Padture, Acta Materialia, 105 (2016) 355-366.
[88] S. Krämer, S. Faulhaber, M. Chambers, D.R. Clarke, C.G. Levi, J.W. Hutchinson, A.G. Evans, Materials Science and Engineering: A, 490 (2008) 26-35.
[89] M.P. Borom, C.A. Johnson, L.A. Peluso, Surface and Coatings Technology, 86 (1996) 116-126.
[90] A. Aygun, A.L. Vasiliev, N.P. Padture, X. Ma, Acta Materialia, 55 (2007) 6734-6745.
[91] A.R. Krause, H.F. Garces, B.S. Senturk, N.P. Padture, Journal of the American Ceramic Society, 97 (2014) 3950-3957.
[92] J.M. Drexler, K. Shinoda, A.L. Ortiz, D. Li, A.L. Vasiliev, A.D. Gledhill, S. Sampath, N.P. Padture, Acta Materialia, 58 (2010) 6835-6844.
[93] B.A. Vazquez, A. Caballero, P. Pena, Journal of the American Ceramic Society, 86 (2003) 2195-2199.
[94] C. Jiang, E.H. Jordan, A.B. Harris, M. Gell, J. Roth, Journal of Thermal Spray Technology, 24 (2015) 895-906.
[95] D.E. Mack, T. Wobst, M.O.D. Jarligo, D. Sebold, R. Vaßen, Surface and Coatings Technology, 324 (2017) 36-47.
[96] J. Feng, X. Ren, X. Wang, R. Zhou, W. Pan, Scripta Materialia, 66 (2012) 41-44.
[97] L. Guo, H. Guo, H. Peng, S. Gong, Journal of the European Ceramic Society, 34 (2014) 1255-1263.
[98] Y. Shen, R.M. Leckie, C.G. Levi, D.R. Clarke, Acta Materialia, 58 (2010) 4424-4431.
[99] S. Raghavan, H. Wang, R.B. Dinwiddie, W.D. Porter, R. Vaβen, D. Stöver, M.J. Mayo, Journal of the American Ceramic Society, 87 (2004) 431-437.
[100] R. Vaßen, M.O. Jarligo, T. Steinke, D.E. Mack, D. Stöver, Surface and Coatings Technology, 205 (2010) 938-942.
[101] X. Song, M. Xie, R. Mu, F. Zhou, G. Jia, S. An, Acta Materialia, 59 (2011) 3895-3902.
[102] D. Zhu, J.A. Nesbitt, C.A. Barrett, T.R. McCue, R.A. Miller, Journal of thermal spray technology, 13 (2004) 84-92.

[103] C.B. Carter, M.G. Norton, Ceramic materials: science and engineering, Springer Science & Business Media, 2007.
[104] M. Jarligo, D. Mack, G. Mauer, R. Vaßen, D. Stöver, Journal of thermal spray technology, 19 (2010) 303-310.
[105] R. Gadow, M. Lischka, Surface and Coatings Technology, 151-152 (2002) 392-399.
[106] X. Xie, H. Guo, S. Gong, Journal of thermal spray technology, 19 (2010) 1179-1185.
[107] H. Lehmann, D. Pitzer, G. Pracht, R. Vassen, D. Stöver, Journal of the American Ceramic Society, 86 (2003) 1338-1344.
[108] G. Mauer, D. Sebold, R. Vaßen, D. Stöver, Journal of thermal spray technology, 21 (2012) 363-371.
[109] C. Wan, Z. Qu, A. Du, W. Pan, Acta Materialia, 57 (2009) 4782-4789.
[110] J.M. Drexler, A.L. Ortiz, N.P. Padture, Acta Materialia, 60 (2012) 5437-5447.
[111] M.H. Habibi, L. Wang, S.M. Guo, Journal of the European Ceramic Society, 32 (2012) 1635-1642.
[112] C. Wang, L. Guo, Y. Zhang, X. Zhao, F. Ye, Ceramics International, 41 (2015) 10730-10735.
[113] E. Bakan, D.E. Mack, G. Mauer, R. Mücke, R. Vaßen, Journal of the American Ceramic Society, 98 (2015) 2647-2654.
[114] L. Guo, M. Li, C. Zhang, X. Huang, F. Ye, Materials Letters, 188 (2017) 142-144.
[115] M.P. Schmitt, J.L. Stokes, B.L. Gorin, A.K. Rai, D. Zhu, T.J. Eden, D.E. Wolfe, Surface and Coatings Technology, 313 (2017) 177-183.
[116] U. Kogelschatz, Plasma Physics and Controlled Fusion, 46 (2004) B63.
[117] J.V. Heberlein, P. Fauchais, M.I. Boulos, thermal spray fundamental, 2014.
[118] P. Fauchais, Journal of Physics D: Applied Physics, 37 (2004) R86.
[119] J. Coudert, M. Planche, P. Fauchais, Plasma chemistry and plasma processing, 16 (1995) S211-S227.
[120] H. Guo, R. Vaßen, D. Stöver, Surface and Coatings technology, 186 (2004) 353-363.
[121] K. Ito, H. Kuriki, M. Watanabe, S. Kuroda, M. Enoki, Materials Transactions, 53 (2012) 671-675.
[122] J. Singh, D. Wolfe, Journal of materials Science, 40 (2005) 1-26.
[123] A.F. Renteria, B. Saruhan, U. Schulz, H.J. Raetzer-Scheibe, J. Haug, A. Wiedenmann, Surface and Coatings Technology, 201 (2006) 2611-2620.

[124] K. Von Niessen, M. Gindrat, Journal of thermal spray technology, 20 (2011) 736-743.
[125] G. Mauer, A. Hospach, R. Vaßen, Surface and Coatings Technology, 220 (2013) 219-224.
[126] S. Rezanka, G. Mauer, R. Vaßen, Journal of Thermal Spray Technology, 23 (2014) 182-189.
[127] L. Pawlowski, Surface and Coatings Technology, 203 (2009) 2807-2829.
[128] N. Curry, Z. Tang, N. Markocsan, P. Nylén, Surface and Coatings Technology, 268 (2015) 15-23.
[129] C. Delbos, J. Fazilleau, V. Rat, J.-F. Coudert, P. Fauchais, B. Pateyron, Plasma Chemistry and Plasma Processing, 26 (2006) 393-414.
[130] A. Vardelle, C. Moreau, N.J. Themelis, C. Chazelas, Plasma Chemistry and Plasma Processing, 35 (2015) 491-509.
[131] H. Kassner, R. Siegert, D. Hathiramani, R. Vassen, D. Stoever, Journal of thermal spray technology, 17 (2008) 115-123.
[132] K. VanEvery, M.J. Krane, R.W. Trice, H. Wang, W. Porter, M. Besser, D. Sordelet, J. Ilavsky, J. Almer, Journal of thermal spray technology, 20 (2011) 817-828.
[133] B. Bernard, A. Quet, L. Bianchi, A. Joulia, A. Malié, V. Schick, B. Rémy, Surface and Coatings Technology, (2016).
[134] A. Ganvir, S. Joshi, N. Markocsan, R. Vassen, Materials & Design.
[135] Z. Zou, J. Donoghue, N. Curry, L. Yang, F. Guo, P. Nylén, X. Zhao, P. Xiao, Surface and Coatings Technology, 275 (2015) 276-282.
[136] P. Sokołowski, S. Kozerski, L. Pawłowski, A. Ambroziak, Surface and Coatings Technology, 260 (2014) 97-106.
[137] P. Sokołowski, L. Pawłowski, D. Dietrich, T. Lampke, D. Jech.
[138] A. Ganvir, N. Curry, N. Markocsan, P. Nylén, F.-L. Toma, Surface and Coatings Technology, 268 (2015) 70-76.
[139] S. Mahade, N. Curry, S. Björklund, N. Markocsan, P. Nylén, Surface and Coatings Technology, (2015).
[140] B. Bernard, A. Quet, L. Bianchi, V. Schick, A. Joulia, A. Malié, B. Rémy, Journal of Thermal Spray Technology, 26 (2017) 1025-1037.
[141] P. Fauchais, G. Montavon, R. Lima, B. Marple, Journal of Physics D: Applied Physics, 44 (2011) 093001.
[142] in, http://www.mettech.com/coating-equipment/axial-III-plasma-spray-system.php.

[143] S. Deshpande, A. Kulkarni, S. Sampath, H. Herman, Surface and coatings technology, 187 (2004) 6-16.
[144] X. Zhang, B. Xu, F. Xuan, H. Wang, Y. Wu, S. Tu, Journal of Alloys and Compounds, 467 (2009) 501-508.
[145] L. Whittig, W. Allardice, Methods of Soil Analysis: Part 1—Physical and Mineralogical Methods, (1986) 331-362.
[146] D. Dorset, Microscopy and Microanalysis, 4 (1998) 513-515.
[147] M. Fitzpatrick, A. Fry, P. Holdway, F. Kandil, J. Shackleton, L. Suominen, (2005).
[148] G. Witz, V. Shklover, W. Steurer, S. Bachegowda, H.P. Bossmann, Journal of the American Ceramic Society, 90 (2007) 2935-2940.
[149] J. Malzbender, J. Den Toonder, A. Balkenende, Materials Science and Engineering: R: Reports, 36 (2002) 47-103.
[150] F. Sergejev, M. Antonov, Proc. Estonian Acad. Sci. Eng, 12 (2006) 388-398.
[151] F. Traeger, R. Vaßen, K.H. Rauwald, D. Stöver, Advanced Engineering Materials, 5 (2003) 429-432.
[152] T. Steinke, D. Sebold, D.E. Mack, R. Vaßen, D. Stöver, Surface and Coatings Technology, 205 (2010) 2287-2295.
[153] U. Schulz, O. Bernardi, A. Ebach-Stahl, R. Vassen, D. Sebold, Surface and coatings technology, 203 (2008) 160-170.
[154] S. Rezanka, D.E. Mack, G. Mauer, D. Sebold, O. Guillon, R. Vaßen, Surface and Coatings Technology, 324 (2017) 222-235.
[155] B. Rajasekaran, G. Mauer, R. Vassen, Journal of Thermal Spray Technology, 20 (2011) 1209-1216.
[156] A. Ganvir, N. Curry, S. Björklund, N. Markocsan, P. Nylén, Journal of Thermal Spray Technology, 24 (2015) 1195-1204.
[157] Nicholas Curry 1, Kent VanEvery 2, Todd Snyder 2 and Nicolaie Markocsan 1, (2014).
[158] N. Schlegel, S. Ebert, G. Mauer, R. Vassen, Journal of thermal spray technology, 24 (2015) 144-151.
[159] F. Andreola, C. Leonelli, M. Romagnoli, P. Miselli, American Ceramic Society Bulletin, 79 (2000) 49-52.
[160] A. Moign, A. Vardelle, N. Themelis, J. Legoux, Surface and Coatings Technology, 205 (2010) 668-673.
[161] R. Vaßen, S. Giesen, D. Stöver, Journal of thermal spray technology, 18 (2009) 835-845.

[162] G. Beshish, C. Florey, F. Worzala, W. Lenling, Journal of Thermal Spray Technology, 2 (1993) 35-38.
[163] M. Guazzato, M. Albakry, S.P. Ringer, M.V. Swain, Dental materials, 20 (2004) 449-456.
[164] R. Vaßen, G. Kerkhoff, D. Stöver, Materials Science and Engineering: A, 303 (2001) 100-109.
[165] G.W. Schulze, F. Erdogan, International Journal of Solids and Structures, 35 (1998) 3615-3634.
[166] K.W. Schlichting, N. Padture, E. Jordan, M. Gell, Materials Science and Engineering: A, 342 (2003) 120-130.
[167] A. Ganvir, R.F. Calinas, N. Markocsan, N. Curry, S. Joshi, Journal of the European Ceramic Society, (2018).
[168] M. Ahrens, R. Vaßen, D. Stöver, Surface and Coatings Technology, 161 (2002) 26-35.
[169] S. Tsipas, I. Golosnoy, T. Clyne, R. Damani, Journal of thermal spray technology, 13 (2004) 370-376.
[170] D. Zhu, R.A. Miller, Journal of Thermal Spray Technology, 9 (2000) 175-180.
[171] D. Renusch, M. Schorr, M. Schütze, Materials and corrosion, 59 (2008) 547-555.
[172] C. Nordhorn, R. Mücke, D.E. Mack, R. Vassen, Mechanics of materials, 93 (2016) 199-208.
[173] A. Casu, J. Marqués, R. Vassen, D. Stöver, in: Key Engineering Materials, Trans Tech Publ, 2007, pp. 263-268.
[174] B. Siebert, C. Funke, R. Vaβen, D. Stöver, Journal of Materials Processing Technology, 92 (1999) 217-223.
[175] A. Bacciochini, F. Ben-Ettouil, E. Brousse, J. Ilavsky, G. Montavon, A. Denoirjean, S. Valette, P. Fauchais, Surface and Coatings Technology, 205 (2010) 683-689.
[176] V. Lughi, V.K. Tolpygo, D.R. Clarke, Materials Science and Engineering: A, 368 (2004) 212-221.
[177] Y. Zhao, L. Wang, J. Yang, D. Li, X. Zhong, H. Zhao, F. Shao, S. Tao, Journal of Thermal Spray Technology, 24 (2015) 338-347.
[178] R. Vaßen, D. Stöver, in: Thermal Spray 2007: Global Coating Solutions: Proceedings of the 2007 International Thermal Spray Conference, ASM International, 2007, pp. 417.

[179] L. Zhe, K. Min-Sik, S.-W. Myoung, L. Je-Hyun, J. Yeon-Gil, K. In-Soo, J. Chang-Yong, Transactions of Nonferrous Metals Society of China, 24 (2014) s29-s35.
[180] M. Karger, R. Vaßen, D. Stöver, Surface and Coatings Technology, 206 (2011) 16-23.
[181] X. Chen, T. Ohnuki, S. Kuroda, M. Gizynski, H. Araki, H. Murakami, M. Watanabe, Y. Sakka, Ceramics International, 42 (2016) 16822-16832.
[182] L. Łatka, A. Cattini, L. Pawłowski, S. Valette, B. Pateyron, J.-P. Lecompte, R. Kumar, A. Denoirjean, Surface and Coatings Technology, 208 (2012) 87-91.
[183] A. Ganvir, N. Markocsan, S. Joshi, Coatings, 7 (2016) 4.
[184] Q. Chen, W. Mao, Y. Zhou, C. Lu, Applied Surface Science, 256 (2010) 7311-7315.
[185] C. Weyant, J. Almer, K. Faber, Acta materialia, 58 (2010) 943-951.
[186] C. Johnson, J. Ruud, R. Bruce, D. Wortman, Surface and Coatings Technology, 108 (1998) 80-85.
[187] V. Viswanathan, G. Dwivedi, S. Sampath, Journal of the American Ceramic Society, 98 (2015) 1769-1777.
[188] N. Schlegel, D. Sebold, Y. Sohn, G. Mauer, R. Vassen, Journal of thermal spray technology, 24 (2015) 1205-1212.
[189] M.C. Hatnean, M. Lees, G. Balakrishnan, Journal of Crystal Growth, 418 (2015) 1-6.
[190] M.J.D. Rushton, C.R. Stanek, A.R. Cleave, B.P. Uberuaga, K.E. Sickafus, R.W. Grimes, Nuclear Instruments and Methods in Physics Research Section B: Beam Interactions with Materials and Atoms, 255 (2007) 151-157.

Appendix

Sample	Top coat protocol number	Plasma gas (slpm)	Input power (kW)	Current (A)	Spraying distance (mm)	Meander	Bond coat	Bond coat condition	Substrate	Suspension/ powder	Cycles
A	A-16-008-A3	Ar (183.4), H_2 (36.8), N_2 (24.5)	105.5	750	70	320*2*16	Amdry 9954 (FM-15-552-dj)	Mirror polished	Stainless steel	10 wt.% TZ-5Y	50
B	A-16-008-A3	Ar (183.4), H_2 (36.8), N_2 (24.5)	105.5	750	70	320*2*16	Amdry 9954 (FM-15-552-dj)	Grinding	Stainless steel	10 wt.% TZ-5Y	50
C	A-16-008-A3	Ar (183.4), H_2 (36.8), N_2 (24.5)	105.5	750	70	320*2*16	Amdry 9954 (FM-15-552-dj)	Grit blasting	Stainless steel	10 wt.% TZ-5Y	50
D	A-16-008-A3	Ar (183.4), H_2 (36.8), N_2 (24.5)	105.5	750	70	320*2*16	Amdry 9954 (FM-15-552-dj)	As-sprayed	Stainless steel	10 wt.% TZ-5Y	50
E	A-16-017-A3	Ar (183.4), H_2 (36.8), N_2 (24.5)	105.5	750	100	320*2*16	Amdry 9954 (FM-15-552-dj)	Mirror polishing	Stainless steel	10 wt.% TZ-5Y	100
F	A-16-017-A3	Ar (183.4), H_2 (36.8), N_2 (24.5)	105.5	750	100	320*2*16	Amdry 9954 (FM-15-552-dj)	grinding	Stainless steel	10 wt.% TZ-5Y	100
G	A-16-017-A3	Ar (183.4), H_2 (36.8),	105.5	750	100	320*2*16	Amdry 9954 (FM-15-552-dj)	Grit blasting	Stainless steel	10 wt.% TZ-5Y	100

		N_2 (24.5)									
H	A-16-017-A3	Ar (183.4), H_2 (36.8), N_2 (24.5)	105.5	750	100	320*2*16	Amdry 9954 (FM-15-552-dj)	As-sprayed	Stainless steel	10 wt.% TZ-5Y	100
I	A-16-017-A3	Ar (183.4), H_2 (36.8), N_2 (24.5)	105.5	750	100	320*2*16	Amdry 9954 (FM-16-195-dj)	As-sprayed (coarse)	Stainless steel	10 wt.% TZ-5Y	100
J	A-16-012-A3	Ar (183.4), H_2 (36.8), N_2 (24.5)	84	600	70	320*2*16	Amdry 9954 (FM-16-194-dj)	As-sprayed	Stainless steel	10 wt.% TZ-5Y	50
K	A-17-014-A3	Ar (183.4), H_2 (36.8), N_2 (24.5)	105.5	750	70	320*2*16	Amdry 9954 (M-17-035-dj)	As-sprayed	Stainless steel	5 wt.% TZ-5Y	80
L	A-17-015-A3	Ar (183.4), H_2 (36.8), N_2 (24.5)	105.5	750	100	320*2*16	Amdry 9954 (M-17-035-dj)	As-sprayed	Stainless steel	5 wt.% TZ-5Y	150
M	A-16-024-A3	Ar (183.4), H_2 (36.8), N_2 (24.5)	105.5	750	70	320*2*16	Amdry 9954 (V-15-10-F4)	As-sprayed	IN 738	5 wt.% TZ-5Y	150
N	A-16-026-A3	Ar (183.4), H_2 (36.8), N_2 (24.5)	105.5	750	100	320*2*16	Amdry 9954 (V-15-10-F4)	As-sprayed	IN 738	5 wt.% TZ-5Y	280
O	A-17-001-A3	Ar (183.4), H_2 (36.8), N_2 (24.5)	105.5	750	70	320*2*16	Amdry 9954 (V-15-10-F4)	As-sprayed	IN 738	5 wt.% TZ-4Y	200

P	A-17-013-A3	Ar (183.4), H_2 (36.8), N_2 (24.5)	105.5	750	70	200*2*16	Amdry 9954 (v-16-035-f4)	As-sprayed	IN 738	5 wt.% TZ-4Y	250
Q	A-18-003-A3	Ar (183.4), H_2 (36.8), N_2 (24.5)	105.5	750	70	320*2*16	Amdry 9954 (v-16-038-f4)	As-sprayed	IN 738	5 wt.% TZ-4Y	190
R	A-18-005-A3	Ar (183.4), H_2 (36.8), N_2 (24.5)	105.5	750	100	320*2*16	Amdry 9954 (V-18-019-f4)	Grinding followed by pre-oxidation	IN 738	5 wt.% TZ-4Y	490
S-0 h S-1 h S-3 h S-10 h S-50 h	A-16-029-A3, A-17-007-A3, A-17-008-A3	Ar (183.4), H_2 (36.8), N_2 (24.5)	105.5	750	70	320*2*16	Amdry 9954 (V-15-20-F4)	As-sprayed	IN 738	10 wt.% NAMI	138
T	A-17-033-A3	Ar (183.4), H_2 (36.8), N_2 (24.5)	105.5	750	100	320*2*16	Amdry 9954 (v-16-035-f4)	As-sprayed	IN 738	5 wt.% GZO	336
U	A-18-001-A3/ A-18-002-A3	Ar (183.4), H_2 (36.8), N_2 (24.5)	105.5	750	100/ 70	320*2*16	Amdry 9954 (V-16-038-f4)	As-sprayed	IN 738	5 wt.% GZO	100/200
V	M-18-030-tp	Ar (46.5), He(4)	37.7	420	200	250*2*18	Amdry 9954 (V-16-038-f4)	As-sprayed	IN 738	YSZ (YSZ 412M)	20

Acknowledgments

This is the hardest part for me. Three years of memory flood into my mind. I would like to thank all who in one way or another contributed in the completion of this thesis.

Foremost, I would like to express my deeply thanks to my supervisor Prof. Robert Vaßen for giving me such precious opportunity to complete my PhD work in Forschungszentrum Jülich. His patience, enthusiasm as well as his broad knowledge and experience made working with him a very enjoyable fruitful and invaluable experience for me. I would also like to acknowledge the financial support from Helmholtz Association of German Research Centers and China Scholarship Council (CSC).

I would also like to thank our institute colleagues who supported my work enthusiastically and created a friendly working environment. I would like to Dr. Georg Mauer, Dr. Daniel Mack and Dr. Emine Bakan and Prof. Olivier Guillon for their fruitful and constructive discussions. My faithful appreciations also go to Dr. Schlegel Nadin for her patient and invaluable helps at my first 6 months here. She taught me a lot of useful experiment tips and basic knowledge on SPS. I would also like to thank Mr. Karl-Heinz Rauwald, Mr. Frank Kurze for their professional help on operating spraying facilities. If I have problems on spraying facilities, I always can find solutions from them. Many thanks to Dr. Yoo-Jung Sohn for her patient help on XRD analysis; Mr. Mark Kappertz for his introduction on metallography; Mr. Volker Bader for his help on heat treatment; Ms. Sigrid Schwartz-Lückge for porosity measurements; Mr. Martin Tandler for thermal cycling tests. Furthermore, I would like to thank colleagues from IEK-2, Dr. Jürgen Malzbender and Mr. Gang Yan for their supports on indentation tests. I am sorry not able to list everyone who helped me and contributed to this thesis. I am grateful for your helps. Thank you all.

Last but not least, I would like to thank my beloved family, for their support, love and encouragement throughout my study in Germany. Special thanks to my wife for her accompany and support during my hardest time.

Band / Volume 442
Future Grid Load of the Residential Building Sector
L. Kotzur (2018), xxi, 213 pp
ISBN: 978-3-95806-370-9

Band / Volume 443
Yttriumoxid-Dünnschichten als Tritium-Permeationsbarriere
J. Engels (2018), 252 pp
ISBN: 978-3-95806-371-6

Band / Volume 444
Inverse conditioning of a high resolution integrated terrestrial model at the hillslope scale: the role of input data quality and model structural errors
S. Gebler (2018), xxii, 160 pp
ISBN: 978-3-95806-372-3

Band / Volume 445
Cathode Stability and Processing in Inert Substrate-Supported Solid Oxide Fuel Cells
E. Matte (2018), viii, 178 pp
ISBN: 978-3-95806-373-0

Band / Volume 446
Aging and Degradation Behavior of Electrode Materials in Solid Oxide Fuel Cells (SOFCs)
X. Yin (2018), x, 103 pp
ISBN: 978-3-95806-374-7

Band / Volume 447
TRENDS 2017
Transition to Renewable Energy Devices and Systems
D. Stolten, R. Peters (Eds.) (2018), 206 pp
ISBN: 978-3-95806-376-1

Band / Volume 448
3D simulation of impurity transport in a fusion edge plasma using a massively parallel Monte-Carlo code
J. Romazanov (2018), xvi, 149 pp
ISBN: 978-3-95806-377-8

Band / Volume 449
Projektbericht Adelheid – aus dem Labor heraus in die Lüfte
R. Peters, J. Pasel, R. C. Samsun, A. Tschauder, C. Wiethege, F. Scharf, D. Stolten (2018), xxi, 321 pp
ISBN: 978-3-95806-378-5

Band / Volume 450
Microstructure and Thermomechanical Properties of $SrTi_{1-x}Fe_xO_{3-\delta}$ Oxygen Transport Membranes and Supports
R. Oliveira Silva (2019), vi, 148 pp
ISBN: 978-3-95806-381-5

Band / Volume 451
Sodium Ion Conducting Ceramics for Sodium Ion Batteries
S. Naqash (2019), vii, 134 pp
ISBN: 978-3-95806-382-2

Band / Volume 452
Quantitative Analyse der Trocknungsverläufe von Katalysatordispersionen
F. Scheepers (2019), VIII, 191 pp
ISBN: 978-3-95806-384-6

Band / Volume 453
Neue Optionen für einen wirtschaftlichen Betrieb von Wasserstoffzügen durch Nutzung der LOHC-Technologie?
P. Wasserscheid, T. Grube, D. Sternfeld, M. Essl, M. Robinius, D. Stolten (2019), II, 88 pp
ISBN: 978-3-95806-386-0

Band / Volume 454
Reformierung von BtL-Kraftstoffen für die HT-PEFC in luftfahrttechnischen Systemen
C. Wilbrand (2019), IV, 312 pp
ISBN: 978-3-95806-387-7

Band / Volume 455
Entwicklung von thermischen Spritzprozessen für fortschrittliche Schutz- und Funktionsschichten
G. Mauer (2019), vi, 57 pp
ISBN: 978-3-95806-388-4

Band / Volume 456
Columnar Structured Thermal Barrier Coatings Deposited by Axial Suspension Plasma Spraying
D. Zhou (2019), VI, 126 pp
ISBN: 978-3-95806-391-4

Energie & Umwelt / Energy & Environment
Band / Volume 456
ISBN 978-3-95806-391-4

Mitglied der Helmholtz-Gemeinschaft

JÜLICH
Forschungszentrum